

Flow and Thermal Analysis of Oldroyd-B Fluid due to Stretching Surfaces



By
Muhammad Yasir

**Department of Mathematics
Quaid-i-Azam University
Islamabad, Pakistan
2024**

Flow and Thermal Analysis of Oldroyd-B Fluid due to Stretching Surfaces



By
Muhammad Yasir

Supervised By
Prof. Dr. Masood Khan

**Department of Mathematics
Quaid-i-Azam University
Islamabad, Pakistan
2024**

Flow and Thermal Analysis of Oldroyd-B Fluid due to Stretching Surfaces



By
Muhammad Yasir

A DISSERTATION SUBMITTED IN THE PARTIAL FULFILLMENT OF THE
REQUIREMENT FOR THE DEGREE OF
DOCTOR OF PHILOSOPHY
IN
MATHEMATICS

Supervised By
Prof. Dr. Masood Khan

Department of Mathematics
Quaid-i-Azam University
Islamabad, Pakistan
2024

Author's Declaration

I, **Muhammad Yasir** hereby state that my Ph.D. thesis titled "**Flow and Thermal Analysis of Oldroyd-B Fluid due to Stretching Surfaces**" is my own work and has not been submitted previously by me for taking any degree from the Quaid-i-Azam University, Islamabad, Pakistan or anywhere else in the country/world.

At any time if my statement is found to be incorrect even after my graduate the university has the right to withdraw my Ph.D. degree.



Name of Student: **Muhammad Yasir**

Date: **February 16, 2024**

Plagiarism Undertaking

I solemnly declare that research work presented in the thesis titled "**Flow and Thermal Analysis of Oldroyd-B Fluid due to Stretching Surfaces**" is solely my research work with no significant contribution from any other person. Small contribution/help wherever taken has been duly acknowledged and that complete thesis has been written by me.

I understand the zero tolerance policy of the HEC and Quaid-i-Azam University, Islamabad towards plagiarism. Therefore, I as an Author of the above titled thesis declare that no portion of my thesis has been plagiarized and any material used as reference is properly referred/cited.

I undertake that if I am found guilty of any formal plagiarism in the above titled thesis even afterward of PhD degree, the University reserves the rights to withdraw/revoke my PhD degree and that HEC and the University has the right to publish my name on the HEC/University Website on which names of students are placed who submitted plagiarized thesis.

Student/Author Signature: _____



Name: **Muhammad Yasir**

Certificate of Approval

This is to certify that the research work presented in this thesis entitled **Flow and Thermal Analysis of Oldroyd-B Fluid due to Stretching Surfaces** was conducted by Mr. **Muhammad Yasir** under the kind supervision of **Prof. Dr. Masood Khan**. No part of this thesis has been submitted anywhere else for any other degree. This thesis is submitted to the Department of Mathematics, Quaid-i-Azam University, Islamabad in partial fulfilment of the requirements for the degree of Doctor of Philosophy in field of Mathematics from Department of Mathematics, Quaid-i-Azam University, Islamabad, Pakistan.

Student Name: Muhammad Yasir

Signature: 


External Committee:

a) External Examiner 1:

Name: Dr. Zaheer Abbas

Designation: Professor

Office Address: Department of Mathematics, The Islamia University of Bahawalpur, Bahawalpur.


Signature: 

b) External Examiner 2:

Name: Dr. Muhammad Qasim

Designation: Associate Professor

Office Address: Department of Mathematics, COMSATS University, Islamabad.

Signature: 

c) Internal Examiner:

Name: Dr. Masood Khan

Designation: Professor

Office Address: Department of Mathematics, Quaid-i-Azam University, Islamabad

Signature: 


Supervisor Name:

Prof. Dr. Masood Khan

Signature: 

Name of Dean/HOD:

Prof. Dr. Tariq Shah

Signature: 

Flow and Thermal Analysis of Oldroyd-B Fluid due to Stretching Surfaces

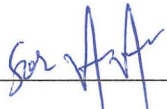
By

Muhammad Yasir

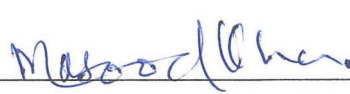
CERTIFICATE

A DISSERTATION SUBMITTED IN THE PARTIAL FULFILLMENT OF THE
REQUIREMENTS FOR THE DEGREE OF THE
DOCTOR OF PHILOSOPHY IN MATHEMATICS

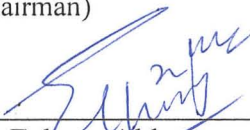
We accept this dissertation as conforming to the required standard

1. 

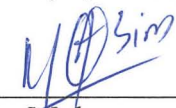
Prof. Dr. Tariq Shah
(Chairman)

2. 

Prof. Dr. Masood Khan
(Supervisor)

3. 

Prof. Dr. Zaheer Abbas
(External Examiner)
Department of Mathematics,
The Islamia University of Bahawalpur,
Bahawalpur

4. 

Dr. Muhammad Qasim
(External Examiner)
Department of Mathematics,
COMSATS University,
Islamabad

**Department of Mathematics
Quaid-i-Azam University
Islamabad, Pakistan
2024**

Dedication

I am feeling great honour and pleasure to dedicate my Ph.D. thesis to

My Father (Late)

Haji Ghulam Jan

Acknowledgement

In the name of **ALLAH**, the Most Glorious and the Most Merciful Lord, the creator and all praises to **ALLAH** who guide me in darkness, helps me in troubles and empowers me to view tentative blocks as stepping stones to the stars to reach the eventual stage with courage. I am nothing without my **ALLAH** but I can achieve everything with assistance. All my reverence and commitment goes to our **Prophet Hazrat Muhammad SAWW** the source of humanity, kindness, and guidance for the whole creatures and who advised the mankind to pursue knowledge from cradle to grave.

First and foremost, I would like to express my special appreciation and thanks to my Ph.D. advisor **Prof. Dr. Masood Khan**, you have been a tremendous mentor for me. I would like to thank you for encouraging my research and for allowing me to grow as a research scientist. Your advice on both research as well as on my career have been invaluable. In short, your tireless work, unique way of research and devotion to your profession cannot be expressed in words.

I am very grateful to the honorable **Distinguished National Prof. Dr. Tasawar Hayat** for his Excellency throughout my research and other educational circumstances.

I would like to thank my beloved mother and late father, whose love, prayers, and guidance are with me to follow my dreams. I am very thankful to my loving parents for their guidance, support, and encouragement. I owe my heartiest gratitude for their assistance and never ending prayers for success. I highly commend the cooperative behavior of my brothers, especially Dr. Muhammad Javid who endeavored for my edification and betterment. Most importantly, I wish to thank Mr. Saqib Javid, Mr. Junaid Sajjad, Mrs. Hifsa, Tayyaba, Izza, and Mahnoor (Niece) for sacrificing and helping in whatever way they could during this challenging period.

I gratefully acknowledge the Department of Mathematics, Quaid-i-Azam university Islamabad for this wonderful facilitation sources that made my Ph.D. work possible. My sincere thanks also goes to the chairman Department of Mathematics Prof. Dr. Tariq Shah, who provide me the opportunity for this milestone achievement.

I thank my friends and fellow lab mates for the stimulating discussions, for the sleepless nights we were working together, and for all the fun we have had in the last four years. A very special thanks to all of you, Dr. Latif Ahmad, Dr. Jawad Ahmed, Ms. Mahnoor Sarfraz, Dr. Awais Ahmed, Dr. Aamir Hamid, Dr. Abdul Hafeez, and Dr. Zahoor Iqbal for his invaluable advice and feedback

on my research and for always being so supportive of my work. My times at Quaid-i-Azam University were also enriched by the graduates and fellows of Dr. Sohail Ahmed Khan, Dr. Muhammad Naveed Khan, Mr. Muhammad Waqar Ahmed, Mr. Muhammad Bilal, Ms. Aneeta Razaq, Mr. Naveed Mir, Mr. Faqeer Shah, Mr. Muhammad, Mr. Umar Farooq, and Mr. Mudassar Qamar.

In the end I would like to thank all my research fellows and to those people who directly and indirectly helped me during my research work.

Best Regards

Muhammad Yasir

Abstract

The dynamics and rheology of complex fluid models have greatly motivated investigation in fluid mechanics. This is due to the increasing importance of complicated fluids in industrial applications. Although many substances in nature can flow but the traditional linearly viscous fluid models are unable to adequately predict their flow characteristics. They are referred to as non-Newtonian fluids. Two main phenomena, known as creep and relaxation are caused by viscous and elastic components in the viscoelasticity of rate-type non-Newtonian fluids. The majority of fluids found in nature are viscoelastic, including some biological fluids, paints, and polymers. In many engineering applications, including the manufacture of polymer sheets and plastic coatings, the flow of viscoelastic non-linear fluids with heat and mass transport is important. The heat transport rate has a considerable impact on the quality of these products. Therefore, the study of the rheological characteristics of viscoelastic fluids with thermal and solutal energy transportation is an immediate attraction of the present era of investigation.

Many investigations have been devoted to scrutinizing the Oldroyd-B fluid flow and energy transfer phenomenon induced by stretching surfaces. From this perspective, the current thesis is designed. Here, the primary focus is on the mathematical modeling of an Oldroyd-B material and analyzing its energy transport characteristics. The model under consideration predicts the features of both the relaxation and retardation times effects. Through appropriate similarity transformations, the governing partial differential equations for flow and energy transport are converted into ordinary differential equations. It is extremely difficult to compute exact solutions to the coupled system of modeled equations. Therefore, both semi-analytical and numerical approaches are used to compute the results. The diverse physical constraints that may have a significant impact on the flow and energy transport are taken into consideration. The results for the flow field and energy transport phenomenon are exhibited both graphically and in tabular form. The findings demonstrate that when the curvature parameter increases, the velocity, temperature, and concentration distributions near the cylinder's surface are enhanced. Moreover, for increasing values of Deborah numbers, the temperature and concentration distributions are higher in terms of relaxation time while these are declined in terms of retardation time. Additionally, the results demonstrate that the homogeneous response parameter exhibits

contradicting behavior on the concentration field while the thermal relaxation parameter lowers the temperature field.

Contents

1	Introduction	5
1.1	Background and literature survey	5
1.2	Fundamental laws and constitutive relations	12
1.3	Homogeneous and heterogeneous reactions	15
1.4	Oldroyd-B fluid model	16
1.5	Methods of computation	16
1.5.1	Analytic solution scheme	17
1.5.2	BVP Midrich scheme	19
1.6	Motivation and research objectives	20
1.7	Thesis overview	21
2	Modelling of Unsteady Oldroyd-B Fluid Flow due to Stretchable Cylindrical Surface	25
2.1	Development of governing equations	26
2.2	Model sketch	29
2.3	Statement of the problem	29

2.3.1	Similarity transformations	31
2.4	Engineering interest quantities	32
2.4.1	Nusselt number	32
2.4.2	Sherwood number	32
2.5	Analytical solution procedure	33
2.5.1	Zeroth order formulation	34
2.5.2	The $m - th$ order deformation	36
2.5.3	Convergence analysis	37
2.6	Validation of results	38
2.7	Results and discussion	39
2.8	Physical interpretation of engineering coefficient	46
3	Convective Transport of Thermal and Solutal Energy in Unsteady MHD	
	Oldroyd-B Nanofluid Flow	48
3.1	Mathematical formulation	49
3.2	Physical quantities	52
3.3	Maple solutions	52
3.4	Presentation of results	53
3.4.1	Analysis authentication	61
4	Radiative Flow of Oldroyd-B Nanofluid subject to Arrhenius Activation En-	
	ergy	62
4.1	Mathematical analysis	63
4.2	Quantities of interest	66

4.3	Solution methodology	66
4.4	Analysis of outcomes	67
4.5	Numerical data of physical quantities	74
5	Thermophoretic Particle Deposition with Soret-Dufour in a Flow of Fluid exhibit Relaxation/Retardation Times Effect	77
5.1	Physical problem description	78
5.2	Thermophoretic particle deposition	79
5.3	The problem solution	80
5.3.1	Solution technique	81
5.3.2	Convergence of solution	81
5.4	Physical parameters	82
5.5	Justification of graphical illustration	83
6	Dynamics of Heat Transport in Flow of Non-linear Oldroyd-B Fluid subject to non-Fourier's Theory	93
6.1	Problem formulation	94
6.2	Solutions expressions	97
6.3	Convergence analysis	98
6.4	Discussion of results	99
7	Axisymmetric of Oldroyd-B Material with Homogeneous-Heterogeneous Re- actions subject to Cattaneo-Christov Heat Transfer	105
7.1	Mathematical formulation	106

7.2	Homotopic solution	109
7.2.1	Convergence region	109
7.3	Analysis and discussion of results	110
7.3.1	Analysis of results	110
7.3.2	Discussion of results	111
8	Flow of Oldroyd-B Nanofluid in Non-Inertial Frame Inspired by Cattaneo-Christov Theory	122
8.1	Physical model and mathematical formulation	123
8.2	Solution procedure	126
8.3	Convergence analysis	127
8.4	Interpretation of graphical results	129
8.5	Results Authentication	136
9	Concluding Remarks and Future Directions	137
9.1	Summary of results	138
9.2	Future recommendations	139

Chapter 1

Introduction

The goal of the current theoretical investigation is outlined in this chapter along with a detailed review of the literature. Additionally, some information and basic mathematical relations that are useful in this study are provided. Moreover, the solution methods for the governing equations are outlined. At the end, a brief description of thesis outline is highlighted.

1.1 Background and literature survey

Non-Newtonian fluids usually exhibit nonlinear deformation when a shear force is applied. In industry, these fluids are plentiful in which adhesives, slurries, lubricating oils, mining tailing, and suspensions, as well as biological fluids, polymer melts, and pharmaceutical items, are all examples. Moreover, non-Newtonian fluids are used in a variety of applications, including petroleum drilling, biological fluid transport, crystal growth, and polymer extrusion. The features of non-Newtonian fluids are not sufficiently accounted for in the conventional Navier-Stokes equations. For non-Newtonian fluids, a variety of constitutive equations have been proposed.

It is not possible to describe the characteristics of all non-Newtonian fluids into one constitutive relationship. Generally, there can be classified into: (i) differential type (ii) integral type, and (iii) rate types. A Maxwell fluid model is a particularly basic rate-type fluid; it can only identify the characteristics of relaxation time and cannot display those of retardation time. The Oldroyd-B fluid model [1] is a modification of the Maxwell fluid model that effectively explains the dynamics of both the relaxation and the retardation phenomena. Oldroyd [1] was one of the first to create a strong constitutive relationship for a fluid, that is referred to as the Oldroyd-B fluid model, and characterizes the manners of nonlinear flows of various types. Several investigators have explored the flow and heat transport for an Oldroyd-B fluid under various geometries. Oldroyd-B fluid flow generated by stretching sheet is visualized by Bhatnagar *et al.* [2]. The decaying of a possible whirl in an Oldroyd-B liquid flow is investigated by Fetecau and Fetecau [3]. Further, the flow of an Oldroyd-B liquid towards a stretching surface is described by Hayat *et al.* [4]. The outcomes of Brownian and thermophoresis motion on the unsteady flow of Oldroyd-B fluid over a stretched surface were explored by Awad *et al.* [5]. Additionally, Hafeez *et al.* [6] studied the non-Newtonian Oldroyd-B liquid flow with heat transportation and solved the problem numerically. Very recently, the study of Oldroyd-B fluid by a rotating geometry was discussed by Khan *et al.* [7].

In fluid dynamics, most of the recent investigations on non-Newtonian fluids flows caused by a stretching sheet/surface have been made in the steady flows. The unsteady boundary layer has a major role in engineering sectors, such as regular fluid movement and start-up procedures. Due to unsteadiness, the boundary layer split and the pattern of fluid motion behave differently. Moore [8] was the first who investigated the boundary layer flow over an insulated flat surface moving with a time-dependent velocity. This analysis was extended by Chao and Jeng [9].

Yang [10] examined the time-dependent boundary layer flow around a stagnation region. Wang [11] explored the concept of the flow of liquid film over a time-dependent stretching surface. Khalili *et al.* [12] numerically examined the time-dependent nanofluid flow with a convective transport. Raju and Sandeep [13] explored the consequence of solar radiation with catalysts reaction in the unsteady flow of Carreau and Casson fluids across a stretched surface. Khan and Azam [14] investigated the mechanisms of unsteady thermal and solutal transportation in magneto-Carreau nanofluid flow via a hollow stretched surface. Li *et al.* [15] scrutinized the simultaneous properties of Wu's slip in the unsteady bioconvective flow of a Maxwell nanofluid. Additionally, the related publications can be encountered in Refs. [16 – 18].

Due to its significance, the energy transport phenomenon due to stretching surface enclosed studied comprehensively in recent years as a result of their broad scope of applications in many methodologies such as thermal exchangers, the fiber industry, crystal growing, hot rolling, etc. In the literature dealing with polymer processes, there have been several experimental and theoretical studies done on convective transport phenomenon over cylindrical bodies. The flow over a cylinder is usually considered to be two-dimensional because the cylinder radius is larger than the thickness of the boundary layer. On the contrary, when the cylinder having radius and boundary layer thickness are same then the flow is considered to be axisymmetric. In an axisymmetric flow over stretchable cylinder, the governing equations depend upon the term "transverse curvature" which induces the behavior of flow. In several applications, the effect of transverse curvature plays a vital role. For example, in wire and fiber drawing where precise prediction is needed and a thick boundary layer may exist on slender/near-slender surface. Numerical solutions of a boundary layer flow on a stretched surface were studied by Sakiadis [19]. Further, Crane [20] expanded this idea for the linear and exponentially stretching surface.

Patil *et al.* [21] explored the time-dependent mixed convective flow due to a vertical stretching cylinder under the outcomes of thermal and solutal distribution in the existence of chemical reactions. Butt *et al.* [22] examined the influences of magnetic fields on the production of entropy in viscous flow over a stretching cylinder. Rajesh *et al.* [23] scrutinized the effectiveness of chemical reactions on the free convection unsteady flow of a viscous fluid over an infinite stretching cylinder. Hayat *et al.* [24] investigated the double stratification effects in a mixed convective flow of Jeffrey fluid. Azam *et al.* [25] studied the thermal properties in flow of Cross nanoliquid with heat source/sink due to stretchable cylinder.

The term "nanofluid" refers to nanomaterials suspended in conventional liquids to enhance the process of coupled heat and mass transportation. In recent years, researchers have become more aware of the importance of nanoparticles in domains such as biology and health, electronics, biomaterials, food processing, and mechanical sciences. Furthermore, unique cancer therapy hypotheses, selective drug delivery, nanotechnologies, fermentation processes, and medicine all have an impact on the mobility of the relevant nanomaterials in the described structures. It is a well-known fact that fluids passing through microfluidic devices in refrigerators and thermal systems are entirely dependent on heat transport particles transported by nanomaterials. Nanofluid dynamics is thus the key term to grasp in any field that deals with non-particle suspensions in any form in order to achieve the best possible results. Nanofluid is a type of liquid that contains nanoparticles (1–100nm). Choi [26] first proposed the idea of these nanoparticles with enhanced thermophysical characteristics, which was later generalized by several scientists. Buongiorno [27] discussed the seven sliding processes in nanoparticle motion, which include thermophoresis and Brownian movement impacts. Alsabery *et al.* [28] studied the transient flow of alumina/water-based nanofluid in a porous media. Kho *et al.* [29] used

numerical simulations to investigate the thermal and velocity slips of Williamson nanofluid flow over a stretching sheet. Analysis of the radiative Maxwell material rendered by a rotating frame was discussed by Alzahrani and Khan [30]. Chu *et al.* [31] studied the rotating flow of Maxwell nano liquid by incorporating the gyrotactic microorganisms with irregular heat source-sink and Newtonian heating. Rasool and Wakif [32] investigated the influence of second-grade nanofluid over a convective surface towards a vertical Riga plate. Further attempts were made in this direction by several authors [33 – 35].

The natural phenomenon of thermal and solutal transport has numerous applications. In the food and chemical industries, heat exchanger efficiency is typically low when dealing with non-Newtonian fluids. Since the apparent viscosities of these fluids are high, laminar flow at high Prandtl numbers typically occurs. Additionally, the fouling issue in these thermal exchangers significantly affects cleaning downtime as well as heat transfer efficiency. Llorens *et al.* [36] conducted an experimental analysis of the thermal transfer approach to a non-Newtonian pseudoplastic fluid. The mixed convection thermal transport of a viscoelastic liquid under the Lorentz forces impact was explored by Mahabaleshwar *et al.* [37]. In the presence of a first-order chemical reaction, heat transport with a dual sampling of stratification in a non-Newtonian fluid flow towards inclined stretched surfaces was inspected by Rehman *et al.* [38]. Akhtar *et al.* [39] investigated the outcome of thermal and solutal transport on the Peristaltic flow of Casson fluid. In heated fluids, high-temperature gradients are also typical, which lowers the process quality and occasionally the fluid quality. Many studies have been conducted on the flow pattern characteristics with heat exchangers, see Refs. [40 – 44].

Due to the complexity of all the reactions in a system, it is additionally suitable and simplistic to restrict to binary kind only. The chemical reaction requires activation significance,

which must be unrestricted to start. The least amount of energy required to operate molecules or atoms in a chemical system so that they can initiate a chemical reaction is referred to as activation energy. The reaction activation energy can be calculated employing the Arrhenius equation, which explains how the rate constant varies with temperature. A chemical change occurs during chemical reaction, and one or more products are produced that differ in some way from the reactants. Many industrial applications require some kind of chemical reaction as a crucial stage in the manufacturing process. These kinds of reactions are typically conducted in chemical reactors, and they are frequently constrained by the degree of mass transfer attained. Instead of using an experimental approach, theoretical investigations into the impacts of activation energy on flow analysis are required. However, due to the complexity of the connection between a chemical reaction and solutal transportation, theoretical explorations are done in the existing study. The physical features of activation energy in chemical reactions are briefly described in a few articles. The effects of chemical reactions on binary reaction models with Arrhenius activation energy have been examined by Bestman [45]. Bestman [46] also investigated the influence of activation significance in the flow of a combustible combination across a vertical pipe with a radiation effect. Following that, the researchers continued their investigation on Arrhenius activation energy consequences under many intriguing circumstances with different flow configurations, as listed in Refs. [47 – 53].

The interaction of chemicals that produces chemical combinations is referred to as a chemical reaction. Some of these reactions necessitate the use of heat as well as a catalyst. A homogeneous catalytic response materializes when the catalyst and reactants exist in the identical phase, whereas a heterogeneous catalytic reaction happens when the catalyst and reactants exist not in the same phase. Homogeneous catalytic reactions are those that occur between gases

and liquids with oxygen as the catalyst, whereas heterogeneous catalytic reactions are those that occur between gas and liquid, liquid and solid, or solid and gas. Firstly, chemical reactions with the same diffusivities were presented by Chaudhary and Merkin [54]. In the following, Merkin [55] examined the laminar flow of a viscous liquid through a flat surface with chemical reactions. For cubic autocatalysis, he reported both homogeneous and the heterogeneous processes on the catalyst surface. This concept was later discussed by many researchers for instance, Animasaun *et al.* [56] investigated the unequal diffusivity case of catalyst reactions in a radiative viscoelastic fluid flow under the influence of Lorentz strength. Koriko *et al.* [57] scrutinized the influences of quartic autocatalytic chemical reactions on the flow of radiative Eyring-Powell alumina-water nanofluid. Kumar *et al.* [58] explored cubic auto-catalysis reactions in three-dimensional nanofluid flow with viscous and joule dissipations under thermal jump. The physical characteristics of the chemically reactive flow of second-grade nanomaterial were studied by Alsaadi *et al.* [59]. The consequence of Cattaneo-Christov heat flux and autocatalytic chemical processes on the dynamics of a micropolar fluid were examined by Sarojamma *et al.* [60]. Meenakumari *et al.* [61] analyzed the significance of Lorentz forces on Prandtl fluid flow subject to cubic autocatalysis type of chemical reaction.

The dynamics of heat transfer mechanism have become one of the most popular topics in recent years, because of their numerous applications in various engineering and technical processes, for instance, energy generators, nuclear reactors, electronic device cooling, biological and medical appliances, heat pumps, etc. The traditional Fourier's heat conduction law [62] has been shown to be the considerable effective example for predicting heat transfer mechanisms in a variety of systems. A thermal gradient is a material parameter that indicates the acceleration and direction of the temperature differences that occur most quickly around a

specific region. When there is no macroscopic comparative movement between the two sides exchanging heat, the heat flux is examined according to an experimental law. Such mechanisms include the conduction of heat through solids and the convective heat transfer between the fluid and the wall. In real-world engineering applications, it is typical for the comparable motion to coincide with thermal transport in a moving fluid. Heat transport in a body proceeds through a deformation motion even in solids. The possibility of such a relative motion affecting the heat flux or transfer density is investigated. As a result, it became crucial to extend the Fourier law to the point where thermal expansion and macroscopic proximate movement between the two sides of swapping heat occur. Cattaneo [63] proposed a successful modification by introducing a key characteristic of thermal relaxation time into Fourier's model. In order to keep the material-invariant formulation, Christov [64] used convected derivative to present frame-indifferent mathematical modeling and generalization of Cattaneo's model. This model is comprehended as the Cattaneo-Christov heat flux model in the literature. Alamri *et al.* [65] scrutinized the influences of solutal transport rate over a stretching cylinder subject to Cattaneo-Christov heat flux. Rasool and Zhang [66] investigated the characteristics of nanofluidic flow manifested by the Cattaneo-Christov heat transport due to a nonlinearly stretching sheet. This idea was expanded by many researchers and mathematicians to incorporate various flow features, (see Refs. [67 – 69]).

1.2 Fundamental laws and constitutive relations

The conservation laws, which are based on classical mechanics, are the fundamental axioms of fluid dynamics. These laws can be stated in integral and or differential form, and are utilized

to solve the fluid dynamics problems and are stated below.

Mass conservation:

$$\frac{\partial \rho}{\partial t} + \nabla \cdot (\rho \mathbf{V}) = 0, \quad (1.1)$$

Momentum conservation:

$$\rho \frac{d\mathbf{V}}{dt} = \nabla \cdot \hat{\tau} + \rho \hat{\mathbf{b}}, \quad (1.2)$$

where $\hat{\tau}$ the Cauchy stress tensor is

$$\hat{\tau} = -p\mathbf{I} + \mathbf{S}, \quad (1.3)$$

for magnetohydrodynamic case, Eq. (1.2) is modified as

$$\rho \frac{d\mathbf{V}}{dt} = -\nabla p + \nabla \cdot \mathbf{S} + \mathbf{J} \times \mathbf{B}, \quad (1.4)$$

the current density \mathbf{J} is defined as

$$\mathbf{J} = \sigma (\mathbf{V} \times \mathbf{B}). \quad (1.5)$$

Energy conservation:

$$\rho c_p \frac{dT}{dt} = -\nabla \cdot \hat{\mathbf{q}}, \quad (1.6)$$

the thermal flux $\hat{\mathbf{q}}$ is described by Fourier's law as

$$\hat{\mathbf{q}} = -k_1 \nabla T, \quad (1.7)$$

Concentration conservation:

$$\frac{dC}{dt} = -\nabla \cdot \hat{\mathbf{J}}, \quad (1.8)$$

the solutal flux $\hat{\mathbf{J}}$ is described by Fick's law as

$$\hat{\mathbf{J}} = -D_B \nabla C, \quad (1.9)$$

Energy and concentration conservation for nanofluids

The contribution of thermophoresis and the Brownian diffusion phenomena, in accordance with Buongiorno [27], improves the convective energy transport in nanofluids. Thus, by combining these two forces, the energy equations (1.6) and (1.8) are as:

$$\frac{dT}{dt} + \frac{\mathbf{1}}{\rho c_p} \nabla \cdot \hat{\mathbf{q}} = \tau \left[D_B \nabla C \cdot \nabla T + D_T \frac{\nabla T \cdot \nabla T}{T_\infty} \right], \quad (1.10)$$

$$\frac{\partial C}{\partial t} + \nabla \cdot \hat{\mathbf{J}} = \frac{D_T}{T_\infty} (\nabla \cdot \nabla T). \quad (1.11)$$

In the above equations, ρ , \mathbf{V} , ∇ , $\frac{d}{dt}$, $\hat{\tau}$, $\hat{\mathbf{b}}$, c_p , $\hat{\mathbf{q}}$, $\hat{\mathbf{J}}$, T , C , p , \mathbf{I} , \mathbf{S} , D_B , k_1 , σ , \mathbf{B} , D_T , τ , T_∞ are the fluid density, velocity field, vector differential operator, material derivative, body force, temperature, concentration, fluid pressure, identity tensor, extra stress tensor, Brownian diffusion coefficient, thermal conductivity, electrical conductivity, applied magnetic field, thermophoresis coefficient, the ratio between nanoparticle heat capacity of base fluid, and ambient temperature, respectively.

Cattaneo-Christov theory

As previously stated, Fourier's approach for heat conduction is unrealistic and contradicts the principle of causality. Therefore, Cattaneo-Christov [63, 64] introduced the relaxation time with upper convective derivative as follows to modify the mathematical relations given in Eqs. (1.7) and (1.9) as follows:

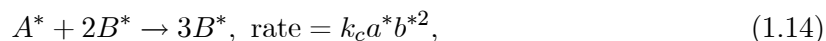
$$\hat{\mathbf{q}} + \lambda_t \frac{D\hat{\mathbf{q}}}{Dt} = -k_1 \nabla T, \quad (1.12)$$

$$\hat{\mathbf{J}} + \lambda_c \frac{D\hat{\mathbf{J}}}{Dt} = -D_B \nabla C, \quad (1.13)$$

in which λ_t and λ_c represent the thermal and solutal relaxation times.

1.3 Homogeneous and heterogeneous reactions

Based on Chaudhary and Merkin [54], an isothermal catalyst particle should exhibit the following fundamental homogeneous-heterogeneous response when utilized in cubic autocatalytic processes



the temperature of the entire system stays stable during this type of reaction. On the reactant surface, the isothermal reaction is represented by where A^* and B^* represent the autocatalysts of chemical reactions, a^* and b^* indicate the chemical reaction concentrations, further k_c , k_s represent the constants involved in the reaction.

1.4 Oldroyd-B fluid model

Generally, non-Newtonian fluids can be classified into (i) differential (ii) integral, and (iii) rate types. The simplest rate type non-Newtonian fluid is a Maxwell fluid model wherein only the properties of relaxation time are defined by this model while the retardation time characteristics cannot be presented by the Maxwell fluid model. An extension of the Maxwell fluid model that adequately explains the behavior of both the relaxation phenomena and retardation phenomena is one Oldroyd-B fluid which is named after Oldroyd [1].

The Oldroyd-B fluid's Cauchy stress tensor is given by

$$\left\{ 1 + \lambda_1 \frac{D}{Dt} \right\} \mathbf{S} = \mu \left\{ 1 + \lambda_2 \frac{D}{Dt} \right\} \mathbf{A}_1, \quad (1.15)$$

where μ , $\frac{D}{Dt}$, and \mathbf{A}_1 are the dynamic viscosity, upper convective derivative, and first Rivlin-Ericksen tensor, respectively, λ_1 the relaxation time, and λ_2 the retardation time. This model reduces to Newtonian fluid model when ($\lambda_1 = \lambda_2 = 0$) and in Maxwell fluid model when ($\lambda_2 = 0$). Furthermore, non-Newtonian fluid deformation is related to \mathbf{S} , as described by the specific mathematical relation for a particular non-Newtonian fluid model.

1.5 Methods of computation

Both semi-analytical and numerical approaches are used to compute the results of highly non-linear ODEs that arise in the current theoretical analysis of Oldroyd-B material with energy transportation phenomenon under the influence of different physical factors produced by stretching surfaces. These methods include the homotopy analysis method (HAM) and the BVP

Midrich scheme. This section gives a brief overview of how these methods function.

1.5.1 Analytic solution scheme

The homotopy approach, first designed by Liao [70] in 1992, is a semi-analytical method for finding the series solution of highly nonlinear differential equations. This technique is based only on the topological notion of homotopy. It ensures that the approximation to the preferred solution of the given problem is deformed indefinitely. The homotopy operation is defined as $F : \mathbf{U} \times [0,1] \longrightarrow \mathbf{W}$ such that $F(\mathbf{u},0) = \psi_o(\mathbf{u})$ and $F(\mathbf{u},1) = \psi(\mathbf{u})$ with $\mathbf{u} \in \mathbf{U}$ where $\psi_o(\mathbf{u})$ and $\psi(\mathbf{u})$ two continuous deformable functions explained on topological space \mathbf{U} and \mathbf{W} . The method is preferable over the other conventional analytical methods such as the perturbation technique because this technique is unaffected by small or large physical restrictions. When compared to other approaches, it has some advantages, it allows us a lot of freedom in terms of selecting the base function and the linear operator. Moreover, it provides the assurance of convergence for highly non-linear problems.

Assume the non-linear DE of the form

$$\mathcal{L}[\ell(\eta)] = 0, \tag{1.16}$$

where ℓ and \mathcal{L} denote the unknown function and non-linear operator, respectively.

Now, assume the auxiliary linear operator \mathcal{L} , and $\ell_o(\eta)$ the initial approximation of $\ell(\eta)$. By introducing the non-zero auxiliary linear parameter \hbar the homotopy is constructed as the

zeroth order deformation equation

$$(1 - \epsilon)\mathcal{L}[\ell(\eta, \epsilon) - \ell_o(\eta)] = \epsilon\hbar\mathcal{L}[\ell(\eta)], \quad (1.17)$$

where $\epsilon \in [0, 1]$ is the embedding parameter.

When $\epsilon = 0$ and $\epsilon = 1$ we get

$$\ell(\eta, 0) = \ell_o(\eta) \text{ and } \ell(\eta, 1) = \ell(\eta), \quad (1.18)$$

the variation of $\ell(\eta, \epsilon)$ from $\ell_o(\eta)$ to $\ell(\eta)$ as ϵ varies from 0 to 1 is called continuous deformation.

This is the fundamental concept of HAM, and $\ell(\eta, \epsilon)$ can be expressed as a Taylor series expansion

$$\ell(\eta, \epsilon) = \ell_o(\eta) + \sum_{m=1}^{\infty} l_m(\eta)\chi^m, \quad l_m = \frac{1}{m!} \frac{\partial^m \ell(\eta, \epsilon)}{\partial q^m}. \quad (1.19)$$

The series in Eq. (1.20) is convergent at $\epsilon = 1$. Thus, the m^{th} order deformation problem is

$$\mathcal{L}[l_m(\eta) - \varkappa_m l_{m-1}(\eta)] = \hbar \mathfrak{R}_m(l_{m-1}), \quad (1.20)$$

with

$$\mathfrak{R}_m(l_{m-1}) = \frac{1}{(m-1)!} \left. \frac{\partial^{m-1} \ell(\eta, \epsilon)}{\partial q^{m-1}} \right|_{\epsilon=0}, \quad \varkappa_m = 0, \quad m \leq 1 \text{ and } \varkappa_m = 0, \quad m > 1. \quad (1.21)$$

The preceding computation is carried out using the Mathematica software.

1.5.2 BVP Midrich scheme

With extremely useful and effective techniques like Traprich, Trapdefer, Midrich, and Middefer, the numerical solution can be computed on the Maple software. The techniques of Midrich and Middefer are the midpoint approaches with identical enhancement strategies. The midpoint approach is a highly stable computational procedure that, when combined with Richardson extrapolation, yields highly accurate grid-independent solutions. By using domain truncation methodology, the region of the semi-infinite domain $[0, \infty)$ is first turned into the region of the finite domain $[0, N]$. The software algorithm adjusts the missing derivative until it achieves the desired convergence. The symbolic, highly efficient software Maple is used to conduct the numerical analyses. The general algorithm for the collocation method is as follows

$$\xi^{*'}(x) = F(x, \xi^*(x)), \quad \xi^*(x_o) = \xi_o^*. \quad (1.22)$$

The explicit midpoint method (Modified Euler method) has the following expression

$$\xi_{n+1}^* = \xi_n^* + hF\left(x_n + \frac{h}{2}, \xi_n^* + \frac{h}{2}F(x_n, \xi_n^*)\right), \quad (1.23)$$

where $x_n (= x_o + nh)$.

The method for the implied midpoint strategy is expressed as

$$\xi_{n+1}^* = \xi_l^* + hF\left(x_n + \frac{h}{2}, \xi_n^* + \frac{1}{2}(\xi_n^*, \xi_{n+1}^*)\right) \quad \text{where } n = 0, 1, 2, \dots \quad (1.24)$$

The method for determining the midpoint has a local error of order $O(h^3)$ and a global error of order $O(h^2)$ at separately step size. For better measurable intensive algorithms, the algorithm

error decays faster as $h \rightarrow 0$ and the solution becomes more stable.

1.6 Motivation and research objectives

A thorough review of the literature on non-Newtonian viscoelastic fluid flow with energy transport phenomenon in the preceding section demonstrated that researchers have been becoming more and more interested in the flow analysis of different non-Newtonian fluids with heat and mass transport by taking into account various physical factors. The majority of the investigations have been devoted to investigating this field of study. Based on previous work described in the literature, some gaps in the investigation of the flows of non-Newtonian viscoelastic Oldroyd-B fluid with energy transport induced by stretching geometry have been found. Also, this area of investigation is perhaps not concentrated on considerably and properly. The rheological attributes of the Oldroyd-B material induced by stretching surface are thus extremely open to investigation. Therefore, the main motivational objective of this thesis is to examine the analytical and numerical solutions to this highly non-linear model, so that we may accurately anticipate the rheological properties of viscoelastic Oldroyd-B material with the transport of thermal energy. The physical factors in this study apply to a variety of applications that includes, centrifugal pumps, plastic extrusion, polymers, gas turbine rotors, rotating machinery, and many more. Accordingly, in this study, we focus on these topics and try to fill up various gaps in the literature. Thus, the following are the main objectives of the current theoretical investigation:

- The flow phenomenon of Oldroyd-B nanofluid caused by stretching boundary is modeled in the form of PDEs, which are subsequently transformed into equivalent ODEs using the

appropriate flow ansatz.

- The transport phenomenon of thermal and solutal energy are investigated using different physical factors such as magnetic field, thermal radiation, Ohmic heating, chemical reaction, and heat source/sink in the system.
- With the aid of analytical and numerical solutions to the obtained governing equations, the flow structure of viscoelastic Oldroyd-B material with energy transport is evaluated, and the findings are displayed graphically as well as in tabular structure. A complete physical explanation of each outcome is provided. Furthermore, the results are validated in good agreement with the existing literature.

1.7 Thesis overview

The goal of this study is to acquire a better understanding of the flow phenomenon along with thermal and solutal transport of axisymmetric Oldroyd-B fluid flow induced by stretching surface. The exploration of energy transport and fluid flow characteristics for the rheology of Oldroyd-B material has been done in this dissertation using a comprehensive numerical and analytical methodologies. This section describes all of the analyses obtained during this study. Thus, the chapter format of the thesis is as obeys:

Chapter 1: A pertinent literature review to present work with motivation is provided in this chapter. There exist vast number of studies on linear and non-linear flows under various characteristics that are discussed. The thesis objectives are also given here. For the current investigation, the conservation laws and some specific material related to continuum mechanics are provided. Furthermore, the solution approaches used in the mathematical analysis are

briefly explained.

Chapter 2: The mathematical modeling of time-dependent two-dimensional Oldroyd-B fluid flow due to stretchable cylindrical surface is presented in this chapter. The energy transport features of Oldroyd-B material are explored employing an performance of the notable Buongiorno's model, which distinguishes the attractive features of Brownian motion and thermophoretic diffusion. The governing PDEs are converted into ODEs using appropriate similarity ansatz. The resultant equations are then tackled regarding the velocity, thermal, and solutal fields by operating the HAM. The study of this chapter is published in "**Ain Shams Eng. J., 14 (2023) 101825**".

Chapter 3: A numerical analysis is presented in this chapter to examine the thermal and solutal transport characteristics of Oldroyd-B nanofluid under the influence of source/sink phenomenon and first-order reaction rate. In addition, the Rosseland approximation for radiative heat transport is taken into account here. In Maple software, numerical integration in domain $[0, \infty)$ is performed for the flow model using the BVP Midrich scheme. For physical flow constraints, graphical results are prepared. This chapter findings were published in "**Phys. Scr., 96 (2021) 125266**".

Chapter 4: This chapter is prepared to analyze the Arrhenius activation energy impact on the non-linear radiative flow of magnetized Oldroyd-B fluid. An important characteristic of this initiative is taking into consideration the irregular heat generation/absorption effects to maintain the temperature of the fluid. The PDEs are transformed into an ODEs system using dimensionless quantities. Graphs are used to discuss and reveal the physical effects of dimensionless constraints on nanofluid velocity, thermal, and solutal distributions. The findings of this investigation are done in "**Waves Random Complex Media, (2022)**".

<https://doi.org/10.1080/17455030.2022.2135791>".

Chapter 5: The theoretical analysis in this chapter is designed to predict thermal energy transportation in time-dependent axisymmetric flow formed by a stretchable cylinder with thermophoretic particle deposition and Soret-Dufour effects. The nonlinear ordinary differential equations for this flow dynamics are converted into time-dependent partial differential equations, which are then analytically solved. The illustrated sketches are used to investigate the physical conduct of significant parameters in depth. The developments of this chapter are done in "**Int. Commun. Heat Mass Transf.**, **141 (2023) 106577**".

Chapter 6: This chapter examines the thermal features of the time-dependent stagnation region of viscoelastic Oldroyd-B material with the influence of the magnetic field. The thermal energy transport mechanism is studied using a non-Fourier approach rather than the conventional Fourier's law. The analysis of energy flow is also carried out for two different types of surface heating mechanisms, namely the prescribed surface temperature and the constant wall temperature. The acquired upshots are represented graphically. The results have been published in "**ZAMM (Z. fur Angew. Math. Mech.) DOI: 10.1002/zamm.202100393 (2023) e202100393**".

Chapter 7: This chapter contains an analysis of the heat transport characteristics of Oldroyd-B fluid during time-dependent axisymmetric flow. The energy transport phenomena are examined from the non-Fourier heat flux and homogeneous-heterogeneous reactions perspective, respectively. The Oldroyd-B fluid model's rheological formulation is used to create the governing flow field equations, which are then altered into a group of ODEs using the applicable similarity conversions. The graphical upshots for the velocity, thermal, and solutal distributions are derived. The physical behaviors of relevant factors are thoroughly explored.

The outcome raised in this chapter is reported in "**Alex. Eng. J., 74 (2023) 665-674**".

Chapter 8: The goal of this chapter is to use Buongiorno's model and Cattaneo-Cristov's theory to explain the thermal and solutal diffusion phenomena of Oldroyd-B nanofluid flow. The mathematical formulation section of this chapter describes the momentum, heat, and mass distribution equations. The effect of physical constraints on the flow, temperature, and concentration distributions of Oldroyd-B nanofluid are discussed through the HAM in Wolfram Mathematica. The findings are displayed graphically and physically justified. The consequences of this chapter are published in "**Waves Random Complex Media, (2022)** <https://doi.org/10.1080/17455030.2023.2172626>".

Chapter 9: Finally, the last chapter concludes this thesis and provides a summary of the work presented and suggests some recommendations for future work.

Chapter 2

Modelling of Unsteady Oldroyd-B

Fluid Flow due to Stretchable

Cylindrical Surface

In this chapter, the time-dependent flow and thermal transportation analysis of an incompressible Oldroyd-B nanofluid driven by a stretching cylinder are scrutinized with an analytical approach. The governing PDEs are first established, and then these PDEs are transformed into ODEs using appropriate similarity conversions. The acquired equations are then interpreted in the form of series solutions via the homotopy analysis method (HAM) for the velocity, temperature, and concentration fields. Additionally, the convergence analysis of the analytic series solutions is discussed. The aspects of thermophoresis and Brownian motion characteristics due to nanoparticles are studied by employing Buongiorno's model. The findings demonstrate that when the curvature parameter increases, the velocity, temperature, and concentration distributions near the cylinder's surface are enhanced. Moreover, the velocity profile, for

relaxation and the retardation times parameters, shows the opposite behavior. Also, the unsteadiness parameter enhances the fluid velocity. A comparison of some current and old results is remarkable.

2.1 Development of governing equations

For an incompressible fluid flow, the mathematical expressions for conservations of mass and momentum are, respectively

$$\nabla \cdot \mathbf{V} = 0, \quad (2.1)$$

$$\rho_f \mathbf{a} = -\nabla p + \nabla \cdot \mathbf{S}, \quad (2.2)$$

where \mathbf{a} signifies the material time derivative in term of velocity vector \mathbf{V} and is defined as

$$\mathbf{a} = \frac{d\mathbf{V}}{dt} = \frac{\partial \mathbf{V}}{\partial t} + (\mathbf{V} \cdot \nabla) \mathbf{V}. \quad (2.3)$$

For unsteady two-dimensional flow, the velocity field is

$$\mathbf{V} = [u(t, z, r), 0, w(t, z, r)], \quad (2.4)$$

where, u and w denote the velocity components in the z - and r -directions, respectively.

The divergence of equation (1.15) gives

$$\left\{ 1 + \lambda_1 \frac{D}{Dt} \right\} \nabla \cdot \mathbf{S} = \mu \left\{ 1 + \lambda_2 \frac{D}{Dt} \right\} \nabla \cdot \mathbf{A}_1. \quad (2.5)$$

After the implementation of $\left\{1 + \lambda_1 \frac{D}{Dt}\right\}$ on Eq. (2.2), and using Eq. (2.5), we have

$$\rho_f \left\{1 + \lambda_1 \frac{D}{Dt}\right\} \mathbf{a} = - \left\{1 + \lambda_1 \frac{D}{Dt}\right\} \nabla p + \mu \left\{1 + \lambda_2 \frac{D}{Dt}\right\} \nabla \cdot \mathbf{A}_1. \quad (2.6)$$

The first Rivlin-Ericksen tensor and upper convective derivative are, respectively, expressed as

$$\mathbf{A}_1 = \nabla \mathbf{V} + (\nabla \mathbf{V})^T, \quad (2.7)$$

$$\frac{D\mathbf{A}}{Dt} = \frac{\partial \mathbf{A}}{\partial t} + (\nabla \cdot \mathbf{V}) \mathbf{A} - (\nabla \mathbf{V}) \mathbf{A}. \quad (2.8)$$

Thus, the system of modelled differential equations for the flow problem are given below, under the assumptions mentioned above

$$\left. \begin{aligned} & \frac{\partial u}{\partial t} + u \frac{\partial u}{\partial z} + w \frac{\partial u}{\partial r} + \lambda_1 \left(\frac{\partial^2 u}{\partial t^2} + u^2 \frac{\partial^2 u}{\partial z^2} + w^2 \frac{\partial^2 u}{\partial r^2} + 2u \frac{\partial^2 u}{\partial t \partial z} + 2w \frac{\partial^2 u}{\partial t \partial r} + 2uw \frac{\partial^2 u}{\partial r \partial z} \right) \\ & = - \left(1 + \lambda_1 \frac{D}{Dt} \right) \frac{1}{\rho_f} \frac{\partial p}{\partial z} + \nu \left(\frac{\partial^2 w}{\partial r \partial z} + \frac{\partial^2 u}{\partial r^2} + 2 \frac{\partial^2 u}{\partial z^2} + \frac{1}{r} \frac{\partial w}{\partial z} + \frac{1}{r} \frac{\partial u}{\partial r} \right) \\ & + \nu \lambda_2 \left\{ \begin{aligned} & \frac{\partial^3 w}{\partial t \partial r \partial z} + \frac{\partial^3 u}{\partial t \partial r^2} + 2 \frac{\partial^3 u}{\partial t \partial z^2} + \frac{1}{r} \frac{\partial^2 w}{\partial t \partial z} + \frac{1}{r} \frac{\partial^2 u}{\partial t \partial r} + u \frac{\partial^3 w}{\partial r \partial z^2} + u \frac{\partial^3 u}{\partial z \partial r^2} + 2u \frac{\partial^3 u}{\partial z^3} \\ & + \frac{u}{r} \frac{\partial^2 w}{\partial z^2} + \frac{u}{r} \frac{\partial^2 u}{\partial z \partial r} + w \frac{\partial^3 w}{\partial r^2 \partial z} + w \frac{\partial^3 u}{\partial r^3} + 2w \frac{\partial^3 u}{\partial r \partial z^2} + \frac{w}{r} \frac{\partial^2 w}{\partial r \partial z} + \frac{w}{r} \frac{\partial^2 u}{\partial r^2} \\ & - \frac{w}{r^2} \frac{\partial w}{\partial z} - \frac{\partial u}{\partial z} \frac{\partial^2 w}{\partial r \partial z} - \frac{\partial u}{\partial z} \frac{\partial^2 u}{\partial r^2} - 2 \frac{\partial u}{\partial z} \frac{\partial^2 u}{\partial z^2} - \frac{1}{r} \frac{\partial u}{\partial z} \frac{\partial w}{\partial z} - \frac{1}{r} \frac{\partial u}{\partial z} \frac{\partial u}{\partial r} - 2 \frac{\partial u}{\partial r} \frac{\partial^2 w}{\partial r^2} \\ & - \frac{\partial u}{\partial r} \frac{\partial^2 u}{\partial z \partial r} - \frac{\partial u}{\partial r} \frac{\partial^2 w}{\partial z^2} - \frac{2}{r} \frac{\partial u}{\partial r} \frac{\partial w}{\partial r} + 2 \frac{w}{r^2} \frac{\partial u}{\partial r} \end{aligned} \right\}, \quad (2.9) \end{aligned}$$

$$\left. \begin{aligned}
& \frac{\partial w}{\partial t} + u \frac{\partial w}{\partial z} + w \frac{\partial w}{\partial r} + \lambda_1 \left(\frac{\partial^2 w}{\partial t^2} + u^2 \frac{\partial^2 w}{\partial z^2} + w^2 \frac{\partial^2 w}{\partial r^2} + 2u \frac{\partial^2 w}{\partial t \partial z} + 2w \frac{\partial^2 w}{\partial t \partial r} + 2uw \frac{\partial^2 w}{\partial r \partial z} \right) \\
& = - \left(1 + \lambda_1 \frac{D}{Dt} \right) \frac{1}{\rho_f} \frac{\partial p}{\partial r} + \nu \left(\frac{\partial^2 u}{\partial r \partial z} + \frac{\partial^2 w}{\partial z^2} + 2 \frac{\partial^2 w}{\partial r^2} + \frac{2}{r} \frac{\partial w}{\partial r} - \frac{2w}{r^2} \right) \\
& + \nu \lambda_2 \left\{ \begin{aligned}
& \frac{\partial^3 u}{\partial t \partial r \partial u} + \frac{\partial^3 w}{\partial t \partial z^2} + 2 \frac{\partial^3 w}{\partial t \partial r^2} + \frac{2}{r} \frac{\partial^2 w}{\partial t \partial r} - \frac{2}{r^2} \frac{\partial w}{\partial t} + 2u \frac{\partial^3 w}{\partial r \partial z^2} + u \frac{\partial^3 u}{\partial r \partial z^2} + u \frac{\partial^3 w}{\partial z^3} \\
& + 2 \frac{u}{r} \frac{\partial^2 w}{\partial r \partial z} + 2 \frac{u}{r^2} \frac{\partial w}{\partial z} + 2w \frac{\partial^3 w}{\partial r^3} + w \frac{\partial^3 u}{\partial z \partial r^2} + w \frac{\partial^3 w}{\partial r \partial z^2} + 2 \frac{w}{r} \frac{\partial^2 w}{\partial r^2} - \frac{4}{r^2} w \frac{\partial w}{\partial r} \\
& + 4 \frac{w^2}{r^3} + \frac{\partial w}{\partial z} \frac{\partial^2 w}{\partial r \partial z} + \frac{\partial w}{\partial z} \frac{\partial^2 u}{\partial r^2} + 2 \frac{\partial w}{\partial z} \frac{\partial^2 u}{\partial z^2} + \frac{1}{r} \left(\frac{\partial w}{\partial z} \right)^2 + \frac{1}{r} \frac{\partial w}{\partial z} \frac{\partial u}{\partial r} \\
& + 2 \frac{\partial w}{\partial r} \frac{\partial^2 w}{\partial r^2} + \frac{\partial w}{\partial r} \frac{\partial^2 u}{\partial r \partial z} + \frac{\partial w}{\partial r} \frac{\partial^2 w}{\partial z^2} + \frac{2}{r} \left(\frac{\partial w}{\partial r} \right)^2 - 2 \frac{w}{r^2} \frac{\partial w}{\partial r}
\end{aligned} \right\}, \quad (2.10)
\end{aligned} \right\}$$

where ν is the kinematic viscosity.

In view of the usual boundary layer approximations, we consider u , r , λ_1 , λ_2 , t , and p are of order 1, while z , and w are of order δ , and ν is of order δ^2 with δ as the boundary layer thickness. Therefore, Eqs. (2.9) and (2.10) are reduced to

$$\left. \begin{aligned}
& \frac{\partial u}{\partial t} + u \frac{\partial u}{\partial z} + w \frac{\partial u}{\partial r} + \lambda_1 \left(\frac{\partial^2 u}{\partial t^2} + u^2 \frac{\partial^2 u}{\partial z^2} + w^2 \frac{\partial^2 u}{\partial r^2} + 2u \frac{\partial^2 u}{\partial t \partial z} + 2w \frac{\partial^2 u}{\partial t \partial r} + 2uw \frac{\partial^2 u}{\partial r \partial z} \right) \\
& = - \left(1 + \lambda_1 \frac{D}{Dt} \right) \frac{1}{\rho_f} \frac{\partial p}{\partial z} + \nu \left(\frac{1}{r} \frac{\partial u}{\partial r} + \frac{\partial^2 u}{\partial r^2} \right) \\
& + \nu \lambda_2 \left\{ \begin{aligned}
& \frac{\partial^3 u}{\partial t \partial r^2} + \frac{1}{r} \frac{\partial^2 u}{\partial t \partial r} + u \frac{\partial^3 u}{\partial z \partial r^2} + \frac{u}{r} \frac{\partial^2 u}{\partial z \partial r} + w \frac{\partial^3 u}{\partial r^3} + \frac{w}{r} \frac{\partial^2 u}{\partial r^2} + \frac{w}{r^2} \frac{\partial u}{\partial r} \\
& - \frac{\partial u}{\partial z} \frac{\partial^2 u}{\partial r^2} - \frac{1}{r} \frac{\partial u}{\partial z} \frac{\partial u}{\partial r} - 2 \frac{\partial u}{\partial r} \frac{\partial^2 w}{\partial r^2} - \frac{\partial u}{\partial r} \frac{\partial^2 u}{\partial z \partial r} - \frac{2}{r} \frac{\partial u}{\partial r} \frac{\partial w}{\partial r}
\end{aligned} \right\}, \quad (2.11)
\end{aligned} \right\}$$

$$- \left(1 + \lambda_1 \frac{D}{Dt} \right) \frac{1}{\rho_f} \frac{\partial p}{\partial r} = 0. \quad (2.12)$$

The momentum equation's relevant boundary conditions are

$$\left. \begin{aligned}
& u(t, z, r) = \frac{az}{1-\alpha t}, \quad w(t, z, r) = 0 \text{ at } r = R \\
& u \rightarrow 0, \quad \frac{\partial u}{\partial r} \rightarrow 0 \text{ as } r \rightarrow \infty
\end{aligned} \right\}, \quad (2.13)$$

and the pressure gradient term can be calculated using the boundary layer approximations and

the boundary condition at infinity as

$$\frac{1}{\rho_f} \frac{\partial p}{\partial z} = 0. \quad (2.14)$$

2.2 Model sketch

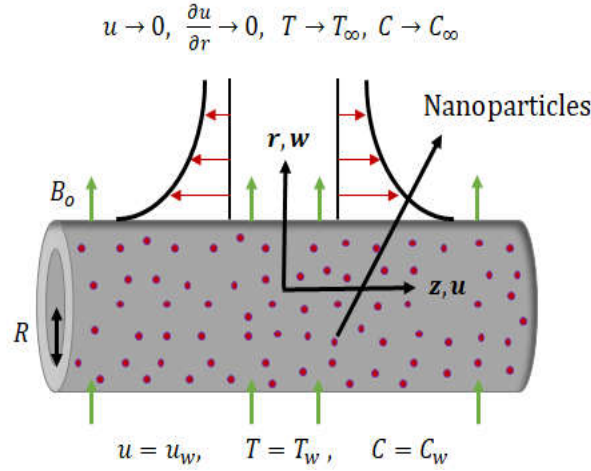


Fig. 2.1: The problem geometry.

2.3 Statement of the problem

Here, we consider the two-dimensional unsteady flow of an upper-convected Oldroyd-B nanofluid driven by a stretchable cylinder. The cylinder is stretched along the z -direction with velocity $u_w \left(= \frac{az}{1-\alpha t} \right)$ having radius R . The radius of the cylinder is the same as the order of the thickness of the boundary layer. Hence, the flow is assumed to be axisymmetric. The stretching cylinder velocity, which varies with time, introduces unsteadiness in the flow field. The flow starts at $t(=0)$ and it is steady when $t(<0)$. Cylindrical coordinates (z, r) are chosen in such a way that the z -axis is along the surface of the cylinder while the r -axis normal to the surface. The surface of cylinder is kept with a constant temperature T_w where $(T_w > T_\infty)$

corresponds to the heated surface while ($T_w < T_\infty$) is for the cooled surface. C_w and C_∞ denote the concentration at the surface and far away from the surface, respectively. **Fig. 2.1** shows the physical representation of the flow configuration.

Under the above-stated assumptions, the constitutive equations are given by

$$\frac{\partial(ru)}{\partial z} + \frac{\partial(rw)}{\partial r} = 0, \quad (2.15)$$

$$\left. \begin{aligned} & \frac{\partial u}{\partial t} + u \frac{\partial u}{\partial z} + w \frac{\partial u}{\partial r} + \lambda_1 \left\{ \frac{\partial^2 u}{\partial t^2} + u^2 \frac{\partial^2 u}{\partial z^2} + w^2 \frac{\partial^2 u}{\partial r^2} + 2u \frac{\partial^2 u}{\partial t \partial z} + 2w \frac{\partial^2 u}{\partial t \partial r} + 2uw \frac{\partial^2 u}{\partial r \partial z} \right\} \\ & = \nu \left(\frac{\partial^2 u}{\partial r^2} + \frac{1}{r} \frac{\partial u}{\partial r} \right) + \nu \lambda_2 \left\{ \begin{aligned} & \frac{\partial^3 u}{\partial t \partial r^2} + \frac{1}{r} \frac{\partial^2 u}{\partial t \partial r} + u \frac{\partial^3 u}{\partial z \partial r^2} \\ & + \frac{u}{r} \frac{\partial^2 u}{\partial z \partial r} + w \frac{\partial^3 u}{\partial r^3} + \frac{w}{r} \frac{\partial^2 u}{\partial r^2} + \frac{w}{r^2} \frac{\partial u}{\partial r} \end{aligned} \right\} \\ & - \nu \lambda_2 \left\{ \frac{\partial u}{\partial z} \frac{\partial^2 u}{\partial r^2} + \frac{1}{r} \frac{\partial u}{\partial z} \frac{\partial u}{\partial r} + 2 \frac{\partial u}{\partial r} \frac{\partial^2 w}{\partial r^2} + \frac{\partial u}{\partial r} \frac{\partial^2 u}{\partial z \partial r} + \frac{2}{r} \frac{\partial u}{\partial r} \frac{\partial w}{\partial r} \right\} \end{aligned} \right\}, \quad (2.16)$$

$$\frac{\partial T}{\partial t} + u \frac{\partial T}{\partial z} + w \frac{\partial T}{\partial r} = \frac{\alpha_1}{r} \frac{\partial}{\partial r} \left\{ r \frac{\partial T}{\partial r} \right\} + \tau \left\{ D_B \frac{\partial C}{\partial r} \frac{\partial T}{\partial r} + \frac{D_T}{T_\infty} \left(\frac{\partial T}{\partial r} \right)^2 \right\}, \quad (2.17)$$

$$\frac{\partial C}{\partial t} + u \frac{\partial C}{\partial z} + w \frac{\partial C}{\partial r} = \frac{D_B}{r} \frac{\partial}{\partial r} \left\{ r \frac{\partial C}{\partial r} \right\} + \frac{D_T}{T_\infty} \frac{1}{r} \frac{\partial}{\partial r} \left\{ r \frac{\partial T}{\partial r} \right\}, \quad (2.18)$$

with corresponding BCs

$$\left. \begin{aligned} & u = u_w, \quad w = 0, \quad T = T_w, \quad C = C_w \quad \text{at } r = R, \\ & u \rightarrow 0, \quad \frac{\partial u}{\partial r} \rightarrow 0, \quad T \rightarrow T_\infty \quad \text{and } C \rightarrow C_\infty \quad \text{as } r \rightarrow \infty \end{aligned} \right\}, \quad (2.19)$$

where $\alpha_1 \left(= \frac{k_1}{(\rho c)_f} \right)$ is the thermal diffusivity, $\nu \left(= \frac{\mu}{\rho_f} \right)$ the kinematic viscosity, $\tau \left(= \frac{(\rho c)_p}{(\rho c)_f} \right)$ the heat capacity ratio, T_w, C_w denote temperature and the nanoparticle concentration nearby the surface while T_∞, C_∞ denote the same far from the surface.

2.3.1 Similarity transformations

According to the flow ansatz [71], letting

$$\left. \begin{aligned} u &= \frac{az}{1-\alpha t} f'(\eta), \quad w = -\frac{R}{r} \sqrt{\frac{a\nu}{1-\alpha t}} f(\eta), \quad \theta = \frac{T-T_\infty}{T_w-T_\infty}, \\ \phi &= \frac{C-C_\infty}{C_w-C_\infty}, \quad \eta = \sqrt{\frac{a}{\nu(1-\alpha t)}} \left(\frac{r^2-R^2}{2R} \right) \end{aligned} \right\}, \quad (2.20)$$

which convert equations (2.16) to (2.19) into a system of ODEs as follow

$$\left. \begin{aligned} &(1 + 2\eta k) f''' + 2k f'' + f f'' - f'^2 - S f' - \frac{1}{2} \eta S f'' - \frac{De_1 k}{(1+2\eta k)} f^2 f'' \\ &+ De_1 \left\{ \begin{aligned} &2f f' f'' - 2S f'^2 - 2S^2 f' - \eta S f' f'' + 3S f f'' - f^2 f''' \\ &+ \eta S f f''' - \frac{7}{4} \eta S^2 f'' - \frac{1}{4} \eta^2 S^2 f''' \end{aligned} \right\} \\ &+ De_2 \left\{ \begin{aligned} &(1 + 2\eta k) \{ f''^2 + 2S f''' + \frac{1}{2} \eta S f^{iv} - f f^{iv} \} + 3S k f'' \\ &+ \eta S k f''' - 4k f f''' \end{aligned} \right\} = 0 \end{aligned} \right\}, \quad (2.21)$$

$$(1 + 2\eta k) \theta'' + 2k \theta' + \text{Pr} f \theta' - \frac{1}{2} \text{Pr} \eta S \theta' + (1 + 2\eta k) \text{Pr} \{ N_b \theta' \phi' + N_t \theta'^2 \} = 0, \quad (2.22)$$

$$(1 + 2\eta k) \phi'' + 2k \phi' + \text{Pr} Le f \phi' - \frac{1}{2} \text{Pr} Le \eta S \phi' + \frac{N_t}{N_b} \{ (1 + 2\eta k) \theta'' + 2k \theta' \} = 0, \quad (2.23)$$

with corresponding BCs

$$\left. \begin{aligned} &f(0) = 0, \quad f'(0) = 1, \quad \theta(0) = 1, \quad \phi(0) = 1 \\ &f'(\infty) = 0, \quad f''(\infty) = 0, \quad \theta(\infty) = 0, \quad \phi(\infty) = 0 \end{aligned} \right\}, \quad (2.24)$$

where De_1 is the fluid relaxation time, k the curvature parameter, De_2 the retardation times, S the unsteadiness parameter, N_t the thermophoresis parameter, N_b the Brownian motion parameter, Pr the Prandtl number, and Le the Lewis number are the dimensionless quantities,

which are respectively defined as

$$\left. \begin{aligned} De_1 &= \frac{\lambda_1 a}{1-\alpha t}, \quad k = \frac{1}{R} \sqrt{\frac{\nu(1-\alpha t)}{a}}, \quad De_2 = \frac{\lambda_2 a}{1-\alpha t}, \quad S = \frac{\alpha}{a}, \\ N_t &= \frac{\tau D_T (T_w - T_\infty)}{\nu T_\infty}, \quad N_b = \frac{\tau D_B (C_w - C_\infty)}{\nu}, \quad \text{Pr} = \frac{\nu}{\alpha_1}, \quad Le = \frac{\alpha_1}{D_B} \end{aligned} \right\}. \quad (2.25)$$

2.4 Engineering interest quantities

The engineering interest quantities (physical quantities) are defined as follow

2.4.1 Nusselt number

The Nusselt number can be used to describe the transportation of heat from the surface to the fluid. Mathematically,

$$Nu_z = \frac{z q_w}{k_1 (T_w - T_\infty)}, \quad (2.26)$$

where

$$q_w = -k_1 \left(\frac{\partial T}{\partial r} \right)_{r=R}. \quad (2.27)$$

In dimensionless form, we write

$$\frac{Nu_z}{\sqrt{\text{Re}_z}} = -\theta'(0). \quad (2.28)$$

2.4.2 Sherwood number

The Sherwood number is the rate of mass transport from the surface of the cylinder to the fluid. Mathematically,

$$Sh_z = \frac{z j_w}{D_B (C_w - C_\infty)}, \quad (2.29)$$

in which

$$j_w = -D_B \left(\frac{\partial C}{\partial r} \right)_{r=R}. \quad (2.30)$$

Thus, we have

$$\frac{Sh_z}{\sqrt{Re_z}} = -\phi'(0). \quad (2.31)$$

where $Re_z (= \frac{u_w z}{\nu})$ denotes the Reynold number.

2.5 Analytical solution procedure

Here, the homotopic technique is used for convergent series solutions of non-linear ODEs (2.21) to (2.23) along with BCs (2.24). For this, one requires the appropriate linear operators and initial guesses which are defined as

$$f_o(\eta) = (1 - e^{-\eta}), \quad \theta_o(\eta) = e^{-\eta} \quad \text{and} \quad \phi_o(\eta) = e^{-\eta}, \quad (2.32)$$

$$\mathcal{L}_f = \frac{\partial^3}{\partial \eta^3} - \frac{\partial}{\partial \eta}, \quad \mathcal{L}_\theta = \frac{\partial^2}{\partial \eta^2} - \theta \quad \text{and} \quad \mathcal{L}_\phi = \frac{\partial^2}{\partial \eta^2} - \phi, \quad (2.33)$$

satisfying

$$\mathcal{L}_f = [c_0 + c_1 e^\eta + c_2 e^{-\eta}], \quad \mathcal{L}_\theta = [c_3 e^\eta + c_4 e^{-\eta}] \quad \text{and} \quad \mathcal{L}_\phi = [c_5 e^\eta + c_6 e^{-\eta}], \quad (2.34)$$

where c_i ($i = 0, 1, 2, \dots, 6$) are constants.

2.5.1 Zeroth order formulation

One can write the problems corresponding to zeroth order as

$$\left. \begin{aligned} (1-p) \mathcal{L}_f \left\{ \hat{f}(\eta; p) - f_o(\eta) \right\} &= p \bar{h}_f \mathcal{N}_f \left\{ \hat{f}(\eta; p) \right\} \\ (1-p) \mathcal{L}_\theta \left\{ \hat{\theta}(\eta; p) - \theta_o(\eta) \right\} &= p \bar{h}_\theta \mathcal{N}_\theta \left\{ \hat{\theta}(\eta; p) \right\} \\ (1-p) \mathcal{L}_\phi \left\{ \hat{\phi}(\eta; p) - \phi_o(\eta) \right\} &= p \bar{h}_\phi \mathcal{N}_\phi \left\{ \hat{\phi}(\eta; p) \right\} \end{aligned} \right\}, \quad (2.35)$$

$$\left. \begin{aligned} \hat{f}(0; p) = 0, \hat{f}'(0; p) = 1, \hat{\theta}(0; p) = 1, \hat{\phi}(0; p) = 1 \\ \hat{f}'(\infty; p) = 0, \hat{f}''(\infty; p) = 0, \hat{\theta}(\infty; p) = 0, \hat{\phi}(\infty; p) = 0 \end{aligned} \right\}, \quad (2.36)$$

$$\left. \begin{aligned} \mathcal{N}_f \left\{ \hat{f}(\eta; p) \right\} &= (1 + 2\eta k) \hat{f}''' + 2k \hat{f}'' + \hat{f} \hat{f}'' - \hat{f}'^2 - S \hat{f}' - \frac{1}{2} \eta S \hat{f}'' \\ -De_1 \left\{ \begin{aligned} \frac{k}{(1+2\eta k)} \hat{f}^2 \hat{f}'' - 2\hat{f} \hat{f}' \hat{f}'' + 2S \hat{f}'^2 + 2S^2 \hat{f}' + \eta S \hat{f}' \hat{f}'' - 3S \hat{f} \hat{f}'' + \hat{f}^2 \hat{f}''' \\ + \frac{7}{4} \eta S^2 \hat{f}'' - \eta S \hat{f} \hat{f}''' + \frac{1}{4} \eta^2 S^2 \hat{f}''' \end{aligned} \right\} \\ +De_2 \left\{ (1 + 2\eta k) \left\{ \hat{f}''^2 + 2S \hat{f}'' - \hat{f} \hat{f}^{iv} + \frac{1}{2} \eta S \hat{f}^{iv} \right\} + 3S k \hat{f}'' + \eta S k \hat{f}''' - 4k \hat{f} \hat{f}''' \right\} \end{aligned} \right\}, \quad (2.37)$$

$$\left. \begin{aligned} \mathcal{N}_\theta \left\{ \hat{\theta}(\eta; p) \right\} &= (1 + 2\eta k) \hat{\theta}'' + 2k \hat{\theta}' + \text{Pr} \hat{f} \hat{\theta}' - \frac{1}{2} \text{Pr} \eta S \hat{\theta}' \\ &+ (1 + 2\eta k) \text{Pr} \left\{ N_b \hat{\theta}' \hat{\phi}' + N_t \hat{\theta}'^2 \right\} \end{aligned} \right\}, \quad (2.38)$$

$$\left. \begin{aligned} \mathcal{N}_\phi \left\{ \hat{\phi}(\eta; p) \right\} &= (1 + 2\eta k) \hat{\phi}'' + 2k \hat{\phi}' + \text{Pr} \text{Le} \hat{f} \hat{\phi}' - \frac{1}{2} \text{Pr} S \text{Le} \eta \hat{\phi}' \\ &+ \frac{N_t}{N_b} \left\{ (1 + 2\eta k) \hat{\theta}'' + 2k \hat{\theta}' \right\} \end{aligned} \right\}. \quad (2.39)$$

Here $p \in [0, 1]$ stands for embedding parameter, \mathcal{N}_f , \mathcal{N}_θ , and \mathcal{N}_ϕ for the non-linear operators, and \bar{h}_f , \bar{h}_θ and \bar{h}_ϕ for non zero auxiliary parameters.

Setting $p = 0$, and $p = 1$ we obtain

$$\left. \begin{aligned} \hat{f}(\eta, 0) &= f_o(\eta), \quad \hat{f}(\eta, 1) = f(\eta) \\ \hat{\theta}(\eta, 0) &= \theta_o(\eta), \quad \hat{\theta}(\eta, 1) = \theta(\eta) \\ \hat{\phi}(\eta, 0) &= \phi_o(\eta), \quad \hat{\phi}(\eta, 1) = \phi(\eta) \end{aligned} \right\}, \quad (2.40)$$

when we change p from 0 to 1, then $\hat{f}(\eta; p)$, $\hat{\theta}(\eta; p)$ and $\hat{\phi}(\eta; p)$ show the alteration from primary approximation's $f_o(\eta)$, $\theta_o(\eta)$ and $\phi_o(\eta)$ to desired ultimate solutions $f(\eta)$, $\theta(\eta)$ and $\phi(\eta)$.

By employing Taylor's series

$$\left. \begin{aligned} \hat{f}(\eta, p) &= f_o(\eta) + \sum_{m=1}^{\infty} f_m(\eta)p^m, \quad f_m(\eta) = \frac{1}{m!} \left. \frac{\partial^m \hat{f}(\eta; p)}{\partial p^m} \right|_{p=0} \\ \hat{\theta}(\eta, p) &= \theta_o(\eta) + \sum_{m=1}^{\infty} \theta_m(\eta)p^m, \quad \theta_m(\eta) = \frac{1}{m!} \left. \frac{\partial^m \hat{\theta}(\eta; p)}{\partial p^m} \right|_{p=0} \\ \hat{\phi}(\eta, p) &= \phi_o(\eta) + \sum_{m=1}^{\infty} \phi_m(\eta)p^m, \quad \phi_m(\eta) = \frac{1}{m!} \left. \frac{\partial^m \hat{\phi}(\eta; p)}{\partial p^m} \right|_{p=0} \end{aligned} \right\}, \quad (2.41)$$

the convergence regarding the equation (2.41) is based on the proper selections of \hbar_f , \hbar_θ , and \hbar_ϕ .

Choosing suited values of \hbar_f , \hbar_θ , and \hbar_ϕ so that equation (2.41) converge at $p = 1$, then

$$\left. \begin{aligned} f(\eta) &= f_o(\eta) + \sum_{m=1}^{\infty} f_m(\eta) \\ \theta(\eta) &= \theta_o(\eta) + \sum_{m=1}^{\infty} \theta_m(\eta) \\ \phi(\eta) &= \phi_o(\eta) + \sum_{m=1}^{\infty} \phi_m(\eta) \end{aligned} \right\}. \quad (2.42)$$

2.5.2 The $m - th$ order deformation

The $m - th$ order deformation problem is

$$\left. \begin{aligned} \mathcal{L}_f \{f_m(\eta) - \chi_m f_{m-1}(\eta)\} &= \hbar_f \mathcal{R}_f^m(\eta) \\ \mathcal{L}_\theta \{\theta_m(\eta) - \chi_m \theta_{m-1}(\eta)\} &= \hbar_\theta \mathcal{R}_\theta^m(\eta) \\ \mathcal{L}_\phi \{\phi_m(\eta) - \chi_m \phi_{m-1}(\eta)\} &= \hbar_\phi \mathcal{R}_\phi^m(\eta) \end{aligned} \right\}, \quad (2.43)$$

$$\left. \begin{aligned} f_m(0) = f'_m(0) = f'_m(\infty) = f''_m(\infty) = 0 \\ \theta_m(0) = \theta_m(\infty) = 0 \\ \phi_m(0) = \phi_m(\infty) = 0 \end{aligned} \right\}, \quad (2.44)$$

$$\left. \begin{aligned} \mathcal{R}_f^m(\eta) &= (1 + 2\eta k) f'''_{m-1} + 2k f''_{m-1} - S f'_{m-1} - \frac{1}{2} \eta S f''_{m-1} \\ &+ \sum_{k=0}^{m-1} [f_{m-1-k} f''_k - f'_{m-1-k} f'_k] - \frac{De_1 k}{(1+2\eta k)} \sum_{k=0}^{m-1} f_{m-1-k} \sum_{l=0}^k f_{k-l} f''_l \\ &+ De_1 \left\{ \begin{aligned} &2 \sum_{k=0}^{m-1} f_{m-1-k} \sum_{l=0}^k f'_{k-l} f''_l - \sum_{k=0}^{m-1} f_{m-1-k} \sum_{l=0}^k f_{k-l} f'''_l \\ &+ \sum_{k=0}^{m-1} \left\{ \begin{aligned} &-2S f'_{m-1-k} f'_k - \eta S f'_{m-1-k} f''_k + 3S f_{m-1-k} f''_k \\ &+ \eta S f_{m-1-k} f'''_k \end{aligned} \right\} \\ &-\frac{1}{4} \eta^2 S^2 f'''_{m-1} - \frac{7}{4} \eta S^2 f''_{m-1} - 2S^2 f'_{m-1} \end{aligned} \right\} \end{aligned} \right\}, \quad (2.45) \\ &+ De_2 \left\{ \begin{aligned} &(1 + 2\eta k) \left\{ \sum_{k=0}^{m-1} [f''_{m-1-k} f''_k - f_{m-1-k} f^{iv}_k] + \frac{1}{2} \eta S f^{iv}_{m-1} + 2S f'''_{m-1} \right\} \\ &-4k \sum_{k=0}^{m-1} f_{m-1-k} f'''_k + 3S k f''_{m-1} + \eta S k f'''_{m-1} \end{aligned} \right\} \end{aligned} \right\}$$

$$\left. \begin{aligned} \mathcal{R}_\theta^m(\eta) &= (1 + 2\eta k) \theta''_{m-1} + 2k \theta'_{m-1} + Pr \sum_{k=0}^{m-1} f_{m-1-k} \theta'_k - \frac{1}{2} Pr \eta S \theta'_{m-1} \\ &+ (1 + 2\eta k) Pr \sum_{k=0}^{m-1} \{N_b(\theta'_{m-1-k} \phi'_k) + N_t(\theta'_{m-1-k} \theta'_k)\} \end{aligned} \right\}, \quad (2.46)$$

$$\left. \begin{aligned} \mathcal{R}_\phi^m(\eta) &= (1 + 2\eta k) \phi''_{m-1} + 2k\phi'_{m-1} + \text{Pr} Le \sum_{k=0}^{m-1} f_{m-1-k} \phi'_k \\ &\quad - \frac{1}{2}\eta S \text{Pr} Le \phi'_{m-1} + \frac{N_t}{N_b} \{(1 + 2\eta k) \theta''_{m-1} + 2k\theta'_{m-1}\} \end{aligned} \right\}, \quad (2.47)$$

with

$$\chi_m = \begin{cases} 0, & \text{when } m \leq 1 \\ 1, & \text{when } m \geq 1 \end{cases} \quad (2.48)$$

The m -th order problem have the following solutions

$$\left. \begin{aligned} f_m(\eta) &= f_m^*(\eta) + c_0^* + c_1^* e^\eta + c_2^* e^{-\eta} \\ \theta_m(\eta) &= \theta_m^*(\eta) + c_3^* e^\eta + c_4^* e^{-\eta} \\ \phi_m(\eta) &= \phi_m^*(\eta) + c_5^* e^\eta + c_6^* e^{-\eta} \end{aligned} \right\}, \quad (2.49)$$

where $f_m^*(\eta)$, $\theta_m^*(\eta)$, and $\phi_m^*(\eta)$ represent the special solutions.

2.5.3 Convergence analysis

The HAM discussed in Sec. 2.5 includes auxiliary parameters h_f , h_θ and h_ϕ whose suitable values are required for the convergence of a series solution. For this, the least square error is

$$F_{f,m} = \frac{1}{N+1} \sum_{j=0}^N \left[N_f \sum_{i=0}^m F_j(i\Delta\eta) \right]^2. \quad (2.50)$$

In **Table 2.1**, we demonstrate the convergence region of analytic results for the non-dimension profiles. It is investigated that 15th order of estimation is enough for velocity while 18th order of estimation is enough for thermal and concentration distributions.

Table 2.1: Convergence analysis of the homotopy solutions for the different order of approximation when $k = S = 0.1$, $De_1 = De_2 = N_t = N_b = 0.2$, $Pr = 6.2$ and $Le = 1$.

Approximation order	$f''(0)$	$\theta'(0)$	$\phi'(0)$
1	1.137843	0.555314	0.281154
3	1.141838	0.568626	0.293529
6	1.151842	0.569407	0.295454
9	1.155231	0.571771	0.296730
12	1.158632	0.572436	0.297342
15	1.158613	0.573134	0.298730
18	1.158613	0.573129	0.298543
21	1.158613	0.573129	0.298543
24	1.158613	0.573129	0.298543

2.6 Validation of results

In **Table 2.2** present results are compared to check the exactness of the analytical outcomes with Abel *et al.* [72] and Megahed *et al.* [73] for Deborah number De_1 for fixed values of all other physical constraints. The current outcomes are found to be in excellent accord with their outcomes, indicating that the current numerical method produces reliable results.

Table 2.2: Obtained results of $-f''(0)$ for De_1 when $k = S = De_2 = 0$.

De_1	Abel <i>et al.</i> [72]	Megahed <i>et al.</i> [73]	Present results
0.0	1.0000000	0.9999780	1.000000
0.2	1.0519480	1.0519450	1.051838
0.4	1.1018500	1.1018480	1.101842
0.6	1.1501630	1.1501600	1.150231
0.8	1.1966920	1.1966900	1.197532
1.2	1.2852570	1.2852530	1.285317

2.7 Results and discussion

In this section, an explanation of the series solution with the impact of involved physical parameters on $f'(\eta)$, $\theta(\eta)$, and $\phi(\eta)$ are discussed in detail through graphs and tables. To understand the physical behavior of these graphical outcomes, the computations are carried out for $0.1 \leq De_1 \leq 3.0$, $0.1 \leq De_2 \leq 3.0$, $0.1 \leq k \leq 1.0$, $0.1 \leq S \leq 1.0$, $0.1 \leq N_t \leq 1.5$, $0.1 \leq N_b \leq 1.5$, $6.2 \leq Pr \leq 7.5$, and $0.1 \leq Le \leq 3.0$.

The consequence of the curvature parameter on dimensionless $f'(\eta)$, $\theta(\eta)$, and $\phi(\eta)$ distributions are illustrated in **Fig. 2.2(a)** to **(c)**, respectively. In **Fig. 2.2(a)**, the increasing values of the k radius of the cylinder decrease, therefore, fluid velocity enhance as a result of less resistance provided to the fluid motion. Further, the impact of k on $\theta(\eta)$ and $\phi(\eta)$ are captured in **Fig. 2.2(b)** and **(c)**. It is evident from these formations that the thermal and solutal distributions increase. Because, due to higher variation of curvature parameter the transfer

rate of heat and mass increases from cylinder to the fluid as a result enhancement occurs in temperature and concentration distributions.

Fig. 2.3(a) to **(c)** illustrate the variation in velocity, temperature, and concentration for higher estimation of unsteadiness parameter (S). It is evident from **Fig. 2.3(a)** that an improvement in unsteadiness parameter S increases the velocity. Physically, this implies that an increasing trend of S enhances the fluid acceleration which help to improves the velocity field. In **Fig. 2.3(b)** and **(c)** the unsteadiness parameter improve particle interactions, which indirectly helped to improve thermal conductivity. That's the reason of increasing in temperature, and concentration fields.

The impact of Deborah numbers that are in terms of fluid relaxation time (De_1) and retardation time (De_2) are shown in **Fig. 2.4(a)** and **(b)**, respectively. From these figures, we noted that the profile $f'(\eta)$ shows opposing behaviors for both De_1 and De_2 . As we know that De_1 and De_2 are proportionate to the relaxation time and the retardation time, accordingly. Therefore, an increase in relaxation time leads to stronger the elastic forces which controls the motion of a fluid due to which the fluid becomes like a solid that's why the fluid velocity decreases. In **Fig. 2.4(b)**, retardation time shows the opposite behavior on velocity profile as compared to relaxation time. In fact, elastic forces decrease due to an enlargement in the retardation phenomena, and hence, the velocity enhances. It is a well known that an increase in the relaxation time parameters results in a decrease the velocity of the fluid, while fluid velocity increases De_1 , while a growing pattern is noted when De_2 increases.

The variation of (N_t) on $\theta(\eta)$ and $\phi(\eta)$ are presented respectively in **Fig. 2.5(a)** and **(b)**. Here, the profiles and their related thickness layer are enhanced for increasing values of (N_t) . Physically, since the nanoparticles improve the fluid thermal conductivity and such thermal

conductivity establishes an increase in thermal and solutal curves.

In **Fig. 2.6(a)** we note that augmenting values of the Brownian movement parameter (N_b) enhances the thermal field. Because, due to higher values of Brownian motion parameter the interaction of particles boost up which increases the temperature distribution. While solutal distribution declines with the increase in (N_b). Because in this case, the collision of particles gives the disturbance for the mass transfer, that's why the solutal distribution decreases as portrayed in **Fig. 2.6(b)**.

The higher values of (Pr) and (Le) cause a deduction in $\theta(\eta)$ and nanoparticles solutal distribution $\phi(\eta)$, as shown in **Fig. 2.7(a)** and **(b)** respectively. Here, as we increase the Prandtl number, the temperature distribution $\theta(\eta)$ and related boundary layer thickness are decreased. Because Pr is the ratio between momentum diffusivity and thermal diffusivity. Thus increasing (Pr) lower the thermal diffusivity, which causes a reduction in temperature profile and the related boundary layer. Since the Lewis number depends upon the (D_B). An increase in (Le) leads to lower the (D_B). This lower coefficient of Brownian diffusion yields to lower the concentration distribution of nanoparticles.

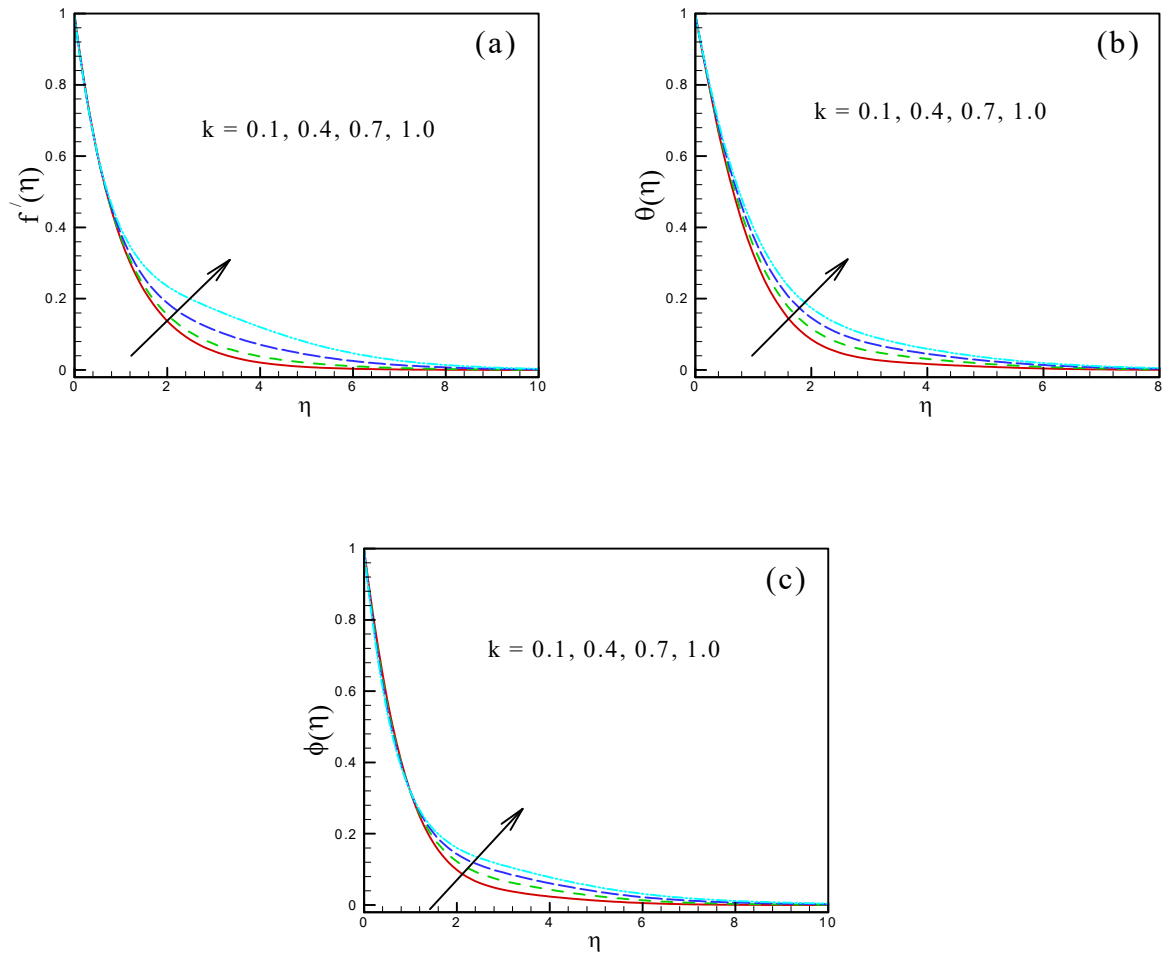


Fig. 2.2: The impact of k on (a): velocity profile (b): temperature and (c): concentration distribution.

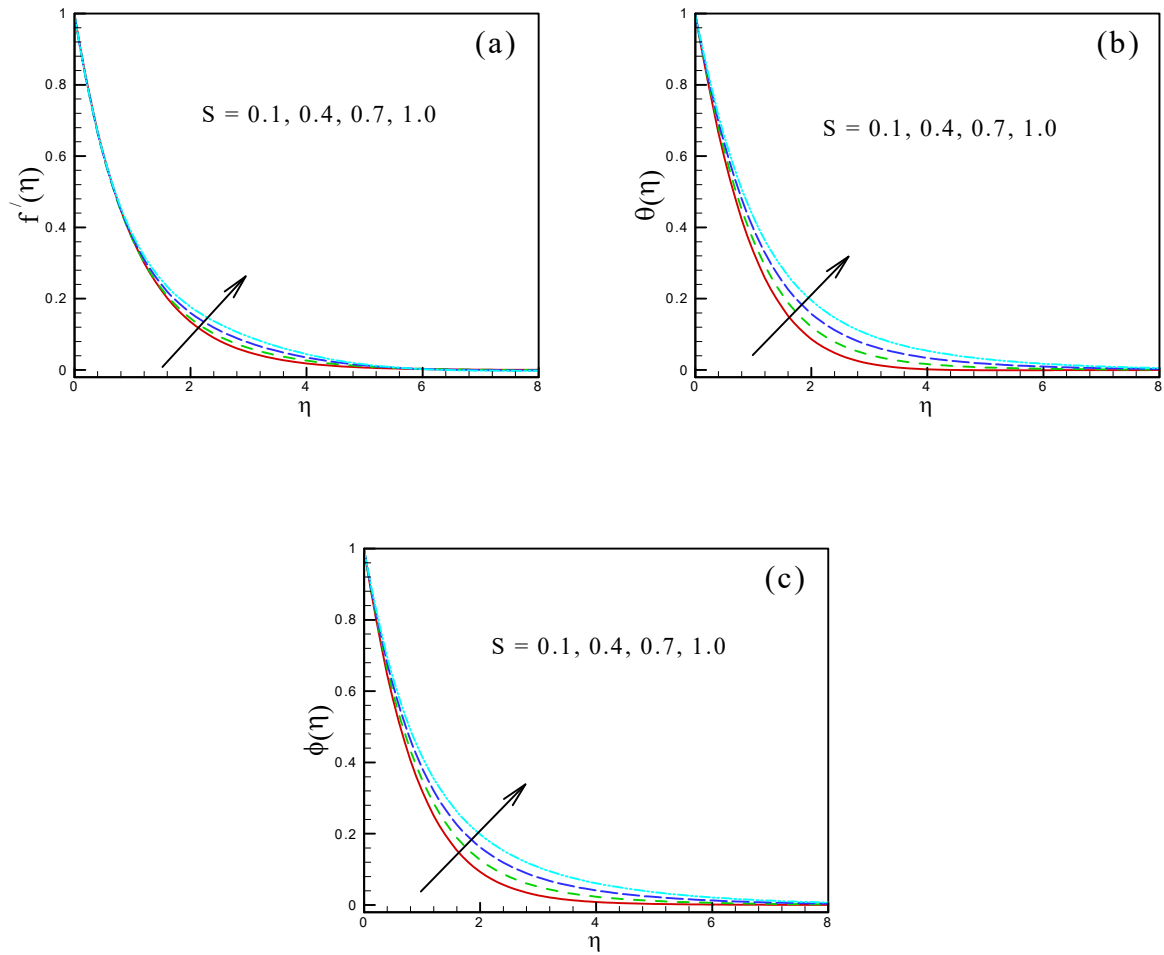


Fig. 2.3: The impact of S on (a): velocity profile (b): temperature and (c): concentration distribution.

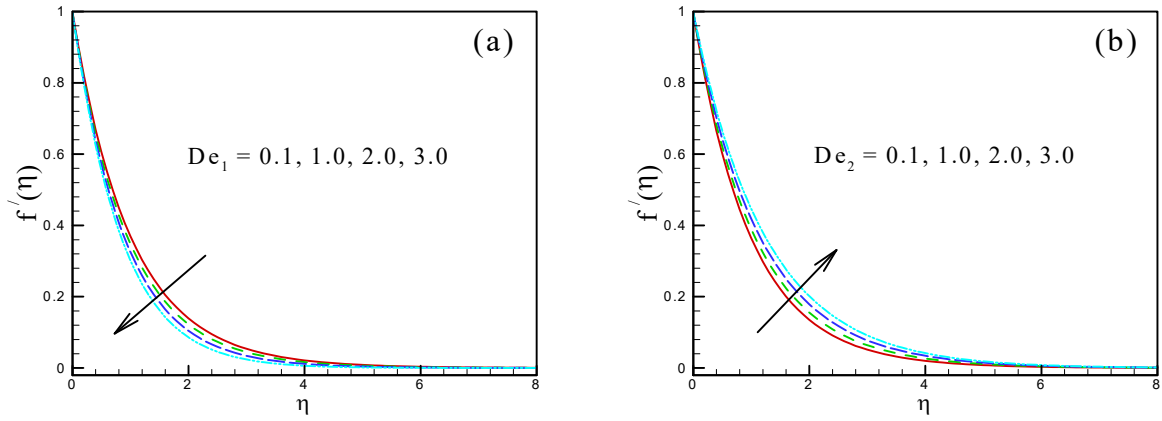


Fig. 2.4: The impact of De_1 and De_2 on velocity profile.

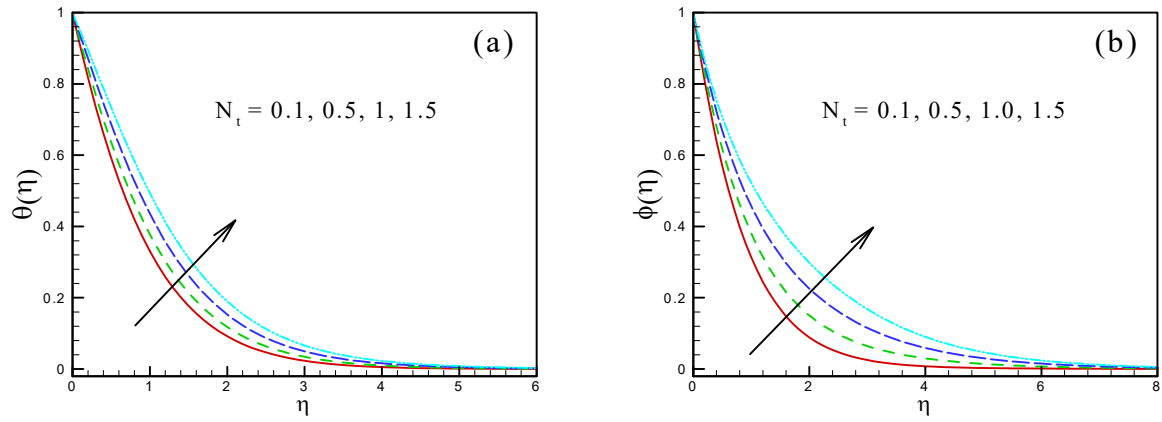


Fig. 2.5: The impact of N_t on (a): temperature and (b): concentration distribution.

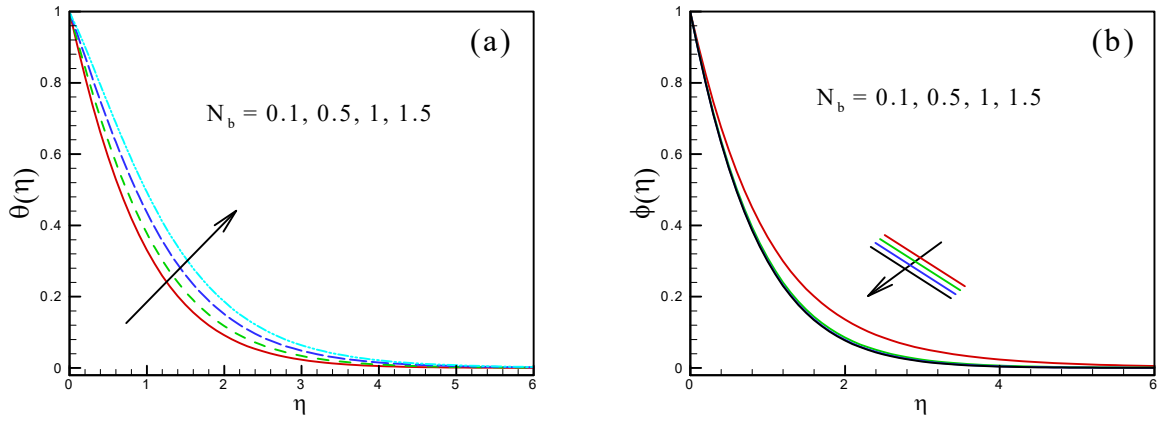


Fig. 2.6: The impact of N_b on (a): temperature and (b): concentration distribution.

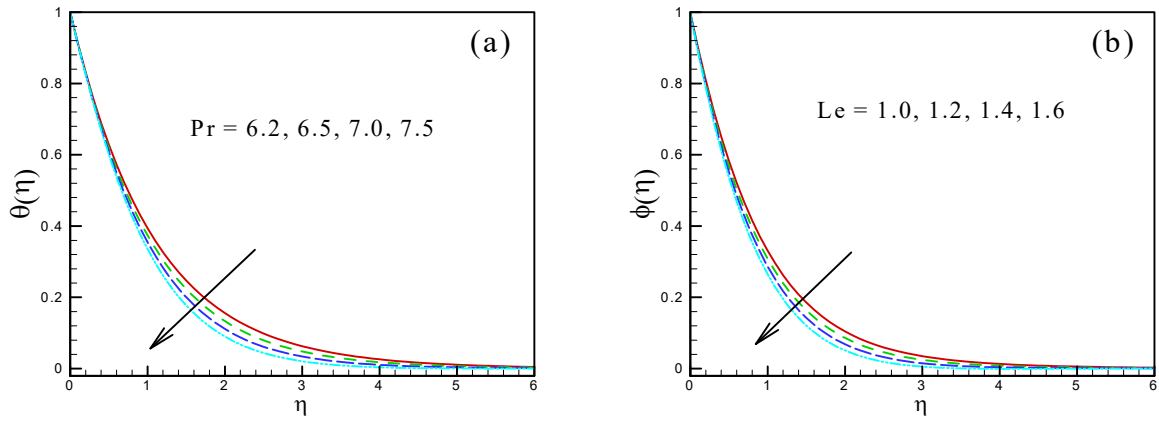


Fig. 2.7: The impact of Pr on (a): temperature and Lewis number Le on (b): concentration distribution.

2.8 Physical interpretation of engineering coefficient

The numerical results for $-\theta'(0)$ and $-\phi'(0)$ for De_1 , De_2 , k , S , N_t and N_b are displayed in **Table 2.4**. Here, the energy transfer rate declines for the progressive values of fluid relaxation time De_1 and fluid retardation time De_2 , respectively. Since the increasing values of De_1 and De_2 boost the relaxation and retardation phenomenon. Such increases conduct the depletion in energy transport rate. The transport rate of heat and mass increases for the increasing values of k . Because the resistance between the cylinder surface and the fluid falls as the radius of the cylinder lowers, as k increases, the resistance between the surface and the fluid decreases. Further, the unsteadiness parameter strengthened the particle interactions, which helps to improve the thermal conductivity indirectly, due to which the numerical values of $-\theta'(0)$ are increases. Further, the numerical results reveal that the energy transport rate decreases as the thermophoresis parameter and Brownian motion parameter values increase, whereas the mass transfer rate shows a reverse pattern.

Table 2.4: The calculated numerical values of $-\theta'(0)$ and $-\phi'(0)$.

De_1	De_2	k	S	N_t	N_b	$-\theta'(0)$	$-\phi'(0)$
0.1	0.1	0.1	0.1	0.1	0.1	0.6396972	1.3719886
0.2	-	-	-	-	-	0.6316371	1.3268961
0.3	-	-	-	-	-	0.6239911	1.2843645
0.1	0.1	0.1	0.1	0.1	0.1	0.6396972	1.3719886
-	0.2	-	-	-	-	0.6497337	1.4224082
-	0.3	-	-	-	-	0.6566886	1.4573653
0.1	0.1	0.1	0.1	0.1	0.1	0.6396972	1.3719886
-	-	0.3	-	-	-	0.6716092	1.4990627
-	-	0.5	-	-	-	0.7005311	1.6328715
0.1	0.1	0.1	0.1	0.1	0.1	0.6396972	1.3719886
-	-	-	0.2	-	-	0.7375931	1.3534494
-	-	-	0.3	-	-	0.8116354	1.3342672
0.1	0.1	0.1	0.1	0.1	0.1	0.6396972	1.3719886
-	-	-	-	0.2	-	0.5908652	1.3786006
-	-	-	-	0.3	-	0.5467763	1.4152298
0.1	0.1	0.1	0.1	0.1	0.1	0.6396972	1.3719886
-	-	-	-	-	0.2	0.4704245	1.5106871

Chapter 3

Convective Transport of Thermal and Solutal Energy in Unsteady MHD Oldroyd-B Nanofluid Flow

This chapter presents an analysis for the unsteady axisymmetric flow of an Oldroyd-B nanofluid generated by impermeable stretching cylinder with heat and mass transport under the influence of heat generation/absorption, thermal radiation and first-order chemical reaction. Additionally, thermal and solutal performances of nanofluid are studied using an interpretation of the well-known Buongiorno's model, which helps us to determine the attractive characteristics of Brownian motion and thermophoretic diffusion. For the governing non-linear ordinary differential equations, numerical integration in domain $[0, \infty)$ is carried out using the BVP Midrich scheme in Maple software. For the velocity, temperature and concentration distributions, reliable results are prepared for different physical flow constraints. According to the results, for increasing values of Deborah numbers, the temperature and concentration

distributions are higher in terms of relaxation time while these are declined in terms of retardation time. Moreover, thermal radiation and heat generation/absorption increases the temperature distribution and corresponding boundary layer thickness. With previously stated numerical values, the acquired solutions have an excellent accuracy.

3.1 Mathematical formulation

The time-dependent axisymmetric flow of an Oldroyd-B nanomaterials due to a stretching cylinder is considered here. The surface of cylinder is stretching with the velocity $u(t, z) = az/(1 - \alpha t)$, in which a denotes the stretching rate and α is a positive constant which measures the unsteadiness. The heat generation/absorption and first-order chemical reaction along with Brownian movement and thermophoresis effects are taken into consideration to study the characteristic of heat and mass transportation. Moreover, the convective transport of energy is assumed from surface of cylinder to fluid.

The model equations for the flow phenomena are Eqs. (2.16) to (2.19), (cf. Chapter 2)

$$\frac{\partial(ru)}{\partial z} + \frac{\partial(rw)}{\partial r} = 0, \quad (3.1)$$

$$= \frac{\nu}{r} \frac{\partial}{\partial r} \left(r \frac{\partial u}{\partial r} \right) + \nu \lambda_2 \left(\begin{array}{l} \frac{\partial^3 u}{\partial t \partial r^2} + \frac{1}{r} \frac{\partial^2 u}{\partial t \partial r} + u \frac{\partial^3 u}{\partial r^2 \partial z} + \frac{w}{r} \frac{\partial^2 u}{\partial r^2} + \frac{u}{r} \frac{\partial^2 u}{\partial z \partial r} + w \frac{\partial^3 u}{\partial r^3} + \frac{w}{r^2} \frac{\partial u}{\partial r} \\ - \frac{\partial u}{\partial z} \frac{\partial^2 u}{\partial r^2} - \frac{1}{r} \frac{\partial u}{\partial z} \frac{\partial u}{\partial r} - \frac{\partial u}{\partial r} \frac{\partial^2 u}{\partial r \partial z} - \frac{2}{r} \frac{\partial w}{\partial r} \frac{\partial u}{\partial r} - 2 \frac{\partial u}{\partial r} \frac{\partial^2 w}{\partial r^2} \\ - \frac{\sigma B_0^2}{\rho_f} \left(u + \lambda_1 \left\{ \frac{\partial u}{\partial t} + w \frac{\partial u}{\partial r} \right\} \right) \end{array} \right), \quad (3.2)$$

$$\left. \begin{aligned} \frac{\partial T}{\partial t} + u \frac{\partial T}{\partial z} + w \frac{\partial T}{\partial r} = \alpha_1 \left(\frac{\partial^2 T}{\partial r^2} + \frac{1}{r} \frac{\partial T}{\partial r} \right) - \frac{1}{(\rho c)_f} \left(\frac{1}{r} \frac{\partial}{\partial r} (r q_r) \right) + Q_o \left(\frac{T - T_\infty}{(\rho c)_f} \right) \\ + \frac{\sigma B_0^2 u^2}{(\rho c)_p} + \tau \left[D_B \frac{\partial C}{\partial r} \frac{\partial T}{\partial r} + \frac{D_T}{T_\infty} \left(\frac{\partial T}{\partial r} \right)^2 \right] \end{aligned} \right\}, \quad (3.3)$$

$$\frac{\partial C}{\partial t} + u \frac{\partial C}{\partial z} + w \frac{\partial C}{\partial r} = D_B \frac{1}{r} \frac{\partial}{\partial r} \left(r \frac{\partial C}{\partial r} \right) + \frac{D_T}{T_\infty} \frac{1}{r} \left(r \frac{\partial T}{\partial r} \right) - k_c (C_w - C_\infty), \quad (3.4)$$

and the corresponding BC's are

$$\left. \begin{aligned} u(t, z, r) = \frac{az}{(1-\alpha t)}, \quad w(t, z, r) = 0 \\ -k_1 \frac{\partial T}{\partial r} = h_t (T_w - T_\infty), \quad -D_B \frac{\partial C}{\partial r} = h_m (C_w - C_\infty) \quad \text{at } r = R \\ u \rightarrow 0, \quad \frac{\partial u}{\partial r} \rightarrow 0, \quad T \rightarrow T_\infty \quad \text{and } C \rightarrow C_\infty \quad \text{as } r \rightarrow \infty \end{aligned} \right\}. \quad (3.5)$$

In case of thermal radiation, the Rosseland approximation is used [74] and the radiative heat flux is defined as

$$q_r = \frac{-4\sigma^*}{3k^*} \frac{\partial T^4}{\partial r} = \frac{-16\sigma^*}{3k^*} T_\infty^3 \frac{\partial T}{\partial r}. \quad (3.6)$$

Using Eq. (3.6) in Eq. (3.3), we get

$$\left. \begin{aligned} \frac{\partial T}{\partial t} + u \frac{\partial T}{\partial z} + w \frac{\partial T}{\partial r} = \alpha_1 \left(\frac{\partial^2 T}{\partial r^2} + \frac{1}{r} \frac{\partial T}{\partial r} \right) + \frac{16\sigma^* T_\infty^3}{3k^* (\rho c)_f} \left(r \frac{\partial T}{\partial r} \right) + Q_o \left(\frac{T - T_\infty}{(\rho c)_f} \right) \\ + \frac{\sigma B_0^2 u^2}{(\rho c)_p} + \tau \left[D_B \frac{\partial C}{\partial r} \frac{\partial T}{\partial r} + \frac{D_T}{T_\infty} \left(\frac{\partial T}{\partial r} \right)^2 \right] \end{aligned} \right\}, \quad (3.7)$$

in which Q_o is the heat generation/absorption coefficient, k_c the reaction rate, k^* the mean absorption coefficient, σ^* the Stefan-Boltzmann constant, h_t and h_m represent the heat and mass transfer coefficients.

With the use of Eq. (2.20) (cf. Chapter 2), the PDEs are transformed as

$$\left. \begin{aligned} & (1 + 2\eta k) f''' + 2k f'' + f f'' - f'^2 - S f' - \frac{1}{2} \eta S f'' - \frac{De_1 k}{(1+2\eta k)} f^2 f'' \\ & + De_1 \left[\begin{array}{l} 2f f' f'' - f^2 f''' - 2S f'^2 - \eta S f' f'' + 3S f f'' + \eta S f f''' - \frac{1}{4} \eta^2 S^2 f''' \\ -\frac{7}{4} \eta S^2 f'' - 2S^2 f' \end{array} \right] \\ & + De_2 \left[(1 + 2\eta k) \{ f''^2 - f f^{iv} + \frac{1}{2} \eta S f^{iv} + 2S f''' \} - 4k f f''' + 3S k f'' + \eta S k f''' \right] \\ & - M \left(f' + \frac{De_1}{2} \eta S f'' + De_1 S f' - De_1 f f'' \right) = 0 \end{aligned} \right\}, \quad (3.8)$$

$$\left. \begin{aligned} & (1 + \frac{4}{3} R_d) \left[(1 + 2\eta k) \theta'' + 2k \theta' \right] + Pr f \theta' - \frac{1}{2} Pr \eta S \theta' + (1 + 2\eta k) Pr N_b \theta' \phi' \\ & + (1 + 2\eta k) Pr N_t \theta'^2 + Pr \delta^* \theta + Pr MEc f'^2 = 0 \end{aligned} \right\}, \quad (3.9)$$

$$\left. \begin{aligned} & (1 + 2\eta k) \phi'' + 2k \phi' + Pr Le f \phi' - \frac{1}{2} Pr Le \eta S \phi' + (1 + 2\eta k) \left(\frac{N_t}{N_b} \right) \theta'' + 2k \left(\frac{N_t}{N_b} \right) \theta' \\ & - Pr Le C_r \phi = 0 \end{aligned} \right\}, \quad (3.10)$$

with BCs as

$$\left. \begin{aligned} & f(0) = 0, f'(0) = 1, \theta'(0) = -\gamma_1 (1 - \theta(0)), \phi'(0) = -\gamma_2 (1 - \phi(0)), \\ & f'(\infty) = 0, f''(\infty) = 0, \theta(\infty) = 0, \phi(\infty) = 0 \end{aligned} \right\}. \quad (3.11)$$

In the above equations, $k \left(= \frac{1}{R} \sqrt{\frac{\nu(1-\alpha t)}{a}} \right)$ is the curvature parameter, $M \left(= \sqrt{\frac{\sigma B_0^2(1-\alpha t)}{a \rho_f}} \right)$ the magnetic parameter, $De_1 \left(= \frac{\lambda_1 a}{1-\alpha t} \right)$ and $De_2 \left(= \frac{\lambda_2 a}{1-\alpha t} \right)$ the Deborah numbers, $S \left(= \frac{\alpha}{a} \right)$ the unsteadiness parameter, $R_d \left(= \frac{4\sigma^* T_\infty^3}{k_1 k^*} \right)$ the thermal radiation parameter, $\delta^* \left(= \frac{Q_o(1-\alpha t)}{a(\rho c)_f} \right)$ the heat source/sink parameter, $N_b \left(= \frac{\tau D_B(C_w - C_\infty)}{\nu} \right)$ and $N_t \left(= \frac{\tau D_T(T_w - T_\infty)}{\nu T_\infty} \right)$ are Brownian motion and thermophoresis parameters, respectively. Moreover, $Ec \left(= \frac{u_w^2}{(\rho c)_p(T_w - T_\infty)} \right)$ is the Eckert number, $C_r \left(= \frac{k_c(1-\alpha t)}{a} \right)$ the chemical reaction parameter, $Pr \left(= \frac{\nu}{\alpha_1} \right)$ the Prandtl, $Le \left(= \frac{\alpha_1}{D_B} \right)$

the Lewis number and $\gamma_1 \left(= \frac{h_t}{k_1} \sqrt{\frac{\nu(1-\alpha t)}{a}} \right)$ and $\gamma_2 \left(= \frac{h_m}{D_B} \sqrt{\frac{\nu(1-\alpha t)}{a}} \right)$ are the Biot numbers.

3.2 Physical quantities

The physical quantities are

$$Nu_z = \frac{zq_w}{k_1(T_w - T_\infty)} \text{ and } Sh_z = \frac{zj_w}{D_B(C_w - C_\infty)}, \quad (3.12)$$

where q_w and j_w represent the heat and mass fluxes, respectively, and are defined as:

$$q_w = -k_1 \left(\frac{\partial T}{\partial r} \right)_{r=R} - \frac{4\sigma^* T_\infty^3}{3k^*} \left(\frac{\partial T}{\partial r} \right)_{r=R} \text{ and } j_w = -D_B \left(\frac{\partial C}{\partial r} \right)_{r=R}. \quad (3.13)$$

The normalized expressions for heat and mass transport are expressed as

$$Nu_z Re_z^{-\frac{1}{2}} = - \left(1 + \frac{4}{3} R_d \right) \theta'(0) \text{ and } Sh_z Re_z^{-\frac{1}{2}} = -\phi'(0). \quad (3.14)$$

3.3 Maple solutions

The general algorithm is as follows:

$$\xi^{*l}(x) = \zeta^*(x, \xi^*(x)), \quad \xi^*(x_o) = \xi_o^*. \quad (3.15)$$

The following is the expression for the explicit midpoint approach (Modified Euler method)

$$\xi_{n+1}^* = \xi_l^* + h\zeta^* \left(x_l + \frac{h}{2}, \xi_l^* + \frac{h}{2}\zeta(x_l, \xi_l^*) \right), \quad (3.16)$$

in which h denote the step-size, and $x_l (= x_o + lh)$.

The general procedure is written as

$$\xi_{l+1}^* = \xi_l^* + h\zeta^* \left(x_l + \frac{h}{2}, \xi_l^* + \frac{1}{2} (\xi_l^*, \xi_{l+1}^*) \right) \text{ where } l = 0, 1, 2, \dots \quad (3.17)$$

The method of determining the midpoint has a local error of order $O(h^3)$ and a global error of order $O(h^2)$. The algorithm error decays more quickly, and the solution becomes more reliable for more measurable intensive algorithms as $h \rightarrow 0$ increases.

3.4 Presentation of results

This section's goal is to investigate the effects of several non-dimensional flow parameters on the velocity, temperature and the concentration fields. Here, it is noted that all the plots asymptotically approaches the far field boundary conditions on fixed flow parameters $M = De_1 = De_2 = k = S = \delta^* = Ec = Cr = 0.1$, $N_t = N_b = 0.2$, $Pr = 6.2$, $Le = Rd = 1$ and $\gamma_1 = \gamma_2 = 1$ which are drawn in **Fig. 3.1** to **3.6**.

The consequence of parameter M on dimensionless profile $f'(\eta)$ and distribution $\theta(\eta)$ are underlined in **Fig. 3.1(a)** and **(b)**, subsequently. As with the enhancing strength of the magnetic field, the flow velocity curves diminished. Because the Lorentz forces produced due to the transverse magnetic field which delays down the fluid movement, that's why fluid velocity decreases. On contrary $M = 0.1, 0.3, 0.6, 0.9$, the temperature distribution is seen to be increases because the existence of magnetic field enhances the conduction of heat transfer and hence the corresponding thermal boundary-layer thickness is enlarged.

Due to the influence of Deborah number De_1 the dimensionless temperature and concen-

tration distributions are enhanced which are expressed via **Fig. 3.2(a)** and **(b)**, respectively. Deborah number De_1 depends upon the relaxation time [75]. The higher values of Deborah number increases the relaxation time. Its a well-known reality, those fluids which have higher relaxation time possess higher thermal and solutal while for smaller relaxation time fluids having lower thermal and solutal. In view of this discussion, the thermal and solutal profiles are enhanced through the larger values of De_1 . The consequence of De_2 on profiles $\theta(\eta)$ and $\phi(\eta)$ when $De_2 = 0.1, 0.4, 0.7, 1$ while other parameters are constant is discussed in **Fig. 3.3(a)** and **(b)**. From **Fig. 3.3(a)** and **(b)**, it can be clearly seen that De_2 decreases the temperature and concentration distributions. Deborah number De_2 depends upon retardation time [76]. The retardation time increases due to the higher values of De_2 . Such increase in the retardation time conducts the depletion in temperature and concentration distributions. Here, it's worth pointing out that when $De_1 = De_2 = 0$ the flow problem reduces to viscous fluid while when $De_2 = 0$ it corresponds to Maxwell fluid. From an experimental point of view, the value of De_2 is not greater than the values of De_1 .

The analysis for various values of Biot numbers γ_1 and γ_2 on temperature and concentration profiles are sketched through **Fig. 3.4(a)** and **(b)**, respectively. Both profiles have increasing behavior for thermal and solutal Biot numbers. Physically, larger Biot numbers decreases the resistance of energy transport at the surface because it involves energy transfer coefficients h_t and h_m , so with the increase of h_t and h_m thermal and solutal energy transport enhance in fluid flow.

A change in temperature field due to heat generation/absorption is illustrated in **Fig. 3.5(a)**. For heat absorption case ($\delta^* = -0.2, -0.1$) and heat generation case ($\delta^* = 0.1, 0.2$) the temperature distribution is declined and enhanced, respectively. This is due to the fact

that heat source/sink adds additional heat to the surface, the heat emitted inside the boundary layer increases, resulting in higher temperature field. Additionally, the corresponding boundary layer thickness is more heightened for heat generation in contrast to the heat absorption case. The impact of Eckert number ($Ec = 0.1, 0.3, 0.5, 0.7$) on the thermal field can be seen in **Fig. 3.5(b)**. Because Eckert number physically correlates to the intensity of resistive heating, so higher Eckert numbers produce more heat in the fluid, which increases the temperature field. In **Fig. 3.5(c)**, it is observed that the temperature distribution showing increasing trend for thermal radiation parameter R_d . Physically, it is verified as in the working fluid the heat is produced through radiation process so the temperature field enhances.

The change in generative/destructive chemical reaction (C_r) effects the profile $\phi(\eta)$ which is portrayed in **Fig. 3.6**. In case of generative chemical reaction ($C_r = -0.3, -0.1$), the concentration distribution increases slightly but it is falling for destructive chemical reaction ($C_r = 0.1, 0.3$). Because the mass transfer rate decreases when $C_r < 0$, which tends to enhance the concentration profile $\phi(\eta)$. Meanwhile, destructive chemical reactions have the opposite effect.

In **Table 3.1**, the values of $-\theta'(0)$ and $-\phi'(0)$ are calculated numerically and analytically against the different ranges of involved physical parameters M, N_t, N_b, De_1 and De_2 . The calculated results expose that $-\theta'(0)$ diminishes for the increasing values of M, De_1, De_2, N_t and N_b . Also, the solutal transport rate $-\phi'(0)$ drops against N_t, De_1 , and De_2 , and contrasting trends are seen against the values of N_b .

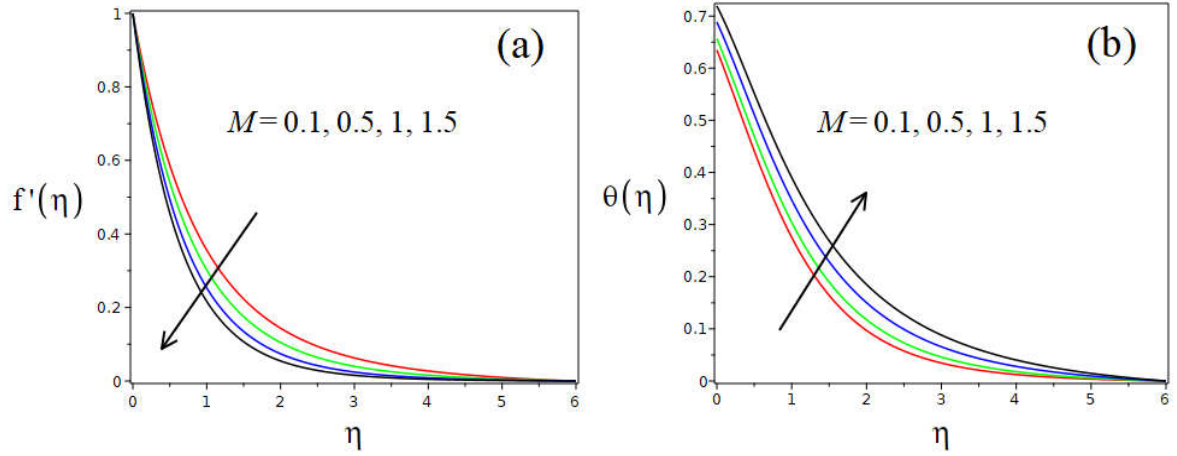


Fig. 3.1: The impact of Magnetic parameter (M) on (a): $f'(\eta)$ and (b): $\theta(\eta)$.

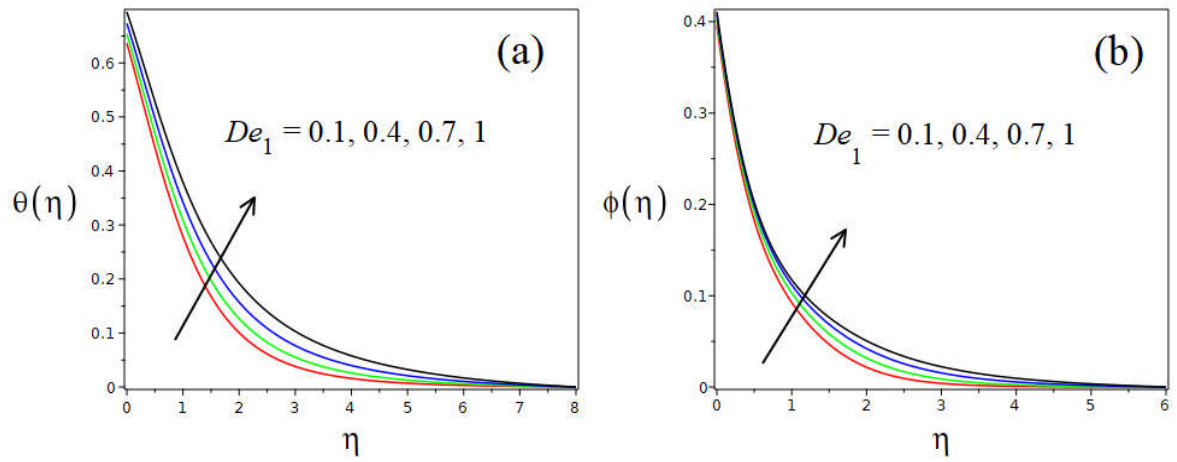


Fig. 3.2: The impact of Deborah number (De_1) on (a): $\theta(\eta)$ and (b): $\phi(\eta)$.

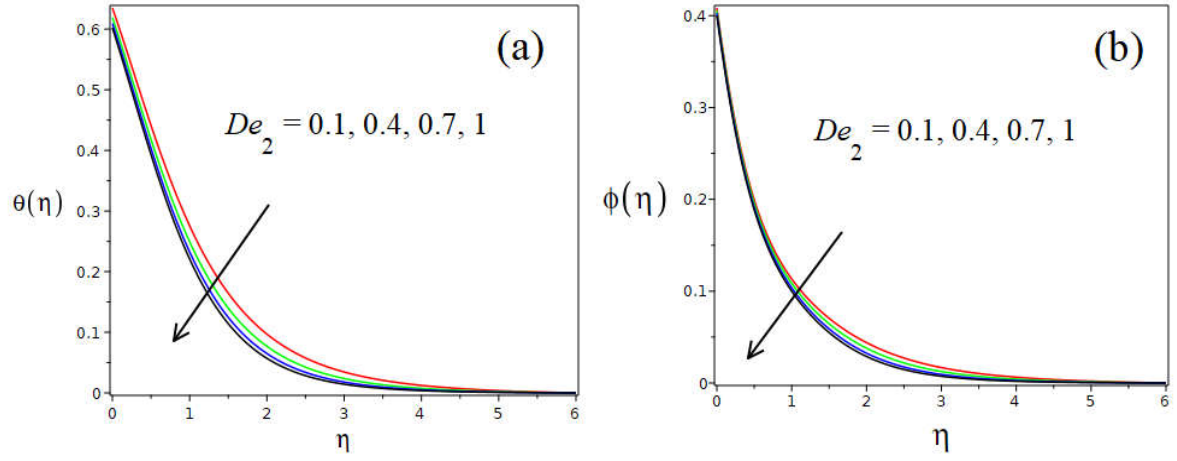


Fig. 3.3: The impact of Deborah number (De_2) on (a): $\theta(\eta)$ and (b): $\phi(\eta)$.

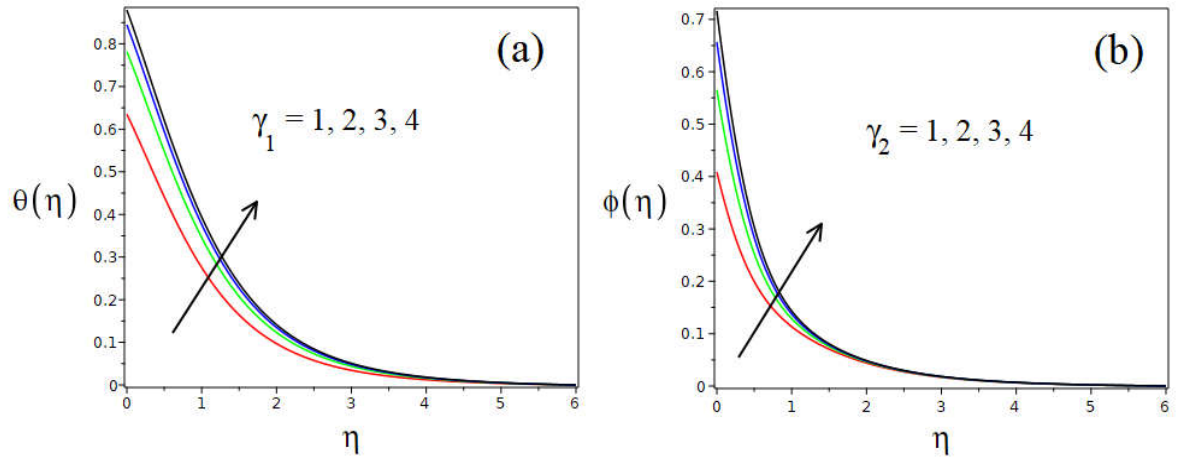


Fig. 3.4: The impact of Biot number γ_1 and γ_2 on (a): $\theta(\eta)$ and (b): $\phi(\eta)$.

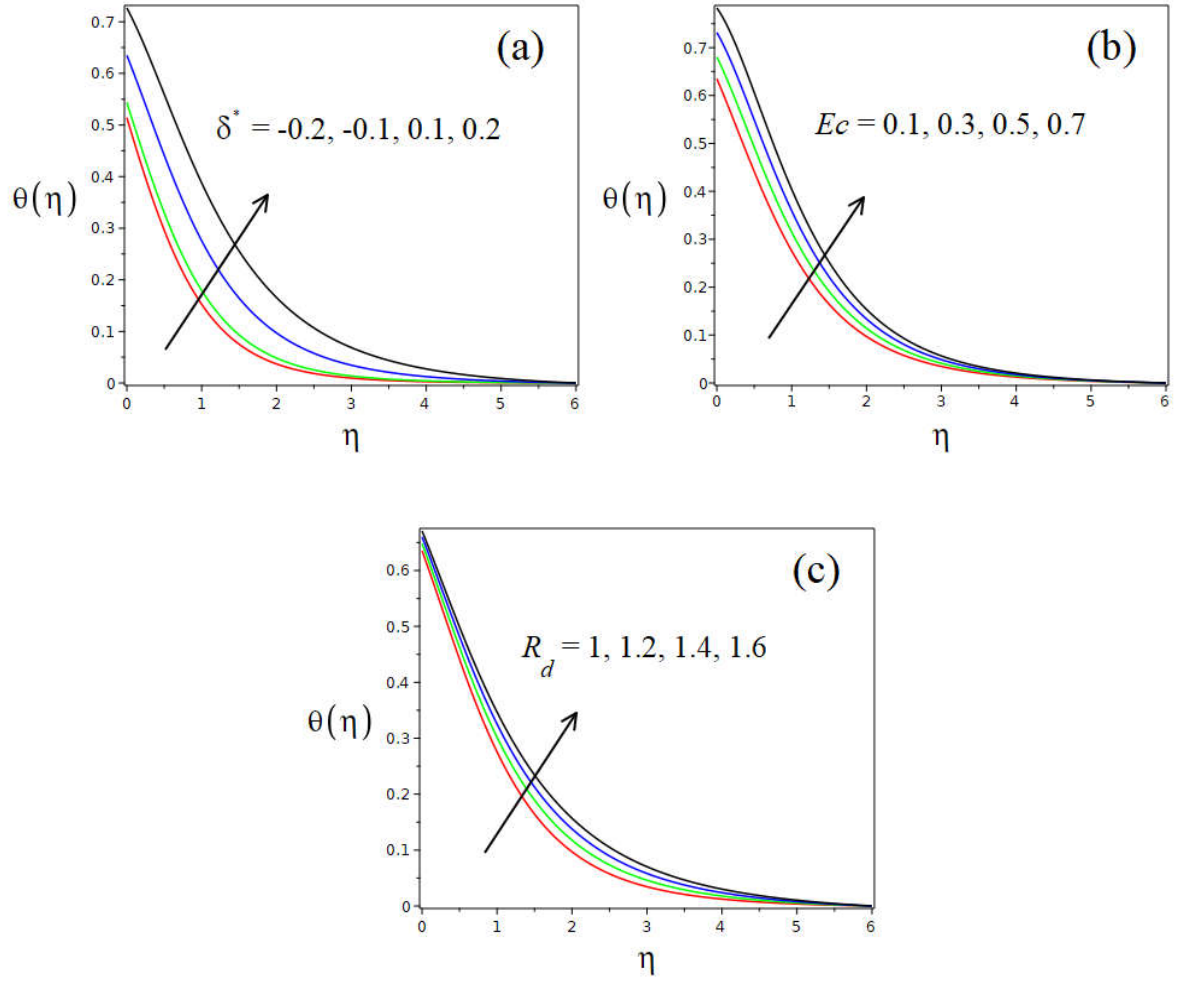


Fig. 3.5: The impact of heat source/sink parameter (δ^*), Eckert number (Ec) and thermal radiation (R_d) on $\theta(\eta)$.

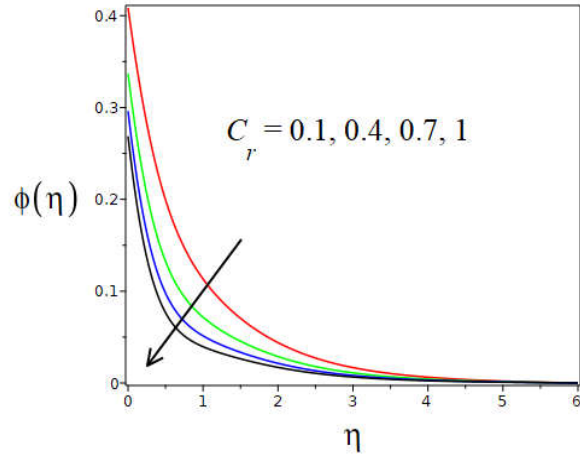


Fig. 3.6: The impact of chemical reaction parameter (C_r) on $\phi(\eta)$.

Table 3.1: The calculated values of $Nu_z Re_z^{-1/2}$ and $Sh_z Re_z^{-1/2}$ for M , De_1 , De_2 , N_t , and N_b when $k = S = R_d = \delta = Ec = Cr = 0.1$, $Pr = 6.2$ and $Le = \gamma_1 = \gamma_2 = 1$.

M	De_1	De_2	N_t	N_b	$Nu_z Re_z^{-1/2}$		$Sh_z Re_z^{-1/2}$	
					Numerical	Analytical	Numerical	Analytical
0.1	0.1	0.1	0.2	0.2	0.414912	0.414934	-	-
0.2	-	-	-	-	0.393993	0.393081	-	-
0.3	-	-	-	-	0.383227	0.3830267	-	-
0.1	0.1	0.1	0.2	0.2	0.364912	0.364586	2.714063	2.714964
-	0.3	-	-	-	0.354847	0.354751	2.635350	2.635165
-	0.5	-	-	-	0.344660	0.344036	2.574934	2.570243
0.1	0.1	0.1	0.2	0.2	0.414904	0.414904	0.364912	0.364036
-	-	0.3	-	-	0.400126	0.400126	2.440287	2.440701
-	-	0.5	-	-	0.391341	0.391341	2.280542	2.280924
0.1	0.1	0.1	0.2	0.2	1.564912	1.564782	1.894184	1.894634
-	-	-	0.4	-	1.350112	1.350062	1.430721	1.430920
-	-	-	0.6	-	1.195108	1.195005	1.180152	1.180843
0.1	0.1	0.1	0.2	0.2	0.964912	0.964042	2.398254	2.398636
-	-	-	-	0.4	0.634697	0.634803	2.534971	2.534843
-	-	-	-	0.6	0.314921	0.314231	2.694007	2.694194

3.4.1 Analysis authentication

To check the accurateness of the results produced by Maple software (Midrich scheme), a comparison of $-\theta'(0)$ is made in **Table 3.2**, for the limiting case. These table shows a fair correlation between current numerical findings and previous outcomes. Which ensures the accuracy of our numerical reports.

Table. 3.2: Comparison results of $-\theta'(0)$ for Prandtl number Pr.

Pr	Khan and Pop [77]	Ahmed <i>et al.</i> [78]	Present results
0.2	0.1691	-	0.169032
0.7	0.4539	0.453919	0.453753
1	-	0.581974	0.582132
1.5	-	0.760289	0.761456
2	0.9113	0.911156	0.911387

Chapter 4

Radiative Flow of Oldroyd-B

Nanofluid subject to Arrhenius

Activation Energy

It is generally known that the inclusion of nanoparticles improves the thermal conductivity of base liquids. Because of their improved thermophysical and rheological properties, these are appropriate for energy transport. The objective of this chapter is to investigate the thermal transport analysis of unsteady magnetohydrodynamic (MHD) Oldroyd-B nanofluid generated by an impermeable stretching cylinder. An important aspect of this endeavor is to add the effects of Arrhenius activation energy for modified Buongiorno's model of nanofluid. In an axisymmetric flow situation, boundary layer approximations are used to simulate the model equations of thermal energy, momentum, and, concentration for Oldroyd-B nanofluid. To convert the leading PDEs into a nonlinear ODEs system, dimensionless quantities are utilized. The physical consequences of the dimensionless constraints on nanofluid velocity, temperature,

and concentration are discussed and revealed via graphs. It is worth noting that enhancing the estimation of the activation energy parameter results in an increase in the nanoparticles concentration field. These findings also provide the impression that as the reaction rate parameter is increased, the rate of heat transfer over the surface of the cylinder drops. Additionally, with enhancing values of the temperature difference parameter, the thickness of the nanoparticles concentration layer depreciates.

4.1 Mathematical analysis

This chapter examines the time-dependent axisymmetric flow of a non-Newtonian Oldroyd-B fluid past a stretched cylinder with suspended nanoparticles. To study the flow analysis, we have adopted the (z, r) structure frame, with the z -axis aligned with the stretched cylinder and the r -axis constructed as normal to it. To properly represent heat transportation rate, non-linear thermal radiation with Ohmic heating and non-uniform heat source/sink are taken into account. The solutal transport in the system is calculated using a binary chemical reaction with Arrhenius activation energy. The flow problem for time-dependent Oldroyd-B nanofluid are (Eqs. (2.16) to (2.19), cf. Chapter 2)

$$\frac{\partial (ru)}{\partial z} + \frac{\partial (rw)}{\partial r} = 0, \quad (4.1)$$

$$\left. \begin{aligned} & \frac{\partial u}{\partial t} + u \frac{\partial u}{\partial z} + w \frac{\partial u}{\partial r} + \lambda_1 \left\{ \frac{\partial^2 u}{\partial t^2} + u^2 \frac{\partial^2 u}{\partial z^2} + w^2 \frac{\partial^2 u}{\partial r^2} + 2u \frac{\partial^2 u}{\partial t \partial z} + 2w \frac{\partial^2 u}{\partial t \partial r} + 2uw \frac{\partial^2 u}{\partial r \partial z} \right\} \\ & = \nu \left(\frac{\partial^2 u}{\partial r^2} + \frac{1}{r} \frac{\partial u}{\partial r} \right) + \nu \lambda_2 \left\{ \begin{aligned} & \frac{\partial^3 u}{\partial t \partial r^2} + \frac{1}{r} \frac{\partial^2 u}{\partial t \partial r} + u \frac{\partial^3 u}{\partial r^2 \partial z} + \frac{w}{r} \frac{\partial^2 u}{\partial r^2} + \frac{u}{r} \frac{\partial^2 u}{\partial z \partial r} \\ & + w \frac{\partial^3 u}{\partial r^3} + \frac{w}{r^2} \frac{\partial u}{\partial r} - \frac{\partial u}{\partial z} \frac{\partial^2 u}{\partial r^2} - \frac{1}{r} \frac{\partial u}{\partial z} \frac{\partial u}{\partial r} \\ & - \frac{\partial u}{\partial r} \frac{\partial^2 u}{\partial r \partial z} - \frac{2}{r} \frac{\partial w}{\partial r} \frac{\partial u}{\partial r} - 2 \frac{\partial u}{\partial r} \frac{\partial^2 w}{\partial r^2} \end{aligned} \right\} \\ & - \frac{\sigma B_o^2}{\rho_f} \left\{ u + \lambda_1 \left(\frac{\partial u}{\partial t} + w \frac{\partial u}{\partial r} \right) \right\} \end{aligned} \right\}, \quad (4.2)$$

$$\left. \begin{aligned} \frac{\partial T}{\partial t} + u \frac{\partial T}{\partial z} + w \frac{\partial T}{\partial r} &= \frac{k_1}{(\rho c)_f} \left\{ \frac{\partial^2 T}{\partial r^2} + \frac{1}{r} \frac{\partial T}{\partial r} \right\} + \frac{(\rho c)_p}{(\rho c)_f} \left\{ D_B \frac{\partial C}{\partial r} \frac{\partial T}{\partial r} + \frac{D_T}{T_\infty} \left(\frac{\partial T}{\partial r} \right)^2 \right\} \\ - \frac{1}{(\rho c)_f} \frac{1}{r} \frac{\partial}{\partial r} (r q_r) + \frac{\sigma B_0^2 u^2}{(\rho c)_f} + \frac{1}{(\rho c)_f} \frac{k_1 u_w}{\nu z} [A_1^* (T_w - T_\infty) f' + B_2^* (T - T_\infty)] & \end{aligned} \right\}, \quad (4.3)$$

$$\left. \begin{aligned} \frac{\partial C}{\partial t} + u \frac{\partial C}{\partial z} + w \frac{\partial C}{\partial r} &= \frac{D_B}{r} \frac{\partial}{\partial r} \left(r \frac{\partial C}{\partial r} \right) + \frac{D_T}{T_\infty} \frac{1}{r} \frac{\partial}{\partial r} \left(r \frac{\partial T}{\partial r} \right) \\ - k_r^2 e^{\left(\frac{-E_a}{k^{**} T} \right)} \left(\frac{T}{T_\infty} \right)^n (C - C_\infty) & \end{aligned} \right\}, \quad (4.4)$$

where A_1^* and B_2^* signify the coefficients of space and, temperature-dependent heat source/sink, respectively. It is important to keep in mind that the cases $A_1^* > 0$, and $B_2^* > 0$ correspond to internal heat generation, while $A_1^* < 0$, and $B_2^* < 0$ correspond to internal heat absorption, $\exp\left(\frac{-E_a}{k^{**} T}\right) \left(\frac{T}{T_\infty}\right)^n (C - C_\infty)$ the Arrhenius function, k_r^2 the chemical reaction rate constant, E_a the activation energy and n a constant exponent which lies in the range $(-1 < n < 1)$. The Rosseland approximation $q_r = \frac{-4\sigma^*}{3k^*} T^3 \frac{\partial T}{\partial r}$ is employed for the radiative heat.

The necessary boundary conditions are

$$\left. \begin{aligned} u = u_w = \frac{az}{1-\alpha t}, \quad w(t, z, r) = 0, \quad T = T_w \text{ and } C = C_w \text{ at } r = R \\ u \rightarrow 0, \quad \frac{\partial u}{\partial r} \rightarrow 0, \quad T \rightarrow T_\infty \text{ and } C \rightarrow C_\infty \text{ as } r \rightarrow \infty \end{aligned} \right\}. \quad (4.5)$$

After applying the similarity conversion given in Eq. (2.20) on Eqs. (4.1) to (4.4), we have

$$\left. \begin{aligned} (1 + 2\eta k) f''' + 2k f'' + f f'' - f'^2 - S f' - \frac{1}{2} \eta S f'' - \frac{De_1 k}{(1+2\eta k)} f^2 f'' \\ + De_1 \left\{ \begin{aligned} 2f f' f'' - f^2 f''' - 2S f'^2 - \eta S f' f'' + 3S f f'' + \eta S f f''' - \frac{1}{4} \eta^2 S^2 f''' \\ - \frac{7}{4} \eta S^2 f'' - 2S^2 f' \end{aligned} \right\} \\ + De_2 \left[(1 + 2\eta k) \left\{ f''^2 - f f^{iv} + \frac{1}{2} \eta S f^{iv} + 2S f''' \right\} - 4k f f''' + 3S k f'' + \eta S k f'''' \right] \\ - M \left(f' + \frac{De_1}{2} S f'' + De_1 S f' - De_1 f f'' \right) = 0 \end{aligned} \right\}, \quad (4.6)$$

$$\left. \begin{aligned} & \frac{1}{\text{Pr}} \frac{d}{d\eta} \left[(1 + 2\eta k) \left\{ 1 + R_d (1 + (\theta_w - 1)\theta)^3 \right\} \theta' \right] + f\theta' - \frac{1}{2}\eta S\theta' \\ & + (1 + 2\eta k) \left\{ N_b \theta' \phi' + N_t \theta'^2 \right\} + M E c f'^2 + A_1^* f' + B_2^* \theta = 0 \end{aligned} \right\}, \quad (4.7)$$

$$\left. \begin{aligned} & (1 + 2\eta k) \phi'' + 2k\phi' + S c f \phi' - \frac{1}{2}\eta S S c \phi' + \frac{N_t}{N_b} \left\{ (1 + 2\eta k) \theta'' + 2k\theta' \right\} \\ & - S c \sigma (1 + \Delta\theta)^n \exp\left(\frac{-E}{1+\Delta\theta}\right) \phi = 0 \end{aligned} \right\}, \quad (4.8)$$

with the boundary conditions as

$$\left. \begin{aligned} & f(0) = 0, \quad f'(0) = 1, \quad \theta(0) = 1, \quad \phi(0) = 1, \\ & f'(\infty) = 0, \quad f''(\infty) = 0, \quad \theta(\infty) = 0, \quad \phi(\infty) = 0 \end{aligned} \right\}. \quad (4.9)$$

In the above relation, the dimensionless parameters are: S the unsteadiness parameter, M the magnetic field, De_1 the fluid relaxation phenomena, k the curvature parameter, De_2 the fluid retardation phenomena, R_d the radiation parameter, N_t the thermophoresis parameter, N_b the Brownian parameter, Ec the Eckert number, θ_w the temperature ratio parameter, Pr the Prandtl number, Sc the Schmidt number, σ the chemical reaction rate constant, E the activation energy, and Δ the temperature difference parameter, respectively, and are expressed as

$$\left. \begin{aligned} & S = \frac{\alpha}{a}, \quad M = \sqrt{\frac{\sigma B_0^2 (1-\alpha t)}{a \rho_f}}, \quad De_1 = \frac{\lambda_1 a}{1-\alpha t}, \quad k = \frac{1}{R} \sqrt{\frac{\nu(1-\alpha t)}{a}}, \quad De_2 = \frac{\lambda_2 a}{1-\alpha t}, \\ & R_d = \frac{4\sigma^* T_\infty^3}{k_1 k^*}, \quad N_t = \frac{\tau D_T (T_w - T_\infty)}{\nu T_\infty}, \quad N_b = \frac{\tau D_B (C_w - C_\infty)}{\nu}, \quad Ec = \frac{u_w^2}{(\rho c)_p (T_w - T_\infty)}, \\ & \theta_w = \frac{T_w}{T_\infty}, \quad \text{Pr} = \frac{\nu}{\alpha_1}, \quad Sc = \frac{\nu}{D_B}, \quad \sigma = \frac{k_r^2 (1-\alpha t)}{a}, \quad E = \frac{E_a}{k^{**} T_\infty}, \quad \Delta = \frac{T_w - T_\infty}{T_\infty} \end{aligned} \right\}. \quad (4.10)$$

4.2 Quantities of interest

To calculate the thermal and solutal transportation rates, the expressions for physical parameters are

$$Nu_z = \frac{zq_w}{k_1(T_w - T_\infty)}, Sh_z = \frac{zj_w}{D_B(C_w - C_\infty)}, \quad (4.11)$$

where $q_w = -k_1 \left(\frac{\partial T}{\partial r}\right)_{r=R} - \frac{16\sigma^* T^3}{3k^*} \left(\frac{\partial T}{\partial r}\right)_{r=R}$ and $j_w = -D_B \left(\frac{\partial C}{\partial r}\right)_{r=R}$.

By using the usual similarity transformations, the dimensionless layout of the above quantities are expressed as

$$\left. \begin{aligned} Nu_z Re_z^{-\frac{1}{2}} &= -\left\{1 + \frac{4}{3}R_d(1 + (\theta_w - 1)\theta(0))^3\right\}\theta'(0) \\ Sh_z Re_z^{-\frac{1}{2}} &= -\phi'(0) \end{aligned} \right\}. \quad (4.12)$$

4.3 Solution methodology

As mentioned before, Liao [70] first introduces the concept of the homotopy analysis approach, which is employed in the current study to solve the highly nonlinear equations (4.6) to (4.8) with boundary conditions given in (4.9). This technique is unaffected by small or large physical restrictions. When compared to other approaches, it has some advantages. It allows us a lot of freedom in terms of selecting the command function and the operator [79]. This adaptability and independence help us to solve the highly nonlinear problems.

Letting

$$f_o(\eta) = 1 - e^{-\eta}, \theta_o(\eta) = e^{-\eta} \text{ and } \phi_o(\eta) = e^{-\eta}, \quad (4.13)$$

$$\mathcal{L}_f[f(\eta)] = f''' - f', \mathcal{L}_\theta[\theta(\eta)] = \theta'' - \theta \text{ and } \mathcal{L}_\phi[\phi(\eta)] = \phi'' - \phi, \quad (4.14)$$

satisfying

$$\mathcal{L}_f = c_0 + c_1e^\eta + c_2e^{-\eta}, \quad \mathcal{L}_\theta = c_3e^\eta + c_4e^{-\eta} \quad \text{and} \quad \mathcal{L}_\phi = c_5e^\eta + c_6e^{-\eta}, \quad (4.15)$$

where c_i ($i = 0, 1, 2, \dots, 6$) are constants.

4.4 Analysis of outcomes

This section describes the analytic solution along with the outcomes of the diverse flow parameters on the dimensionless flow field, thermal, and solutal distributions. We assigned the following fixed numerical values for the graphical results: $M = De_1 = De_2 = k = S = 0.1$, $A_1^* = B_2^* = 0.2$, $N_t = Ec = N_b = E = \sigma = n = \Delta = 0.1$, $Pr = 6.2$, $\theta_w = 1.1$, $Sc = R_d = 1.0$, which are drawn via **Fig. 4.1** to **Fig. 4.8** and all the plots asymptotically approach the far-field boundary conditions. In **Fig. 4.1(a)** and **(b)**, the consequence of Deborah numbers is explained in representation of fluid relaxation time De_1 and, retardation time De_2 , respectively. Based on these figures, it is concluded that fluid velocity and the associated boundary layer thickness behave in opposing ways for De_1 and De_2 . Since De_1 and De_2 are literally related to the relaxation and retardation phenomenon. Thus, an enlargement in relaxation time causes the elastic strengths that control fluid motion to become stronger, causing the fluid to behave more like a solid and therefore decreasing fluid velocity. In comparison to relaxation time, retardation time exhibits the opposing trend on the velocity profile as seen through **Fig. 4.1(b)**. In reality, as the retardation time increases, the elastic forces diminish, and the velocity improves. It is generally known that increasing the relaxation time parameters causes the fluid velocity to drop, but increasing De_1 causes the fluid velocity to increase, and increasing De_2 causes a growing

pattern. In **Fig. 4.2(a)** and **(b)** an increasing tendency is scrutinized for thermal, and solutal distribution for the higher assessment of unsteadiness parameter S . Because the unsteadiness strengthen the particle's interactions, which indirectly contributes to improving thermal conductivity. This is the reason for an increase in thermal and solutal transport. **Fig. 4.3(a)** and **(b)** show the effect of heat generation and absorption, respectively. From these formations, it is observed that internal heat generation causes the temperature profile to rise, whereas internal heat absorption generates the temperature to drop. The consequence of thermophoresis parameter on the temperature and concentration distributions are disclosed in **Fig. 4.4(a)** and **(b)**, respectively. Here, it is observed that higher values of N_t show an increasing tendency in both profiles. Physically, the presence of nanoparticles boosts the comparative thermal enhancement of the fluid. And such higher thermal conductivity correlates to a stronger thermophoretic force. Thus, the thermal and solutal curves improve as a result of the improved thermal conductivity. **Fig. 4.5(a)** and **(b)** have schemed to predict the outcomes of Brownian movement parameters on thermal and solutal transport. In **Fig. 4.5(a)**, the temperature field increases due to a rise in the thermal capacity of nanomaterials to the thermal capacity of the regular fluid, and therefore the temperature field increases. Further, it is observed that the concentration field diminishes for more heightened value of N_b . From the physical aspect, increasing the strength of N_b improves the Brownian motion of the nanoparticle's friction, which provides resistance to mass conduction in the fluid. To examine the nature of thermal transport for different values of R_d and θ_w , **Fig. 4.6(a)** and **(b)** are drawn. As the parameter R_d is increased, it is clear from **Fig. 4.6(a)** that the value of $\theta(\eta)$ is growing. This is owing to the fact that as the value of R_d boosts, the fluid absorbs more heat, causing $\theta(\eta)$ to increase. Similarly, in **Fig. 4.6(b)** it is discovered that as θ_w increases, both the related thickness and fluid temperature

$\theta(\eta)$ also improve. **Fig. 4.7(a)** and **(b)** portray the interpretation in solutal concentration with the deviation in temperature difference parameter Δ and dimensionless activation energy E . It has been found that the solute concentration decreases as δ increases. This suggests that the concentration boundary layer thickness grows as the temperature difference between the wall and the ambient temperature increases. Further, it is observed that rising the activation energy leads the concentration boundary layer to thicken. This is because lower temperature and heightened activation energy result in a smaller reaction rate constant, which slows down the chemical reaction. As a result, the solute concentration rises. In order to observe the effects of reaction rate σ and fitted rate constant n on solute concentration, respectively, **Fig. 4.8(a)** and **(b)** has been constructed. It can be shown that enlargement in either σ or n induces an expansion in the aspect $\sigma (1 + \Delta\theta)^n e^{\frac{-E}{1+\Delta\theta}}$. This eventually favors the reaction rate that causes concentration to increase. The decrease in $\phi(\eta)$ corresponds to a higher concentration gradient at the wall.

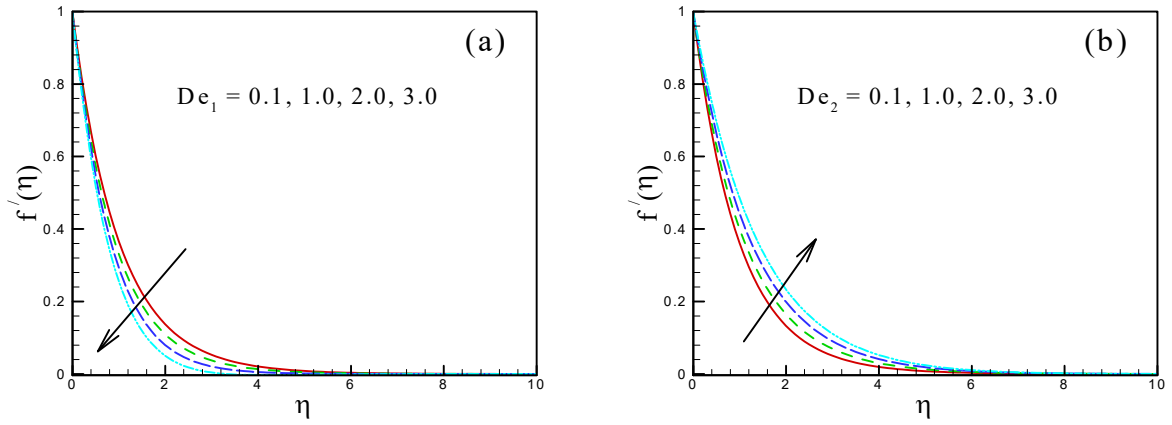


Fig. 4.1: Graph of $f'(\eta)$ versus (a): De_1 and (b): De_2 .

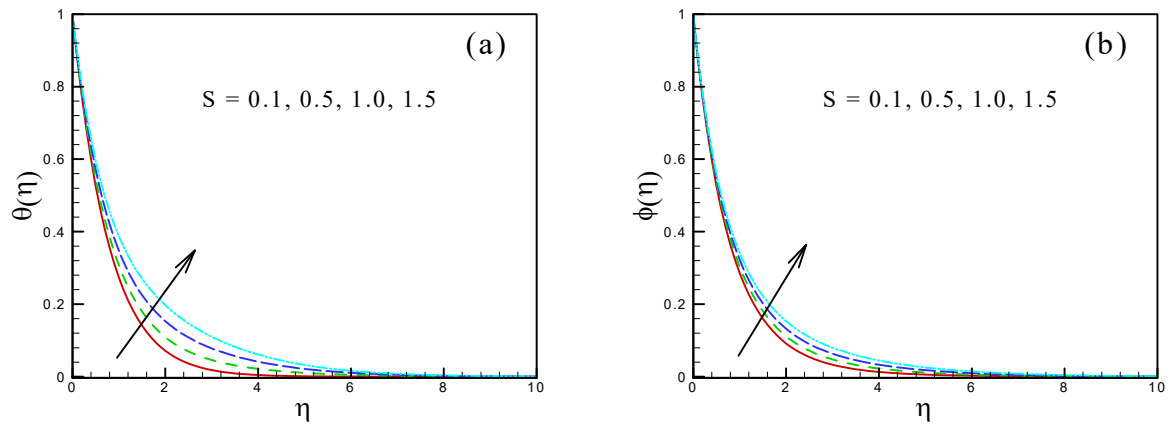


Fig. 4.2: Graph of $\theta(\eta)$ and $\phi(\eta)$ versus S .

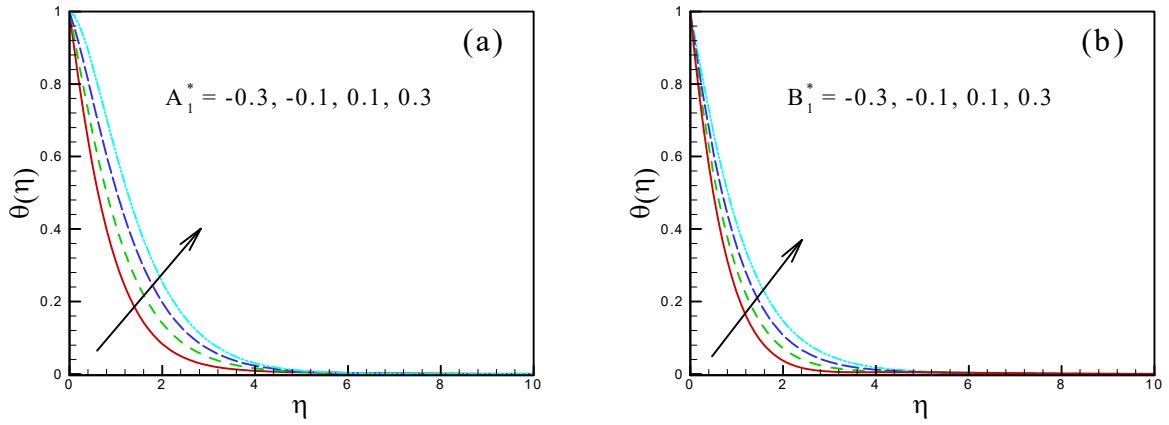


Fig. 4.3: Graph of $\theta(\eta)$ versus (a): A_1^* and (b): B_1^* .

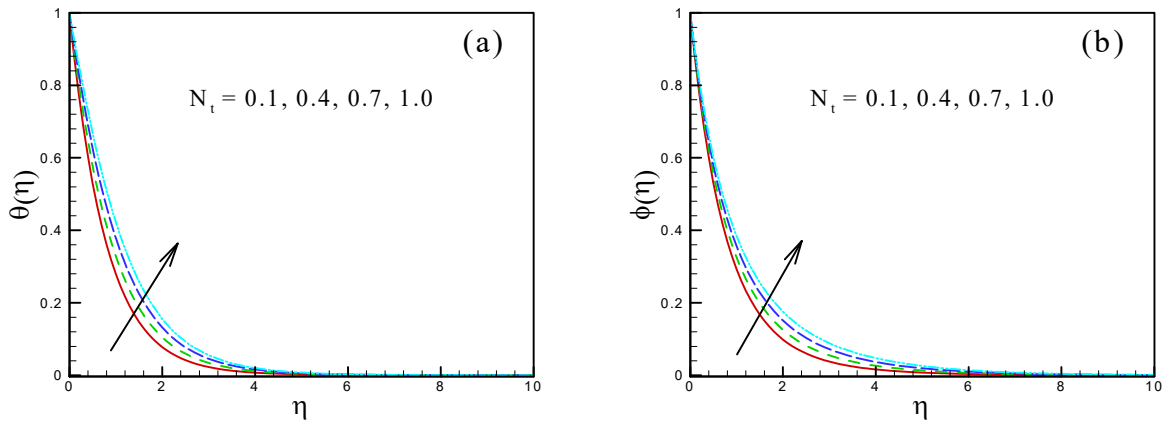


Fig. 4.4: Graph of $\theta(\eta)$ and $\phi(\eta)$ versus N_t .

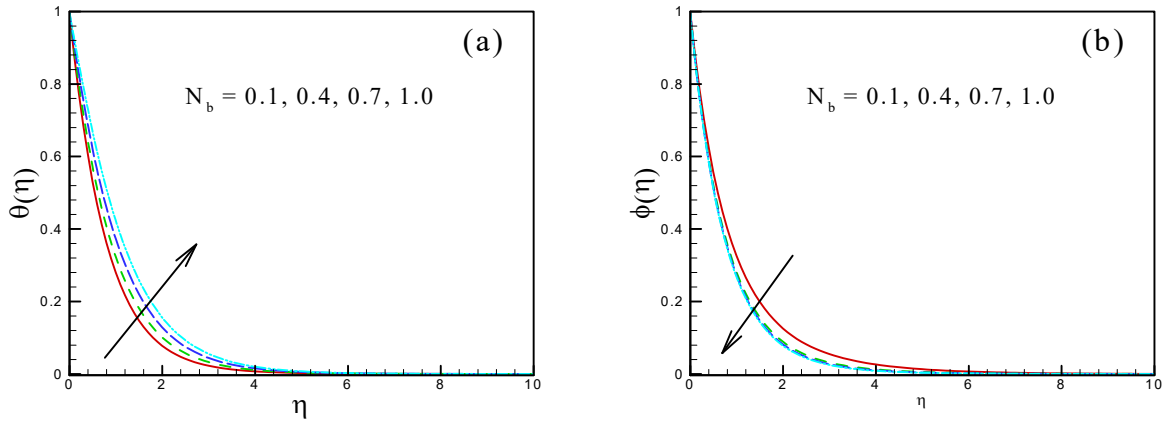


Fig. 4.5: Graph of $\theta(\eta)$ and $\phi(\eta)$ versus N_b .

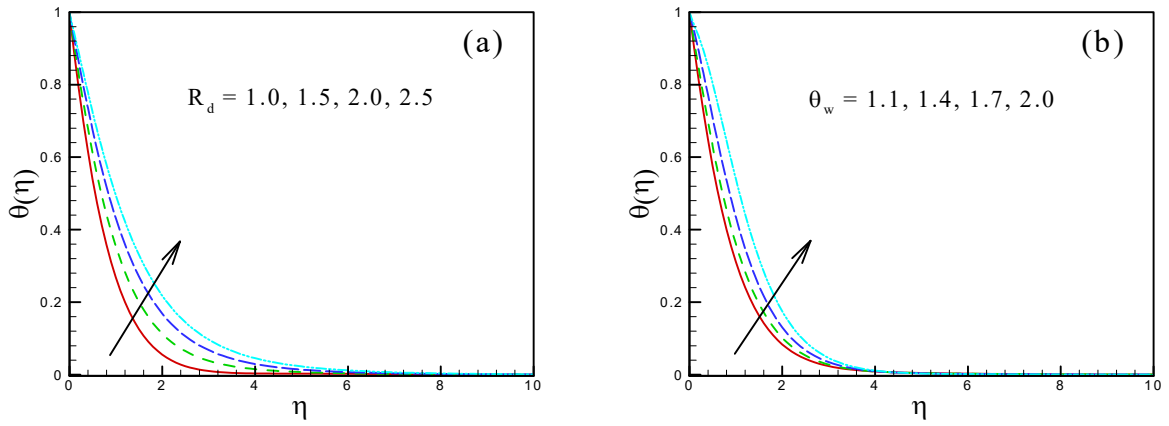


Fig. 4.6: Graph of $\theta(\eta)$ versus (a): R_d and (b): θ_w .

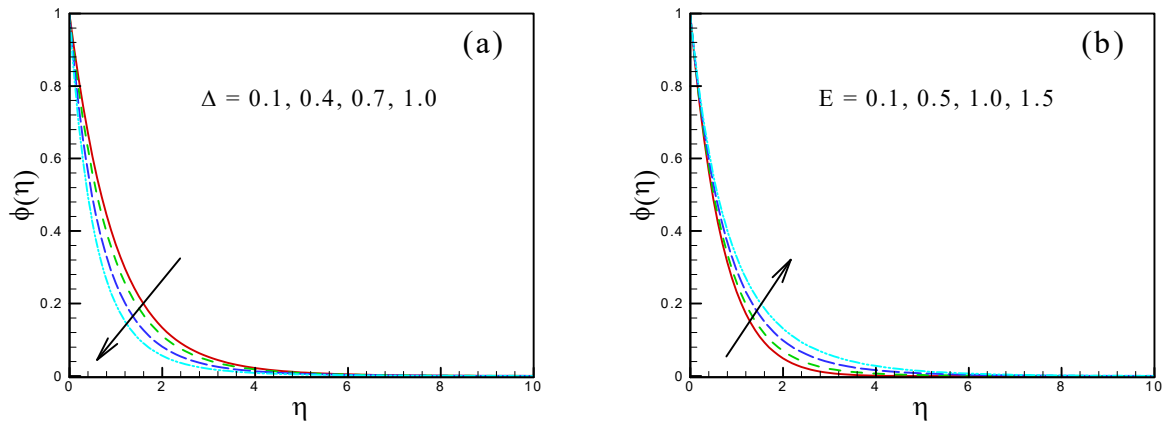


Fig. 4.7: Graph of $\phi(\eta)$ versus (a): Δ and (b): E .

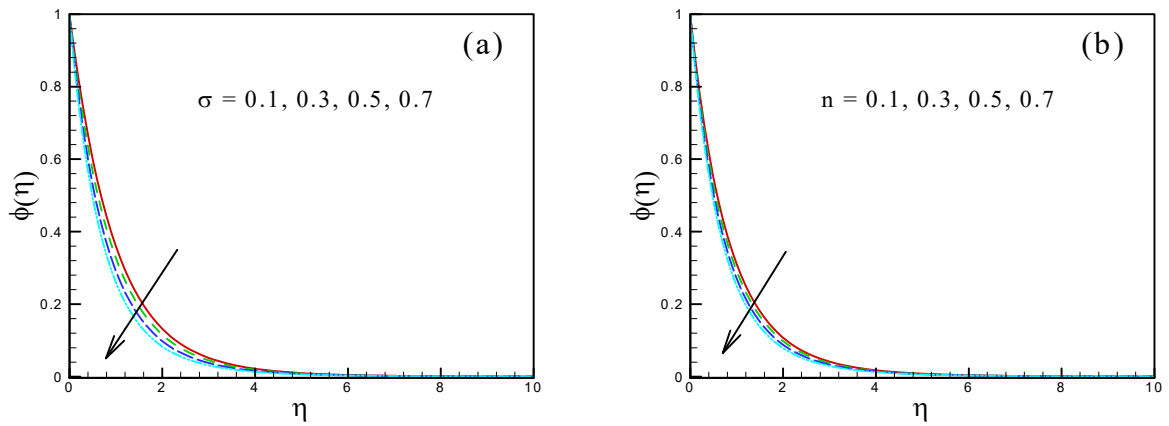


Fig. 4.8: Graph of $\phi(\eta)$ versus (a): σ and (b): n .

4.5 Numerical data of physical quantities

Tables 4.1 and **4.2** reveal the tendencies in thermal and solutal transport rates when the flow parameters are varied. **Table 4.1** exhibits that the heat transport grows as the radiation and temperature ratio parameter increases while it diminishes as the thermophoresis parameter and Brownian movement parameter boost. Also, via **Table 4.2** the numerical outcomes indicated that the solutal transport rate increases for the chemical reaction parameter, while the enhancing values of the thermophoresis, Brownian movement, and activation energy show a reverse pattern.

Table 4.1: The calculated values of $\text{Re}_z^{-1/2} Nu_z$ for R_d , θ_w , N_t , and N_b .

R_d	θ_w	N_t	N_b	$\text{Re}_z^{-1/2} Nu_z$
0.5	1.1	0.1	0.1	0.5285861
1.0	-	-	-	0.7354302
1.5	-	-	-	0.9822415
0.5	1.1	0.1	0.1	0.5285861
-	1.2	-	-	0.6724525
-	1.3	-	-	0.8125489
0.5	1.1	0.1	0.1	0.5285861
-	-	0.2	-	0.4807541
-	-	0.3	-	0.4356652
0.5	1.1	0.1	0.1	0.4174750
-	-	-	0.2	0.3603134
-	-	-	0.3	0.2300528

Table 4.2: The calculated values of $\text{Re}_z^{-1/2} Sh_z$ for σ , E , N_t , and N_b .

σ	E	N_t	N_b	$\text{Re}_z^{-1/2} Sh_z$
0.1	0.5	0.1	0.1	2.2608775
0.3	-	-	-	3.3716641
0.5	-	-	-	4.5112487
0.1	0.5	0.1	0.1	2.2608775
-	1.0	-	-	2.0406554
-	1.5	-	-	1.7725415
0.1	0.5	0.1	0.1	2.2608775
-	-	0.2	-	2.2675015
-	-	0.3	-	2.3041187
0.1	0.5	0.1	0.1	2.2608775
-	-	-	0.2	1.4005760
-	-	-	0.3	1.4515852

Chapter 5

Thermophoretic Particle Deposition with Soret-Dufour in a Flow of Fluid exhibit Relaxation/Retardation Times Effect

The goal of this chapter is to better understand how thermal energy is transported in time-dependent axisymmetric flow that is created by a stretchable cylinder with thermophoretic particle deposition and Soret-Dufour effects. Due to the thermal gradient the occurrence of diffusion of species and concentration gradient cause of heat flux which is one of the most fundamental mechanism for transportation of energy. In present study, the fluid flow reveals the relaxation and retardation phenomena. Moreover, the thermophoretic particles deposition is also considered in thermal analysis. The time-dependent partial differential equations for this flow dynamics are transformed into nonlinear ODEs and then solved

analytically through homotopy approach. The physical behavior of important parameters is studied in detail using graphical representations. The results show that as the values of the thermophoretic coefficient and thermophoretic parameter grow, the mass transfer rate declines. Further, the Soret and Dufour numbers are found to improve concentration and temperature distributions in the flow.

5.1 Physical problem description

Consider a viscoelastic fluid which accelerates due to the time-dependent stretchable cylinder. The well-known Oldroyd-B fluid model is used to study rheological features of relaxation/retardation phenomena. The cylinder orientation is taken as z -axis in axial direction and its surface stretching velocity is $u = u_w$. The flow field is supposed as (u, w) along (z, r) -axes. For the thermal analysis in the flow system we include the thermophoretic particles deposition effect. Additionally, it is assumed the thermal gradient and solutal gradient in the flow system produce the mass and heat flux, respectively.

For the time-dependent Oldroyd-B fluid, the governing equations of motion, thermal and solutal transport as well as the ultimate flow describing system are given below (cf. Chapter 2)

$$\frac{\partial (ru)}{\partial z} + \frac{\partial (rw)}{\partial r} = 0, \quad (5.1)$$

$$\left. \begin{aligned} & \frac{\partial u}{\partial t} + u \frac{\partial u}{\partial z} + w \frac{\partial u}{\partial r} + \lambda_1 \left\{ \frac{\partial^2 u}{\partial t^2} + u^2 \frac{\partial^2 u}{\partial z^2} + w^2 \frac{\partial^2 u}{\partial r^2} + 2u \frac{\partial^2 u}{\partial t \partial z} + 2w \frac{\partial^2 u}{\partial t \partial r} + 2uw \frac{\partial^2 u}{\partial r \partial z} \right\} \\ & = \nu \left(\frac{\partial^2 u}{\partial r^2} + \frac{1}{r} \frac{\partial u}{\partial r} \right) + \nu \lambda_2 \left\{ \begin{aligned} & \frac{\partial^3 u}{\partial t \partial r^2} + \frac{1}{r} \frac{\partial^2 u}{\partial t \partial r} + u \frac{\partial^3 u}{\partial z \partial r^2} + \frac{u}{r} \frac{\partial^2 u}{\partial z \partial r} + w \frac{\partial^3 u}{\partial r^3} \\ & + \frac{w}{r} \frac{\partial^2 u}{\partial r^2} + \frac{w}{r^2} \frac{\partial u}{\partial r} - \frac{\partial u}{\partial z} \frac{\partial^2 u}{\partial r^2} - \frac{1}{r} \frac{\partial u}{\partial z} \frac{\partial u}{\partial r} \\ & - 2 \frac{\partial u}{\partial r} \frac{\partial^2 w}{\partial r^2} - \frac{\partial u}{\partial r} \frac{\partial^2 u}{\partial z \partial r} - \frac{2}{r} \frac{\partial u}{\partial r} \frac{\partial w}{\partial r} \end{aligned} \right\} \end{aligned} \right\}, \quad (5.2)$$

$$\frac{\partial T}{\partial t} + u \frac{\partial T}{\partial z} + w \frac{\partial T}{\partial r} = \alpha_1 \frac{1}{r} \frac{\partial}{\partial r} \left(r \frac{\partial T}{\partial r} \right) + \frac{D_m^* k_T}{c_s c_p} \frac{1}{r} \frac{\partial}{\partial r} \left(r \frac{\partial C}{\partial r} \right), \quad (5.3)$$

$$\frac{\partial C}{\partial t} + u \frac{\partial C}{\partial z} + w \frac{\partial C}{\partial r} = D_B \frac{1}{r} \frac{\partial}{\partial r} \left(r \frac{\partial C}{\partial r} \right) + \frac{D_m^* k_T}{T_m} \frac{1}{r} \frac{\partial}{\partial r} \left(r \frac{\partial T}{\partial r} \right) - \frac{\partial}{\partial r} (V_t C), \quad (5.4)$$

with the relevant BC's are as follows

$$\left. \begin{aligned} u_w = \frac{az}{1-\alpha t}, \quad w = 0, \quad T = T_w, \quad C = C_w = 0 \text{ at } r = R, \\ u \rightarrow 0, \quad \frac{\partial u}{\partial r} \rightarrow 0, \quad T \rightarrow T_\infty \text{ and } C \rightarrow C_\infty \text{ as } r \rightarrow \infty \end{aligned} \right\}. \quad (5.5)$$

5.2 Thermophoretic particle deposition

The thermophoretic velocity associated with the boundary layer approximation was determined by Talbot *et al.* [80]. The additional effects of thermophoretic particle deposition are represented by the last term on R.H.S. of Eq. (5.4). The thermophoretic velocity V_t is defined by

$$V_t = -\frac{k^* \nu}{T} \frac{\partial T}{\partial r}, \quad (5.6)$$

where k^* is the thermophoretic coefficient, which varies between 0.2 and 1.2 according to Batchelor and Shen [81]. The term $k^* \nu$ denotes fluid thermophoretic diffusivity, and the term k^* is defined as [80]:

$$k^* = \frac{2c_s \left(\frac{\lambda_g}{\lambda_p} + C_t Kn \right) \left\{ 1 + Kn \left(C_1 + C_2 e^{-\frac{C_3}{Kn}} \right) \right\}}{(1 + 3C_m Kn) \left(1 + \frac{\lambda_g}{\lambda_p} + 2C_t Kn \right)}, \quad (5.7)$$

where the constants, $c_s = 1.147$, $C_m = 1.146$, $C_1 = 1.2$, $C_2 = 0.41$, $C_3 = 0.88$, $C_t = 2.20$, and λ_g and λ_p denote the heat conductivity's of fluid and diffused particles, respectively.

5.3 The problem solution

In the modelling, the following similarity variables are used [71, 82]:

$$\left. \begin{aligned} u &= \frac{az}{(1-\alpha t)} f'(\eta), \quad w = -\frac{R}{r} \sqrt{\frac{a\nu}{1-\alpha t}} f(\eta), \quad \eta = \sqrt{\frac{a}{\nu(1-\alpha t)}} \left(\frac{r^2 - R^2}{2R} \right), \\ \theta(\eta) &= \frac{T_\infty - T}{T_\infty - T_w}, \quad \phi(\eta) = \frac{C}{C_\infty} \end{aligned} \right\}. \quad (5.8)$$

The equations (5.2) to (5.4) take the following form

$$\left. \begin{aligned} & (1 + 2\eta k) f''' + 2k f'' + f f'' - f'^2 - S f' - \frac{1}{2} \eta S f'' - \frac{De_1 k}{(1+2\eta k)} f^2 f'' \\ +De_1 & \left\{ \begin{aligned} & 2f f' f'' - f^2 f''' - 2S f'^2 - \eta S f' f'' + 3S f f'' + \eta S f f''' - \frac{1}{4} \eta^2 S^2 f''' \\ & -\frac{7}{4} \eta S^2 f'' - 2S^2 f' \end{aligned} \right\} \\ +De_2 & \left\{ \begin{aligned} & (1 + 2\eta k) \{ f'^2 - f f^{iv} + \frac{1}{2} \eta S f^{iv} + 2S f''' \} \\ & -4k f f''' + 3S k f'' + \eta S k f''' \end{aligned} \right\} = 0 \end{aligned} \right\}, \quad (5.9)$$

$$(1 + 2\eta k) \theta'' + 2k \theta' + \text{Pr} f \theta' - \frac{1}{2} \text{Pr} \eta S \theta' + \text{Pr} D_f \{ (1 + 2\eta k) \phi'' + 2k \phi' \} = 0, \quad (5.10)$$

$$\left. \begin{aligned} & \frac{1}{S_c} \{ (1 + 2\eta k) \phi'' + 2k \phi' \} + f \phi' - \frac{1}{2} \eta S \phi' + S_r \{ (1 + 2\eta k) \theta'' + 2k \theta' \} \\ -\frac{k^* N_t^*}{1 - N_t^* \theta} & \left\{ \frac{(1 + 2\eta k) N_t^*}{1 - N_t^* \theta} \phi \theta'^2 + (1 + 2\eta k) \phi \theta'' + k \phi \theta' + (1 + 2\eta k) \theta' \phi' \right\} = 0 \end{aligned} \right\}, \quad (5.11)$$

with BCs as

$$\left. \begin{aligned} & f(0) = 0, \quad f'(0) = 1, \quad \theta(0) = 1, \quad \phi(0) = 0, \\ & f'(\infty) = 0, \quad f''(\infty) = 0, \quad \theta(\infty) = 0, \quad \phi(\infty) = 1 \end{aligned} \right\}. \quad (5.12)$$

The non-dimensional flow controlling parameters are: $k \left(= \frac{1}{R} \sqrt{\frac{\nu(1-\alpha t)}{a}} \right)$ is the curvature parameter, $De_1 \left(= \frac{\lambda_1 a}{1-\alpha t} \right)$ and $De_2 \left(= \frac{\lambda_2 a}{1-\alpha t} \right)$ the Deborah numbers, $S \left(= \frac{\alpha}{a} \right)$ the unsteadiness parameter, $D_f \left(= \frac{D_m^* k_T C_\infty}{c_s c_p \nu (T_w - T_\infty)} \right)$, $S_r \left(= \frac{D_m^* k_T (T_w - T_\infty)}{\nu T_m C_\infty} \right)$ the Dufour and Soret numbers, respec-

tively, N_t^* ($= \frac{T_w - T_\infty}{T_\infty}$) the thermophoretic parameter, Pr ($= \frac{\nu}{\alpha_1}$) the Prandtl and Sc ($= \frac{\nu}{D_B}$) the Schmidt number.

5.3.1 Solution technique

The following are taken as initial approximations and auxiliary linear operators:

$$f_o(\eta) = (1 - e^{-\eta}), \theta_o(\eta) = e^{-\eta} \text{ and } \phi_o(\eta) = e^{-\eta}, \quad (5.13)$$

$$\mathcal{L}_f = \frac{\partial^3}{\partial \eta^3} - \frac{\partial}{\partial \eta}, \mathcal{L}_\theta = \frac{\partial^2}{\partial \eta^2} - \theta \text{ and } \mathcal{L}_\phi = \frac{\partial^2}{\partial \eta^2} - \phi, \quad (5.14)$$

satisfying

$$\mathcal{L}_f = [c_0 + c_1 e^\eta + c_2 e^{-\eta}], \mathcal{L}_\theta = [c_3 e^\eta + c_4 e^{-\eta}] \text{ and } \mathcal{L}_\phi = [c_5 e^\eta + c_6 e^{-\eta}], \quad (5.15)$$

where c_i ($i = 0, 1, 2, \dots, 6$) are constants.

5.3.2 Convergence of solution

The convergence region is modified using the auxiliary parameters \hbar_f , \hbar_θ and \hbar_ϕ . For this purpose, we plotted and analyzed \hbar curves for the velocity, temperature, and concentration fields, as shown in **Fig. 5.1**. The range of adjusted values of \hbar_f , \hbar_θ and \hbar_ϕ are $-0.51 \leq \hbar_f \leq -0.01$, $-0.49 \leq \hbar_\theta \leq -0.14$, $-1.21 \leq \hbar_\phi \leq -0.14$, respectively.

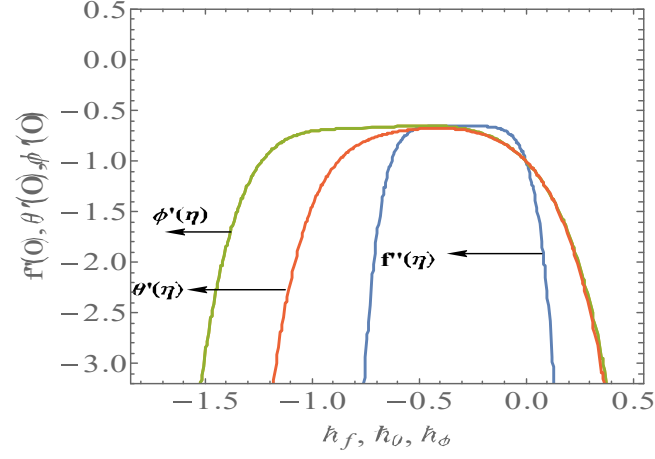


Fig. 5.1: The \hbar curves of $f''(0)$, $\theta'(0)$ and $\phi'(0)$.

5.4 Physical parameters

The heat transfer rate from the surface to the fluid can be calculated as

$$Nu_z = \frac{-\left(\frac{\partial T}{\partial r}\right)_{r=R}}{(T_w - T_\infty)/z} = -\text{Re}_z^{1/2} \theta'(0), \quad (5.16)$$

and the thermophoretic velocity at the cylinder's surface is

$$V_d = \frac{-D_B \left(\frac{\partial C}{\partial r}\right)_{r=R}}{C_\infty}. \quad (5.17)$$

The non-dimensional form can be written as

$$V_d^* = \frac{-\phi'(0)}{Sc}. \quad (5.18)$$

The non-dimensional Stanton number is

$$St_r \text{Re}^{\frac{1}{2}} = \frac{\phi'(0)}{Sc}, \quad (5.19)$$

with

$$V_d^* = -St_r \text{Re}^{\frac{1}{2}}. \quad (5.20)$$

5.5 Justification of graphical illustration

For the objective of this investigation, we considered the theoretical expression of the thermophoretic coefficient given by Talbot *et al.* [80]. To obtain ODEs, the set of PDEs that represents the defined stream pattern is converted using appropriate similarity transformations and boundary constraints. The outcomes of present flow problem are acquired analytically and presented in graphical attracts through **Fig. 5.2** to **5.9**, which show the motion of fluid, thermal, and solutal transport mechanisms. It's worth noting that each profile asymptotically meets the far field boundary conditions. Here, in this section a comprehensive discussion of these results is provided with physical justification. The dimensionless physical parameters are fixed in a range $0.0 \leq k \leq 1.0$, $0.0 \leq S \leq 1.5$, $0.1 \leq De_1 \leq 3.0$, $0.1 \leq De_2 \leq 3.0$, $0.1 \leq D_f \leq 0.7$, $0.1 \leq S_r \leq 1.2$, $0.01 \leq N_t^* \leq 0.6$, $1.0 \leq Sc \leq 1.4$ and $0.1 \leq k^* \leq 0.7$.

The outcome of the curvature parameter is displayed in **Fig. 5.2(a) to (c)**. The velocity profile increases as the curvature parameter is increased, as shown in **Fig. 5.2(a)**. Physically, in comparison with a larger radius of cylinder, the fluid velocity across the cylinder with a smaller radius is much faster. **Fig. 5.2(b)** illustrates the influence of the curvature parameter k on the thermal gradient. Since the curvature parameter is the ratio of boundary-layer thickness

to cylinder radius. The cylinder radius decreases dramatically as k increases. As a result of less resistance to liquid motion, the area of the cylinder in contact with the liquid decreases, resulting in an inclination of the thermal gradient. The variation of k on solutal curves is shown in **Fig. 5.2(c)**. Higher curvature values increases the radial velocity of the flow, which increases the concentration layer.

Fig. 5.3(a) to (c) shows the consequence of S on the flow field, fluid temperature, and fluid concentration distributions. An increase in S enhances the fluid velocity as seen in **Fig. 5.3(a)**. Physically, when the unsteadiness parameter is increased, the stretching rate decreases, which improves the boundary layer. The temperature and concentration distributions in the flow region are also improved, as noted in **Fig. 5.3(b) and (c)**. This is because motion is usually generated by stretching the surface, and the stretching surface velocity, temperature and concentrations are higher than the free stream velocity, temperature and concentration. It's also worth noting that in the absence of the unsteadiness parameter ($S = 0$), these plots increase smoothly, whereas they continuously accelerate as the unsteadiness parameter's value increases.

Fig. 5.4(a) and (b) portray the behavior of retardation time constant De_2 on fluid velocity and thermal distributions. When compared to the effects of the constant De_1 , the constant De_2 has the opposite effect on the velocity field, as seen in **Fig. 5.4(a)**. In reality, as the magnitude of viscous forces decreases, the velocity profile rises. As the elasticity increases for larger retardation time constants, the temperature profile shows a decreasing trend. This is because the Deborah number De_2 is directly proportional to the retardation time.

In **Fig. 5.5(a) and (b)**, it is noticed that the thermal distribution across the liquid layers heightened due to an increment in D_f . The thermal state receives enhancement due to the heat

generated by the temporary concentration gradient which is the constituent element of Dufour effect. The interesting phenomenon occurred in **Fig. 5.5(b)**, it shows the behavior of solutal profile with respect to Soret number S_r . An enlargement in Soret number S_r increases the concentration profiles. As a consequence, the solutal layer becomes thicker. The Soret effect is the mass transfer caused by a temperature gradient. The improvement in concentration profiles can be attributed to a higher Soret number.

Fig. 5.6(a) and (b) depict the influence of N_t^* and k^* on the concentration gradient. In **Fig. 5.6(a)**, it is noticed that with the increase N^* , the concentration gradient is reduced. Further, **Fig. 5.6(b)** shows that increasing the thermophoretic coefficient values degrade the concentration gradient. Particles discontinued in a fluid flow may move for a combination of reasons. This movement could be generated by Brownian diffusion, inertia, viscous drag, or different body forces. Suspended particles have a natural tendency to move from increased to lower thermal regions.

Fig. 5.7 depicts the encouragement of Sc as a function of concentration gradient. Physically, stronger viscous diffusion is associated with higher Sc values, resulting in an inclination of molecular motions.

Fig. 5.8 and **5.9** show the behavior of V_d^* for various values of the thermophoretic coefficient k^* and thermophoretic parameter N_t^* , respectively. **Fig. 5.8** depicts the influence of k^* on V_d^* versus thermophoretic parameter N_t^* . The plotted graph clearly shows that an increase in thermophoretic coefficient N_t^* values degrades V_d^* . Since the Stanton number is inversely proportionate to Sc , and the thermophoretic diffusion deposition velocity approaches zero asymptotically for larger Schmidt numbers. In this case, V_d^* is a decreasing function of the thermophoretic coefficient. **Fig. 5.9** depicts the variation in V_d^* versus k^* for various N_t^*

values. The rise in N_t^* values lowers the profile of V_d^* . In this case, V_d^* acts as a decreasing function of the thermophoretic coefficient.

Further, the values of $-\theta'(0)$ for De_2 , k and S are presented in **Table 5.1**. It is noted thermal transport descends for the increasing significances of fluid retardation time De_2 . Because increasing De_2 values increase retardation times. This increase causes a decrease in heat transport rate. Further, for increasing k , the rate of heat transport rises. Additionally, the S improved particle interactions, which improves thermal enhancement and led to rising numerical values for $-\theta'(0)$. **Table 5.2** is drawn to check the exactness of the analytical procedure.

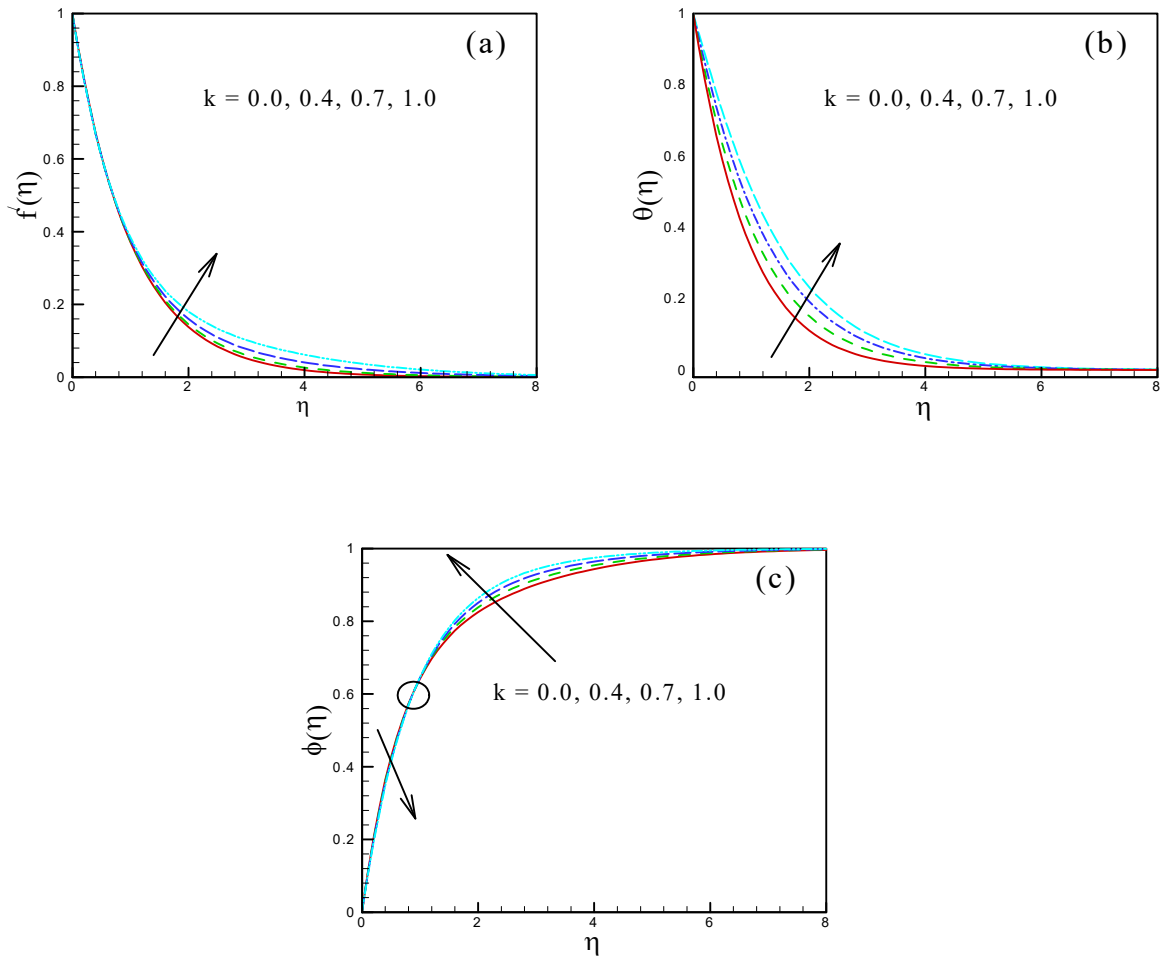


Fig. 5.2: Variation of k on $f'(\eta)$, $\theta(\eta)$ and $\phi(\eta)$.

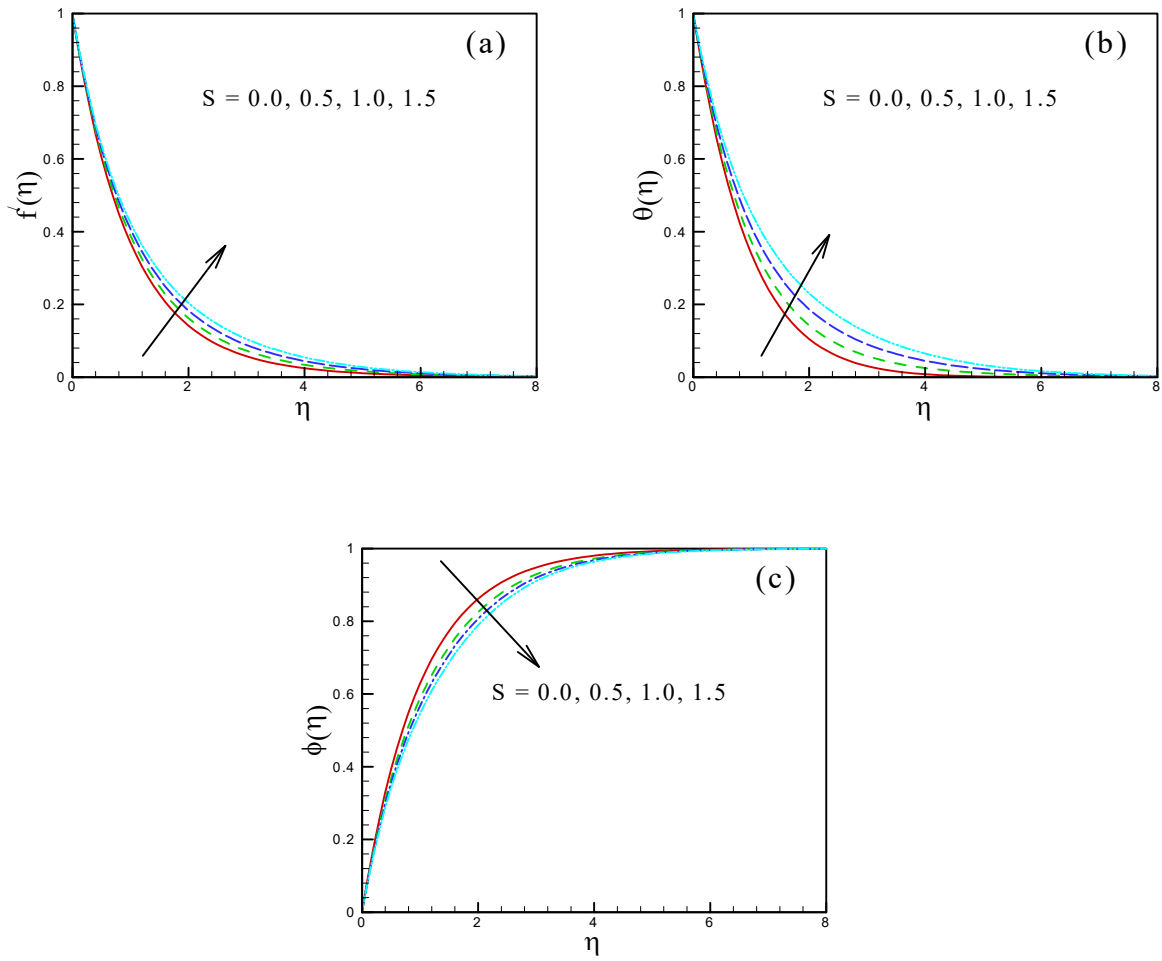


Fig. 5.3: Variation of S on $f'(\eta)$, $\theta(\eta)$ and $\phi(\eta)$.

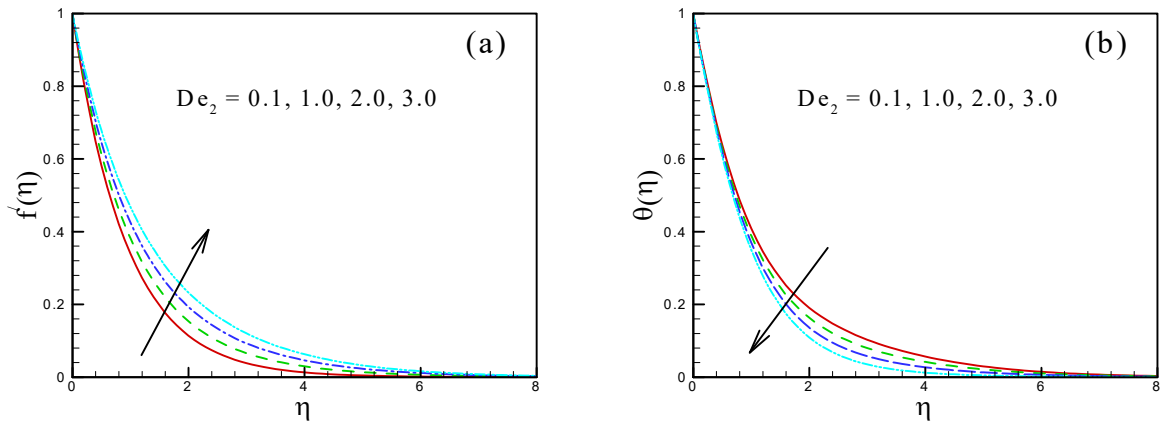


Fig. 5.4: Variation of De_2 on $f'(\eta)$ and $\theta(\eta)$.

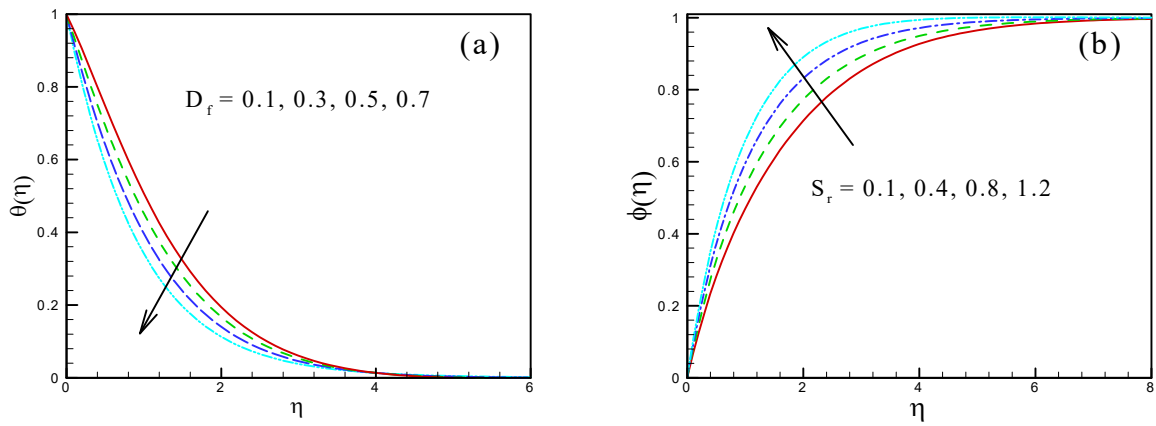


Fig. 5.5: Variation of D_f and S_r on $\theta(\eta)$ and $\phi(\eta)$, respectively.

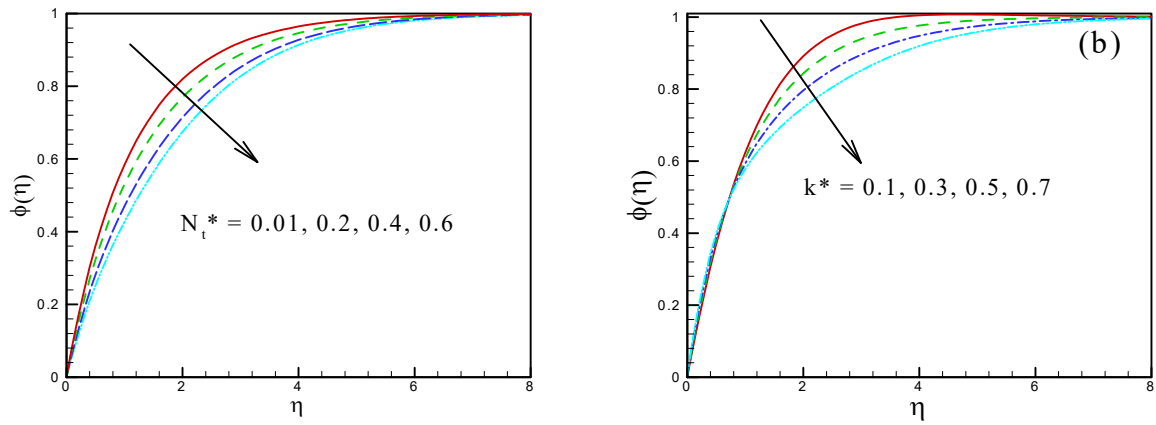


Fig. 5.6: Variation of N_t^* and k^* on $\phi(\eta)$.

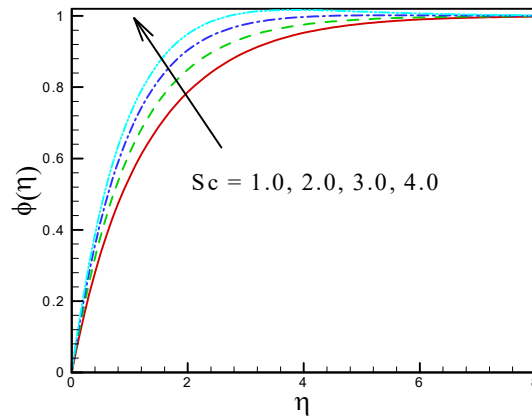


Fig. 5.7: Variation of Sc on $\phi(\eta)$.

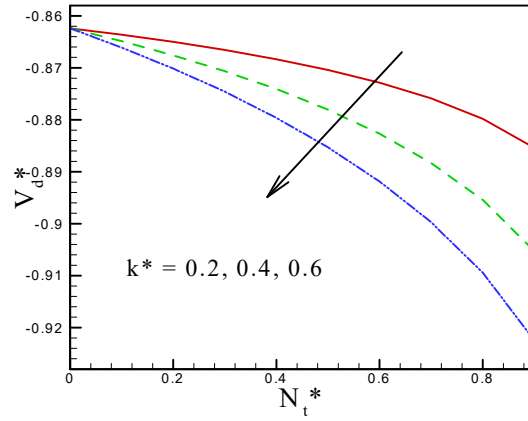


Fig. 5.8: Variation of k^* on V_d^* against N_t^* .

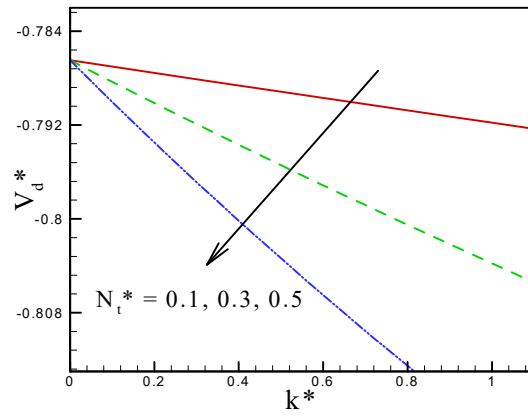


Fig. 5.9: Variation of N_t^* on V_d^* against k^* .

Table. 5.1: The numerical values of $-\theta'(0)$ for distant values of De_2 , k and S .

De_2	k	S	$-\theta'(0)$
0.1	0.1	0.1	0.6396972
0.2	-	-	0.6497337
0.3	-	-	0.6566886
0.4	-	-	0.6612412
0.1	0.1	0.1	0.6396972
-	0.3	-	0.6716092
-	0.5	-	0.7005311
-	0.7	-	0.7300124
0.1	0.1	0.1	0.6396972
-	-	0.2	0.7375931
-	-	0.3	0.8116354
-	-	0.4	0.9021548

Table. 5.2: The calculated numerical values of $-\theta'(0)$.

Pr	Ref. [77]	Ref. [78]	Current results
0.7	0.4539	0.453919	0.453753
2	0.9113	0.911156	0.911387

Chapter 6

Dynamics of Heat Transport in Flow of Non-linear Oldroyd-B Fluid subject to non-Fourier's Theory

The non-Fourier thermal transport in the stagnation point flow of a magnetized Oldroyd-B liquid due to stretching cylinder with the Cattaneo-Christov heat flux model is studied in this chapter. Further, as the controlling agents for thermal and solutal transport in the fluid flow, the heat/source phenomenon and chemical reaction are also considered. The formulations of a such physical phenomenon are going to form the PDEs. Through appropriate similarity variables, these governing PDEs for flow and energy transport are converted into the ODEs. The analytical series solutions are obtained through the use of homotopic approach. The graphical upshots are conducted for velocity field, temperature, and concentration distributions. In addition, energy transport analysis is performed for two kinds of surface heating mechanisms, namely the prescribed surface temperature and constant wall temperature. The

outcomes of the current investigation reveal that the thermal transportation rate is higher in the case of CWT as compared to the case of PST. Moreover, the increasing values of thermal and solutal relaxation time parameters reduce the heat and mass transport in the fluid flow, respectively.

6.1 Problem formulation

Let us assume the dynamics of Oldroyd-B material due to time-dependent cylindrical stretching surface in the stagnation point region. The elastic cylinder having radius R is stretched with velocity $u = u_w$. In a stretchable cylinder, the fluid flow is taken into account along the z -axis, and fluid deformation is taken into account along the radial r -direction. To study the thermal and solutal transport mechanisms in the flow of viscoelastic Oldroyd-B liquid, the Cattaneo-Christov heat theory is utilized. Further, heat generation/absorption has been incorporated for heat transport examination. And the mass balance equation illustrates the relationship between the chemical product and the concentration of liquid molecules. The velocity and magnetic fields are $[u, 0, w]$ and $[0, 0, B_o]$, respectively. The temperature of the fluid is studied for prescribed surface temperature and constant wall temperature, whereas, the concentration of the fluid is maintained at a constant wall, *i.e.*, $C = C_w$. In view of aforesaid assumptions, the model equations are (Eqs. (2.16 – 2.17) cf. chapter 2)

$$\frac{\partial (ru)}{\partial z} + \frac{\partial (rw)}{\partial r} = 0, \quad (6.1)$$

$$\left. \begin{aligned}
& \frac{\partial u}{\partial t} + u \frac{\partial u}{\partial z} + w \frac{\partial u}{\partial r} + \lambda_1 \left(\frac{\partial^2 u}{\partial t^2} + u^2 \frac{\partial^2 u}{\partial z^2} + w^2 \frac{\partial^2 u}{\partial r^2} + 2u \frac{\partial^2 u}{\partial t \partial z} + 2w \frac{\partial^2 u}{\partial t \partial r} + 2uw \frac{\partial^2 u}{\partial r \partial z} \right) \\
& = \frac{\nu}{r} \left(r \frac{\partial u}{\partial r} \right) + \nu \lambda_2 \left(\begin{aligned}
& \frac{\partial^3 u}{\partial t \partial r^2} + \frac{1}{r} \frac{\partial^2 u}{\partial t \partial r} + u \frac{\partial^3 u}{\partial r^2 \partial z} + \frac{w}{r} \frac{\partial^2 u}{\partial r^2} + \frac{u}{r} \frac{\partial^2 u}{\partial z \partial r} + w \frac{\partial^3 u}{\partial r^3} + \frac{w}{r^2} \frac{\partial u}{\partial r} \\
& - \frac{\partial u}{\partial z} \frac{\partial^2 u}{\partial r^2} - \frac{1}{r} \frac{\partial u}{\partial z} \frac{\partial u}{\partial r} - \frac{\partial u}{\partial r} \frac{\partial^2 u}{\partial r \partial z} - \frac{2}{r} \frac{\partial w}{\partial r} \frac{\partial u}{\partial r} - 2 \frac{\partial u}{\partial r} \frac{\partial^2 w}{\partial r^2} \\
& - \frac{\sigma B_0^2}{\rho_f} \left(u + \lambda_1 \left\{ \frac{\partial u}{\partial t} + w \frac{\partial u}{\partial r} \right\} \right),
\end{aligned} \right) \quad (6.2)
\end{aligned} \right\}$$

By keeping in mind the assumptions stated above, utilizing the conservation laws (1.6, 1.12)

and (1.8, 1.13), the energy and concentration equations are

$$\left. \begin{aligned}
& \frac{\partial T}{\partial t} + u \frac{\partial T}{\partial z} + w \frac{\partial T}{\partial r} + \lambda_t \left[\begin{aligned}
& \frac{\partial^2 T}{\partial t^2} + \frac{\partial u}{\partial t} \frac{\partial T}{\partial z} + 2u \frac{\partial^2 T}{\partial t \partial z} + \frac{\partial w}{\partial t} \frac{\partial T}{\partial r} + 2w \frac{\partial^2 T}{\partial t \partial r} \\
& + 2uw \frac{\partial^2 T}{\partial r \partial z} + w^2 \frac{\partial^2 T}{\partial r^2} + u^2 \frac{\partial^2 T}{\partial z^2} + u \frac{\partial u}{\partial z} \frac{\partial T}{\partial z} \\
& + w \frac{\partial u}{\partial r} \frac{\partial T}{\partial z} + u \frac{\partial w}{\partial z} \frac{\partial T}{\partial r} + w \frac{\partial w}{\partial r} \frac{\partial T}{\partial r}
\end{aligned} \right] \quad (6.3) \\
& = \frac{\alpha_1}{r} \frac{\partial}{\partial r} \left(r \frac{\partial T}{\partial r} \right) + \frac{Q_o}{(\rho c_p)_f} (T - T_\infty) + \frac{Q_o}{(\rho c_p)_f} \lambda_t \left(\frac{\partial T}{\partial t} + u \frac{\partial T}{\partial z} + w \frac{\partial T}{\partial r} \right)
\end{aligned} \right\}$$

$$\left. \begin{aligned}
& \frac{\partial C}{\partial t} + u \frac{\partial C}{\partial z} + w \frac{\partial C}{\partial r} + \lambda_c \left[\begin{aligned}
& \frac{\partial^2 C}{\partial t^2} + \frac{\partial u}{\partial t} \frac{\partial C}{\partial z} + 2u \frac{\partial^2 C}{\partial t \partial z} + \frac{\partial w}{\partial t} \frac{\partial C}{\partial r} + 2w \frac{\partial^2 C}{\partial t \partial r} \\
& + 2uw \frac{\partial^2 C}{\partial r \partial z} + w^2 \frac{\partial^2 C}{\partial r^2} + u^2 \frac{\partial^2 C}{\partial z^2} + u \frac{\partial u}{\partial z} \frac{\partial C}{\partial z} \\
& + w \frac{\partial u}{\partial r} \frac{\partial C}{\partial z} + u \frac{\partial w}{\partial z} \frac{\partial C}{\partial r} + w \frac{\partial w}{\partial r} \frac{\partial C}{\partial r}
\end{aligned} \right] \quad (6.4) \\
& = \frac{D_B}{r} \frac{\partial}{\partial r} \left(r \frac{\partial C}{\partial r} \right) - k_c (C - C_\infty) - k_c \lambda_c \left(\frac{\partial C}{\partial t} + u \frac{\partial C}{\partial z} + w \frac{\partial C}{\partial r} \right)
\end{aligned} \right\}$$

with the boundary condition for the system

$$\left. \begin{aligned}
& u_w = \frac{az}{(1-\alpha t)}, \quad w = 0, \\
& T = T_w \text{ (CWT)}, \quad T = T_\infty + \frac{bz}{(1-\alpha t)} \text{ (PST)}, \quad \text{and } C = C_w \text{ at } r = R, \\
& u \rightarrow u_e = \frac{cz}{(1-\alpha t)}, \quad \frac{\partial u}{\partial r} \rightarrow 0, \quad T \rightarrow T_\infty \text{ and } C \rightarrow C_\infty \text{ as } r \rightarrow \infty
\end{aligned} \right\} \quad (6.5)$$

Letting [83]:

$$\left. \begin{aligned} u &= \frac{az}{(1-\alpha t)} f'(\eta), \quad w = -\frac{R}{r} \sqrt{\frac{av}{1-\alpha t}} f(\eta), \\ T &= T_\infty + (T_w - T_\infty) \theta(\eta) \quad (\text{CWT}), \quad T = T_\infty + \frac{bz}{(1-\alpha t)} \theta(\eta) \quad (\text{PST}), \\ C &= C_\infty + (C_w - C_\infty) \phi(\eta), \quad \eta = \sqrt{\frac{a}{\nu(1-\alpha t)}} \left(\frac{r^2 - R^2}{2R} \right) \end{aligned} \right\}, \quad (6.6)$$

to transform the PDE's into dimensionless form as

$$\left. \begin{aligned} &(1 + 2\eta k) f''' + 2k f'' + f f'' - f'^2 - S f' - \frac{1}{2} \eta S f'' - \frac{De_1 k}{(1+2\eta k)} f^2 f'' \\ + De_1 &\left(\begin{aligned} &2f f' f'' - f^2 f''' - 2S f'^2 - \eta S f' f'' + 3S f f'' + \eta S f f''' - \frac{1}{4} \eta^2 S^2 f''' \\ &-\frac{7}{4} \eta S^2 f'' - 2S^2 f' + 2(A^2 S + AS^2) \end{aligned} \right) \\ + De_2 &[(1 + 2\eta k) \{f''^2 - f f^{iv} + \frac{1}{2} \eta S f^{iv} + 2S f'''\} - 4k f f''' + 3S k f'' + \eta S k f'''] \\ &-M (f' + \frac{1}{2} S De_1 f'' - AS De_1 + De_1 S f' - De_1 f f'' + A) + AS + A^2 = 0, \end{aligned} \right\}, \quad (6.7)$$

$$\left. \begin{aligned} &(1 + 2\alpha \eta) \theta'' + 2\alpha \theta' + \text{Pr} (1 - \beta_t \delta) f \theta' - \frac{1}{2} \text{Pr} \eta S \theta' (1 - \beta_t \delta) + \text{Pr} \delta \theta \\ - \text{Pr} \beta_t &\left(\frac{3}{4} \eta S^2 \theta' - \frac{3}{2} S f \theta' - \frac{1}{2} \eta S f' \theta' + \frac{1}{4} \eta^2 S^2 \theta'' - \eta S f \theta'' + f^2 \theta'' - f f' \theta' \right) = 0 \end{aligned} \right\}, \quad (6.8)$$

$$\left. \begin{aligned} &(1 + 2\eta k) \theta'' + 2k \theta' + \text{Pr} (1 - \beta_t \delta^*) f \theta' - \frac{1}{2} \text{Pr} \eta S \theta' (1 - \beta_t \delta^*) \\ &- \text{Pr} (1 - \beta_t \delta^*) f' \theta - \text{Pr} S \theta (1 - \beta_t \delta^*) + \text{Pr} \delta^* \theta \\ - \text{Pr} \beta_t &\left(\frac{3}{4} \eta S^2 \theta' - \frac{3}{2} S f \theta' - \frac{1}{2} \eta S f' \theta' + \frac{1}{4} \eta^2 S^2 \theta'' - \eta S f \theta'' + f^2 \theta'' - f f' \theta' \right) = 0 \end{aligned} \right\}, \quad (6.9)$$

$$\left. \begin{aligned} &(1 + 2\eta k) \phi'' + 2k \phi' + Sc (1 - \beta_c C_r) f \phi' - \frac{1}{2} \eta S Sc \phi' (1 - \beta_c C_r) - C_r Sc \phi \\ - Sc \beta_c &\left(\frac{3}{4} \eta S^2 \phi' - \frac{3}{2} S f \phi' - \frac{1}{2} \eta S f' \phi' + \frac{1}{4} \eta^2 S^2 \phi'' - \eta S f \phi'' + f^2 \phi'' - f f' \phi' \right) = 0 \end{aligned} \right\}, \quad (6.10)$$

the related BC's are

$$\left. \begin{aligned} f(0) = 0, f'(0) = 1, \theta(0) = 1, \phi(0) = 1, \\ f'(\infty) = A, f''(\infty) = 0, \theta(\infty) = 0, \phi(\infty) = 0 \end{aligned} \right\}. \quad (6.11)$$

According to the equations above, the dimensionless parameters are

$$\left. \begin{aligned} De_1 = \frac{\lambda_1 a}{1-\alpha t}, De_2 = \frac{\lambda_2 a}{1-\alpha t}, M = \sqrt{\frac{\sigma B_o^2(1-\alpha t)}{a\rho_f}}, k = \frac{1}{R} \sqrt{\frac{\nu(1-\alpha t)}{a}}, Pr = \frac{\nu}{\alpha_1}, \\ S = \frac{\alpha}{a}, \delta^* = \frac{Q_o(1-\alpha t)}{a(\rho_{cp})_f}, Sc = \frac{\nu}{D_B}, \beta_t = \frac{\lambda_f a}{1-\alpha t}, C_r = \frac{k_c(1-\alpha t)}{a}, \beta_c = \frac{\lambda_c a}{1-\alpha t} \end{aligned} \right\}, \quad (6.12)$$

and these relations are, respectively, termed as the fluid relaxation time, fluid retardation time, magnetic field parameter, curvature parameter, Prandtl number, unsteadiness parameter, heat generation/absorption parameter, Schmidt number, thermal relaxation time, chemical reaction parameter, solutal relaxation time. (cf. chapter 3).

6.2 Solutions expressions

To obtain the most accurate approximations of our problem, we can choose the base functions and linear operators with great freedom using the homotopy analysis approach. With this flexibility, we are able to solve the problem that is extremely nonlinear and get results that are satisfactory. The linear operators for the homotopy analysis procedure are selected from the differential equation's linear section. The options for auxiliary linear operators and initial approximations are as follows:

$$f_o(\eta) = (1 - e^{-\eta}), \theta_o(\eta) = e^{-\eta} \text{ and } \phi_o(\eta) = e^{-\eta}, \quad (6.13)$$

$$\mathcal{L}_f = \frac{\partial^3}{\partial \eta^3} - \frac{\partial}{\partial \eta}, \quad \mathcal{L}_\theta = \frac{\partial^2}{\partial \eta^2} - \theta \quad \text{and} \quad \mathcal{L}_\phi = \frac{\partial^2}{\partial \eta^2} - \phi, \quad (6.14)$$

satisfying

$$\mathcal{L}_f = [c_0 + c_1 e^\eta + c_2 e^{-\eta}], \quad \mathcal{L}_\theta = [c_3 e^\eta + c_4 e^{-\eta}] \quad \text{and} \quad \mathcal{L}_\phi = [c_5 e^\eta + c_6 e^{-\eta}], \quad (6.15)$$

where c_i ($i = 0, 1, 2, \dots, 6$) are arbitrary constants.

The general solutions can be expressed as

$$\left. \begin{aligned} f_m(\eta) &= f_m^*(\eta) + c_0 + c_1 e^\eta + c_2 e^{-\eta} \\ \theta_m(\eta) &= \theta_m^*(\eta) + c_3 e^\eta + c_4 e^{-\eta} \\ \phi_m(\eta) &= \phi_m^*(\eta) + c_5 e^\eta + c_6 e^{-\eta} \end{aligned} \right\}, \quad (6.16)$$

where $f_m^*(\eta)$, $\theta_m^*(\eta)$ and $\phi_m^*(\eta)$ indicate the special solutions.

6.3 Convergence analysis

It's interesting to note that the analytic series solutions for velocity, temperature, and concentration distributions contain convergence control parameters \hbar_f , \hbar_θ , and \hbar_ϕ giving us the freedom to regulate both the convergence region and rate. **Table 6.1** is delivered to guarantee the convergence of the outcomes.

Table. 6.1: The convergence of the outcomes when $k = S = M = 0.1$, $\beta_e = \beta_c = \delta^* = C_r = 0.1$, $De_1 = De_2 = 0.5$, $Pr = 6.2$ and $Sc = 1$.

Approximation order	$-f''(0)$	$-\theta'(0)$	$-\phi'(0)$
1	1.024354	0.735323	0.336524
5	1.052654	0.754376	0.345253
10	1.192456	0.765243	0.348427
15	1.216354	0.779355	0.349231
20	1.226364	0.780253	0.354322
25	1.226543	0.781743	0.352354
30	1.226543	0.781751	0.352354
35	1.226543	0.781751	0.352354
40	1.226543	0.781751	0.352354

6.4 Discussion of results

For the velocity, thermal, and solutal fields of unsteady Oldroyd-B fluid flow, the graphical results are displayed in this section. The temperature distribution is plotted for both CWT and PST wall heating agents. In the comparison of CWT and PST, it is noted that CWT has a higher rate of heat transfer in the fluid flow. To compute an infinite series solution, a semi-analytical scheme, i.e. the HAM in Mathematica, is used. In the computation methodology of the results, the values of pertinent parameters are fixed as: the curvature k ($0.0 \leq k \leq 0.7$), velocity ratio parameter A ($0.0 \leq A \leq 0.5$), fluid retardation time De_2 ($0.0 \leq De_2 \leq 0.5$), mag-

netic field M ($0.1 \leq M \leq 1.5$), thermal relaxation time β_t ($0.1 \leq \beta_t \leq 0.5$), heat source/sink δ^* ($-0.1 \leq \delta^* \leq 0.3$), solutal relaxation time β_c ($0.1 \leq \beta_c \leq 0.7$), and chemical reaction parameter C_r ($0.1 \leq C_r \leq 0.7$).

Fig. 6.1(a) displays how the curvature parameter affects the fluid velocity. From here, it is concluded that a higher value of the curvature parameter raises the fluid velocity away from a cylinder's surface. Physically, for the increasing values of k , the radius of the cylinder lowers; as a result, the consistency of the momentum boundary layer decreases because the influence of the boundary on the fluid flow is reduced, which increases the fluid flow velocity. The consequences of retardation time effects on dimensionless fluid velocity is displayed in **Fig. 6.1(b)**. As we know De_2 is directly proportional to the retardation time. Thus, an increase in De_2 enhances the fluid velocity. In fact, elastic forces decline due to addition in retardation time and therefore, the velocity profile improves. On the other hand, boosting De_2 lowers the temperature and concentration. Because the elasticity increases with increasing retardation time De_2 , therefore, the temperature and concentration profiles for De_2 decrease.

Fig. 6.2(a) and **(b)** shows that increasing velocity ratio parameter A , causes the velocity field to increase, while decreasing the temperature of the fluid. As $A (< 1)$ means that the stretching surface velocity is greater than the free stream velocity, the converse is true for $A (> 1)$. Therefore, for the case where $A (< 1)$, the fluid velocity raises as A boosts up because the higher stretching velocity increases the fluid motion. In contrast, as A increases, the temperature distribution decreases. Physically, the forced convection phenomenon is the primary mechanism for the transfer of thermal energy in fluid. As a result, the forced convection is reduced for higher values of A . Therefore, in this case, the temperature field falls.

Fig. 6.3(a) and **(b)** depict that as the magnetic parameter M increases, the velocity of the

fluid decreases, and the temperature field increases. Physically, the Lorentz force produced by the normally applied magnetic field to the fluid flow velocity causes resistance to the fluid motion in the boundary layer, which causes the velocity field to decelerate. Additionally, the Lorentz force, which improves the interaction of the fluid particles, increases the fluid's conduction in the case of the transportation of thermal energy.

To depict the outcome of dimensionless relaxation time parameter β_t on the temperature field **Fig. 6.4(a)** is delineated. It is observed that the fluid temperature declines with boosting values of β_t . Physically, in the non-heat Fourier's flux model the dimensionless relaxation time parameter, β_t , is the controlling constraint for the propagation of thermal waves in the fluid. Thus, an increment in β_t reduces the thermal transportation in the fluid. **Fig. 6.4(b)** shows how the temperature profile is affected by the internal heat generation/absorption parameter δ^* . It is observed that the presence of a heat source in the system causes the temperature distribution to rise, whereas the presence of a heat sink causes the temperature distribution to diminish. From the physical sense of view, we can deduce that the fact of a heat source/sink in the system recreates a necessary role in terms of maintaining the temperature of the fluid.

The effect of the solutal relaxation time β_c on the concentration field is depicted in **Fig. 6.5(a)**. A larger β_c indicates that the liquid concentration profile decays while the thickness of the solutal layer increases. This is because of the direct relationship between β_c and λ_c , which causes the thickness of the solutal layer to increase as β_c increases. The implications of reaction rate on the concentration field are represented through **Fig. 6.5(b)**. It is observed that, when C_r increases, the thickness of the solutal layer increases while the concentration field decreases. This is due to the fact that chemical reaction variables are directly related to reaction rates.

The comparative analysis of the results with previously published literature is presented in

Table 6.2. In a limiting case, it should be noted that the current results are in good agreement with the results that have been published.

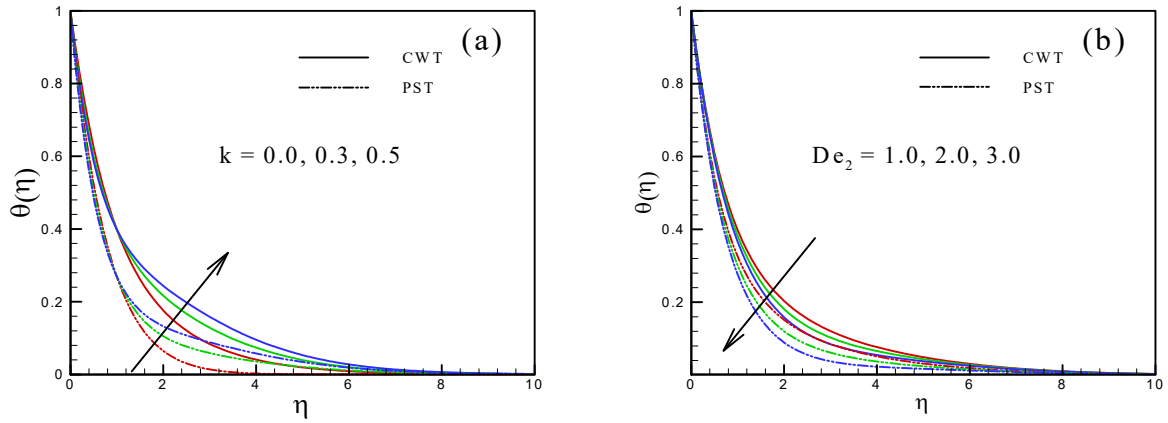


Fig. 6.1: Impact of k and De_2 on $\theta(\eta)$.

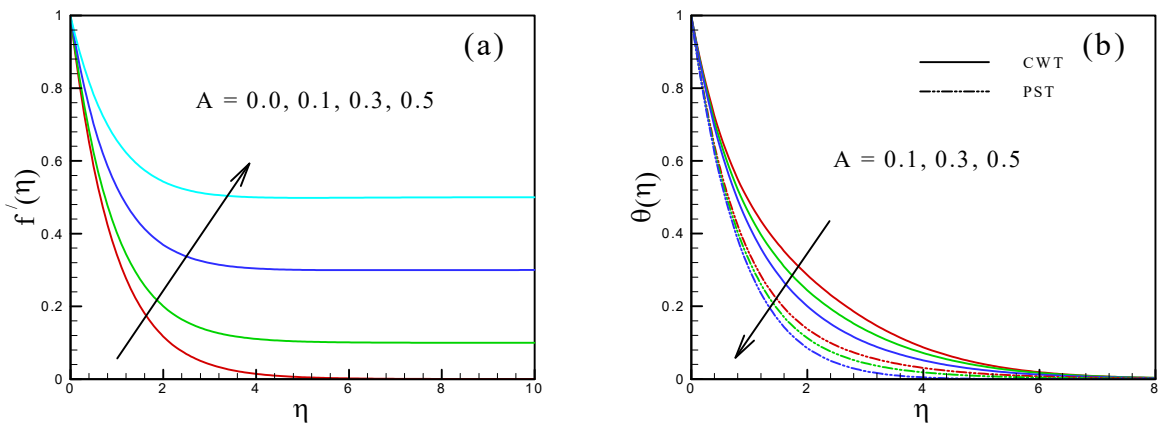


Fig. 6.2: Impact of A on $f'(\eta)$ and $\theta(\eta)$.

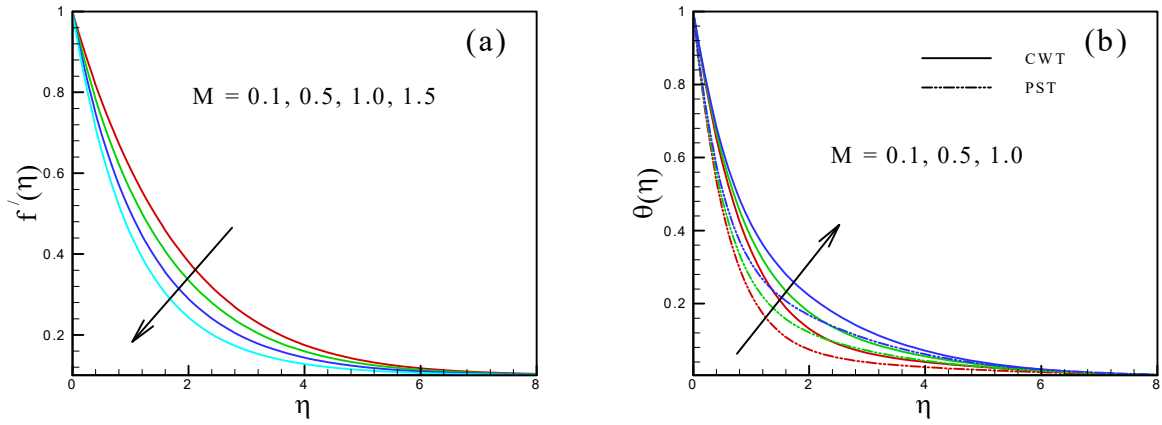


Fig. 6.3: Impact of M on $f'(\eta)$ and $\theta(\eta)$.

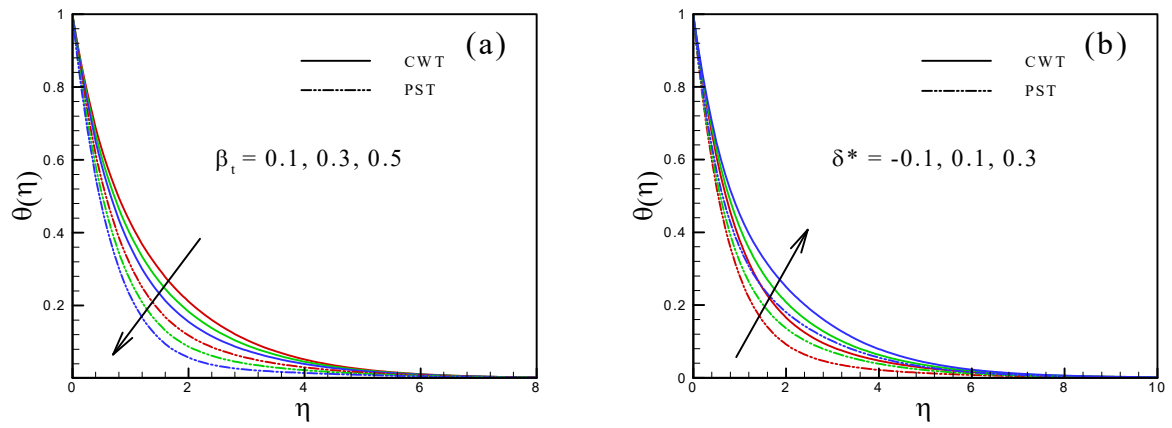


Fig. 6.4: Impact of β_t and δ on $\theta(\eta)$.

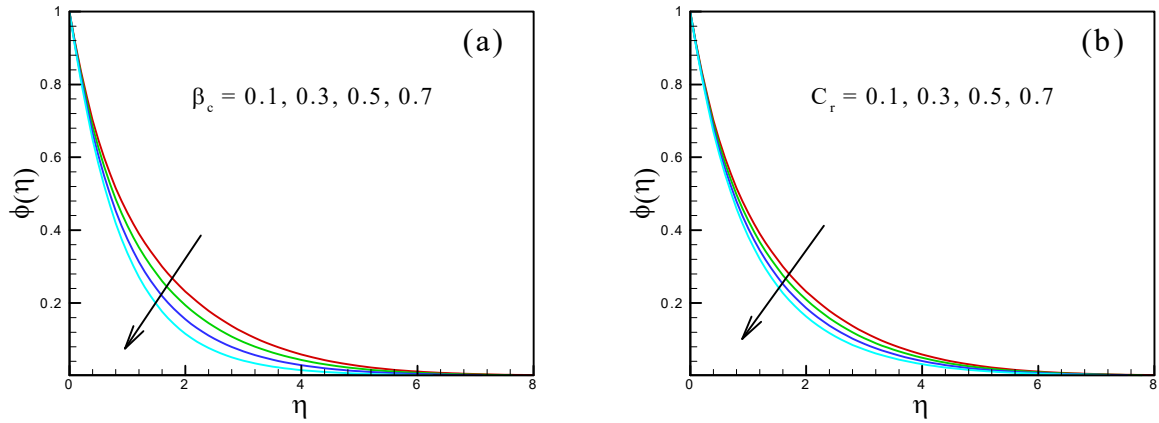


Fig. 6.5: Impact of β_c and C_r on $\phi(\eta)$.

Table. 6.2: Comparison of $f''(0)$ for De_2 when $k = S = M = 0$ when $De_1 = 0.4$.

De_2	Abbasi <i>et al.</i> [84]	Current results
0.2	1.00498	1.004324
0.4	0.92986	0.925478
0.6	0.86942	0.868511
0.8	0.81943	0.819214
1.0	0.77718	0.778112

Chapter 7

Axisymmetric of Oldroyd-B Material with Homogeneous-Heterogeneous Reactions subject to Cattaneo-Christov Heat Transfer

The aim of current chapter is to investigate the characteristics of homogeneous-heterogeneous reactions in the axisymmetric flow of Oldroyd-B material using heat conduction analysis. The heat transfer phenomenon is examined from the non-Fourier heat flux model perspective. The governing flow field equations are developed using the rheological formulation of the Oldroyd-B fluid model, which turned into a set of ODEs by utilizing the proper similarity conversions. The upshots for the velocity, thermal, and solutal distributions are derived. The physical behaviors of relevant parameters are discussed in detail. The findings reveal that for the curvature parameter, the fluid velocity improves nearby the cylinder surface

and no motion occurs away from the surface, while this predicts the dual behavior on temperature and concentration distributions. Further, fluid relaxation and retardation time exhibit opposite behaviors on fluid velocity. Additionally, the results demonstrate that the homogeneous response parameter exhibits contradicting behavior on the concentration field while the thermal relaxation parameter lowers the temperature field.

7.1 Mathematical formulation

A horizontal stretched cylinder having radius R is taken into account for the unsteady flow of an Oldroyd-B fluid. The cylinder surface is physically stretched with a velocity $u = u_w$. Further, the heat transfer rate is investigated employing the Cattaneo-Christov theory, which describes the property of thermal relaxation. Furthermore, the consequences of the catalyst's reactions are also taken into consideration. The controlling flow equations under these presumptions are as follow, (cf. Chapter 6 and Eq. (1.14))

$$\frac{\partial(ru)}{\partial z} + \frac{\partial(rw)}{\partial r} = 0, \quad (7.1)$$

$$\left. \begin{aligned} & \frac{\partial u}{\partial t} + u \frac{\partial u}{\partial z} + w \frac{\partial u}{\partial r} + \lambda_1 \left\{ \frac{\partial^2 u}{\partial t^2} + u^2 \frac{\partial^2 u}{\partial z^2} + w^2 \frac{\partial^2 u}{\partial r^2} + 2u \frac{\partial^2 u}{\partial t \partial z} + 2w \frac{\partial^2 u}{\partial t \partial r} + 2uw \frac{\partial^2 u}{\partial r \partial z} \right\} \\ & = \nu \left(\frac{\partial^2 u}{\partial r^2} + \frac{1}{r} \frac{\partial u}{\partial r} \right) + \nu \lambda_2 \left\{ \begin{aligned} & \frac{\partial^3 u}{\partial t \partial r^2} + \frac{1}{r} \frac{\partial^2 u}{\partial t \partial r} + u \frac{\partial^3 u}{\partial z \partial r^2} \\ & + \frac{u}{r} \frac{\partial^2 u}{\partial z \partial r} + w \frac{\partial^3 u}{\partial r^3} + \frac{w}{r} \frac{\partial^2 u}{\partial r^2} + \frac{w}{r^2} \frac{\partial u}{\partial r} \end{aligned} \right\} \\ & - \nu \lambda_2 \left\{ \frac{\partial u}{\partial z} \frac{\partial^2 u}{\partial r^2} + \frac{1}{r} \frac{\partial u}{\partial z} \frac{\partial u}{\partial r} + 2 \frac{\partial u}{\partial r} \frac{\partial^2 w}{\partial r^2} + \frac{\partial u}{\partial r} \frac{\partial^2 u}{\partial z \partial r} + \frac{2}{r} \frac{\partial u}{\partial r} \frac{\partial w}{\partial r} \right\} \end{aligned} \right\}, \quad (7.2)$$

$$\frac{\partial T}{\partial t} + u \frac{\partial T}{\partial z} + w \frac{\partial T}{\partial r} + \lambda_t \left\{ \begin{array}{l} \frac{\partial^2 T}{\partial t^2} + \frac{\partial u}{\partial t} \frac{\partial T}{\partial z} + 2u \frac{\partial^2 T}{\partial t \partial z} + \frac{\partial w}{\partial t} \frac{\partial T}{\partial r} + 2w \frac{\partial^2 T}{\partial t \partial r} \\ + 2uw \frac{\partial^2 T}{\partial r \partial z} + w^2 \frac{\partial^2 T}{\partial r^2} + u^2 \frac{\partial^2 T}{\partial z^2} + u \frac{\partial u}{\partial z} \frac{\partial T}{\partial z} \\ + w \frac{\partial u}{\partial r} \frac{\partial T}{\partial z} + u \frac{\partial w}{\partial z} \frac{\partial T}{\partial r} + w \frac{\partial w}{\partial r} \frac{\partial T}{\partial r} \end{array} \right\} = \frac{\alpha_1}{r} \frac{\partial}{\partial r} \left(r \frac{\partial T}{\partial r} \right), \quad (7.3)$$

$$\frac{\partial a^*}{\partial t} + u \frac{\partial a^*}{\partial z} + w \frac{\partial a^*}{\partial r} = D_{A^*} \left(\frac{1}{r} \frac{\partial a^*}{\partial r} + \frac{\partial^2 a^*}{\partial r^2} \right) - k_c a^* b^{*2}, \quad (7.4)$$

$$\frac{\partial b^*}{\partial t} + u \frac{\partial b^*}{\partial z} + w \frac{\partial b^*}{\partial r} = D_{B^*} \left(\frac{1}{r} \frac{\partial b^*}{\partial r} + \frac{\partial^2 b^*}{\partial r^2} \right) + k_c a^* b^{*2}, \quad (7.5)$$

with BC's

$$\left. \begin{array}{l} u = u_w = \frac{az}{1-\alpha t}, \quad w = 0, \quad T = T_w, \\ D_{A^*} \frac{\partial a^*}{\partial r} = k_s a^*, \quad D_{B^*} \frac{\partial b^*}{\partial r} = -k_s a^* \\ u \rightarrow 0, \quad \frac{\partial u}{\partial r} \rightarrow 0, \quad T \rightarrow T_\infty, \quad a^* \rightarrow a_o, \quad b^* \rightarrow 0 \text{ as } r \rightarrow \infty \end{array} \right\} \text{ at } r = R, \quad (7.6)$$

where a is the stretching rate and a_o the positive constant.

Letting [85]:

$$\left. \begin{array}{l} u = \frac{az}{(1-\alpha t)} f'(\eta), \quad w = -\frac{R}{r} \sqrt{\frac{a\nu}{1-\alpha t}} f(\eta), \quad \theta = \frac{T-T_\infty}{T_w-T_\infty}, \\ a^* = a_o g(\eta), \quad b^* = a_o h(\eta), \quad \eta = \sqrt{\frac{a}{\nu(1-\alpha t)}} \left(\frac{r^2 - R^2}{2R} \right) \end{array} \right\}, \quad (7.7)$$

which convert the PDEs as

$$\left. \begin{array}{l} (1 + 2\eta k) f''' + 2k f'' + f f'' - f'^2 - S f' - \frac{1}{2} \eta S f'' - \frac{De_1 k}{(1+2\eta k)} f^2 f'' \\ + De_1 \left\{ \begin{array}{l} 2f f' f'' - 2S f'^2 - 2S^2 f' - \eta S f' f'' + 3S f f'' - f^2 f''' \\ + \eta S f f''' - \frac{7}{4} \eta S^2 f'' - \frac{1}{4} \eta^2 S^2 f''' \end{array} \right\} \\ + De_2 \left\{ \begin{array}{l} (1 + 2\eta k) \{ f''^2 + 2S f''' + \frac{1}{2} \eta S f^{iv} - f f^{iv} \} + 3S k f'' \\ + \eta S k f''' - 4k f f''' \end{array} \right\} = 0 \end{array} \right\}, \quad (7.8)$$

$$\left. \begin{aligned} & (1 + 2\eta k)\theta'' + 2k\theta' + \text{Pr} f\theta' - \frac{1}{2}\text{Pr}\eta S\theta' \\ & - \text{Pr}\beta_t \left(\frac{3}{4}\eta S^2\theta' - \frac{3}{2}Sf\theta' - \frac{1}{2}\eta Sf'\theta' + \frac{1}{4}\eta^2 S^2\theta'' - \eta Sf\theta'' + f^2\theta'' + ff'\theta' \right) = 0 \end{aligned} \right\}, \quad (7.9)$$

$$\frac{1}{Sc} [(1 + 2\eta k)g'' + 2kg'] + fg' - \frac{1}{2}\eta Sg' - Kgh^2 = 0, \quad (7.10)$$

$$\frac{\lambda^*}{Sc} [(1 + 2\eta k)h'' + 2kh'] + fh' - \frac{1}{2}\eta Sh' + Kgh^2 = 0, \quad (7.11)$$

with BC's as

$$\left. \begin{aligned} & f(0) = 0, f'(0) = 1, \theta(0) = 1, g'(0) = K_s g(0), \lambda^* h'(0) = -K_s g(0), \\ & f'(\infty) = 0, f''(\infty) = 0, \theta(\infty) = 0, g(\infty) = 1, h(\infty) = 0 \end{aligned} \right\}. \quad (7.12)$$

In which $k \left(= \frac{1}{R} \sqrt{\frac{\nu(1-\alpha t)}{a}} \right)$ is the curvature parameter, $De_1 \left(= \frac{\lambda_1 a}{1-\alpha t} \right)$ and $De_2 \left(= \frac{\lambda_2 a}{1-\alpha t} \right)$ are the Deborah numbers, $S \left(= \frac{a}{\sigma} \right)$ the unsteadiness parameter, $\text{Pr} \left(= \frac{\nu}{\alpha_1} \right)$ the Prandtl number and $Sc \left(= \frac{\nu}{D_{A^*}} \right)$ the Schmidt number, $\beta_t \left(= \frac{\lambda_t a}{1-\alpha t} \right)$ the thermal relaxation parameter, $\lambda^* \left(= \frac{D_{B^*}}{D_{A^*}} \right)$ the ratio of the diffusion coefficient, $K_s \left(= \frac{k_s}{D_{A^*}} \sqrt{\frac{\nu(1-\alpha t)}{a}} \right)$ the strength of heterogeneous reaction, $K \left(= \frac{k_c(1-\alpha t)a^2}{a} \right)$ the strength of homogeneous reaction.

Here, assumed that the D_{A^*} and D_{B^*} are comparable, that is $\lambda^* (= 1)$ and so

$$m(\eta) + h(\eta) = 1. \quad (7.13)$$

Thus Eqs. (7.10) – (7.11) and their respective BC's take the form

$$\frac{1}{Sc} [(1 + 2\eta k)g'' + 2kg'] + fg' - \frac{1}{2}\eta Sg' - Kg(1-g)^2 = 0, \quad (7.14)$$

$$g'(0) = K_s g(0), g(\eta) \rightarrow 1 \text{ as } \eta \rightarrow \infty. \quad (7.15)$$

7.2 Homotopic solution

Employing the homotopy analysis procedure, we have significant freedom in selecting the command functions and linear operators to get considerable proper approximations of our problem. This adaptability allows us to successfully tackle a highly nonlinear problem and obtain satisfactory outcomes.

Considering

$$f_o(\eta) = 1 - e^{-\eta}, \quad \theta_o(\eta) = e^{-\eta} \quad \text{and} \quad g_o(\eta) = 1 - \frac{1}{2}e^{-\eta k_s}, \quad (7.16)$$

$$\mathcal{L}_f(\eta) = \frac{\partial^3 f}{\partial \eta^3} - \frac{\partial f}{\partial \eta}, \quad \mathcal{L}_\theta(\eta) = \frac{\partial^2 \theta}{\partial \eta^2} - \theta \quad \text{and} \quad \mathcal{L}_g(\eta) = \frac{\partial^2 g}{\partial \eta^2} - g, \quad (7.17)$$

satisfying

$$\left. \begin{aligned} \mathcal{L}_f [c_0 + c_1 e^\eta + c_2 e^{-\eta}] &= 0 \\ \mathcal{L}_\theta [c_3 e^\eta + c_4 e^{-\eta}] &= 0 \\ \mathcal{L}_g [c_5 e^\eta + c_6 e^{-\eta}] &= 0 \end{aligned} \right\}, \quad (7.18)$$

where c_i ($i = 0, 1, \dots, 6$) are the constants.

7.2.1 Convergence region

The convergence of the HAM solution is presented in this section. The HAM has the ability to govern and regulate the problem convergence. The \hbar -curves for velocity, thermal, and solutal fields are sketched in **Fig. 7.1** at the 17th order of approximation. According to Liao [70], all of the curves in this figure have a horizontal line segment that defines the valid zone of \hbar . For instance, when $k = S = De_1 = De_2 = 0.1$, $\beta_t = 0.1$, $Pr = 6.5$, $K = 0.1$, $K_s = 1.1$, and $Sc = 1$

the convergence intervals for f , θ and g are respectively $-1.78 \leq \hbar_f \leq 0.03$, $-1.36 \leq \hbar_\theta \leq 0.21$ and $-1.33 \leq \hbar_g \leq 0.21$.

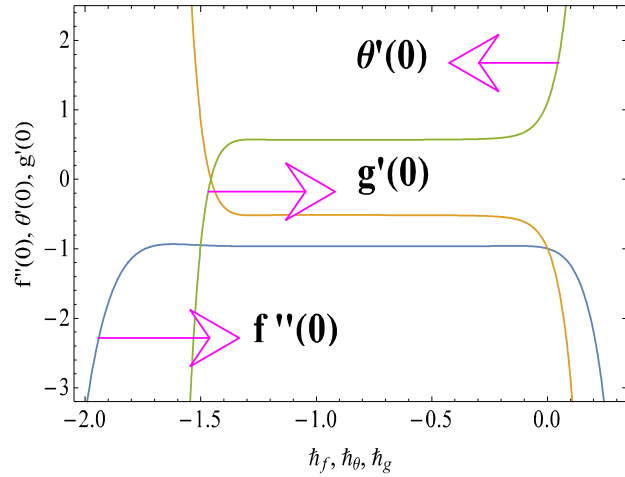


Fig. 7.1: The \hbar curves for f , θ and g .

7.3 Analysis and discussion of results

This section provides the analysis and discussion of the findings from the governing Eqs. (7.8) to (7.12) that describe the flow behavior, and thermal and solutal transport of unsteady axisymmetric Oldroyd-B material due to stretching cylinder.

7.3.1 Analysis of results

This section encloses a detailed conversation of the series solution with the impacts of the diverse material parameters on different distributions. To comprehend the physical behavior of these findings, simulations for various values: De_1 ($0.1 \leq De_1 \leq 1.0$), De_2 ($0.1 \leq De_2 \leq 1.0$), k ($0.1 \leq k \leq 0.7$), S ($0.1 \leq S \leq 0.4$), β_t ($0.1 \leq \beta_t \leq 0.4$), Pr ($6.5 \leq Pr \leq 8$), K ($0.1 \leq K \leq 0.7$)

and Ks ($1.1 \leq Ks \leq 1.4$) are performed. The characteristics of Deborah numbers for fluid relaxation and retardation times, the curvature parameter, and the unsteadiness parameter on a dimensionless velocity profile are discussed in **Fig. 7.2** to **Fig. 7.5**. It is reported that the fluid velocity displays the opposite behavior for fluid relaxation and retardation times while it enhances as the curvature and unsteadiness parameter increases. The graphic illustrations for thermal relaxation time, fluid relaxation time, fluid retardation time, curvature parameter, Prandtl number, and unsteadiness parameter are displayed in **Fig. 7.6** to **Fig. 7.11**. The temperature of the fluid boostup for fluid the relaxation time, curvature, and unsteadiness parameter while it drops down for the thermal relaxation time, fluid retardation time and Prandtl number. The graphic illustrations for the homogeneous reaction parameter, heterogeneous reaction parameter, unsteadiness parameter, and curvature parameter are shown through **Fig. 7.8** to **Fig. 7.15**. The solutal transport rate declines for the homogeneous and heterogeneous strength while it grows for unsteadiness and curvature parameters. Further, a comparison with earlier publicized upshots proposed in Refs [86, 87] is done to provide the exactness of the current analytical data, as listed in **Table 7.1**. This table delivers a satisfactory match between current results and earlier results. This certifies the exactness of our analytical study.

7.3.2 Discussion of results

To comprehend the impact of physical constraints on the dimensionless fluid velocity, thermal, and solutal distributions various graphs have been drawn in this section. These graphs confirm the significant contributions of changing physical parameters. For fluid relaxation and retardation phenomenon, the fluid velocity exhibit opposing behavior, as seen in **Fig. 7.2** and **Fig. 7.3**. This is because De_2 and De_1 are, respectively, directly proportional to retardation and

relaxation times. As a result, an augmentation in relaxation time generates the flexible forces that maintain liquid movement to become more robust, generating the liquid to conduct more like a solid, and consequently declining fluid velocity. In contrast to the relaxation time, the retardation time demonstrates the opposite behavior on the velocity profile. In reality, when the retardation time improves, flexible forces reduce, and the velocity profile enhances. Furthermore, as k increases, the radius of the cylinder reduces, and therefore fluid velocity increases as a result of less resistance to fluid motion, as seen in **Fig. 7.4**. Also, it is noted that there is no motion far from the surface. **Fig. 7.5** clearly shows that the velocity increases as the unsteadiness parameter S is improved. Physically, an increase in unsteadiness improves the liquid acceleration, which contributes to enhancing the velocity field.

The fluid temperature drops as β_t increase, as shown in **Fig. 7.6**. Physically, β_t is the governing parameter for the propagation of heat waves in the fluid in the Fourier heat flux model. As a result, increasing β_t lowers the heat transfer in the fluid. The temperature distribution improves under the influence of De_1 while showing a reverse trend for De_2 , as shown in **Fig. 7.7** and **Fig. 7.8**. The relaxation time increases as Deborah number value rise. It is a well-known fact that fluid having higher relaxation times have higher thermal properties, whereas fluids with smaller relaxation time have lower thermal properties. In light of this debate, higher De_1 improves the thermal distribution. Further, the retardation time rises as De_2 values boostup. Such an upsurge in the retardation time causes the temperature distribution to deplete. According to **Fig. 7.9**, the thermal field responds to the curvature parameter k in a dual manner. For the smaller significances of η it declines far from the surface whereas, near the surface of a cylinder, it boosts. This is due to the fact that the resistance between the fluid and the cylinder surface reduces as the cylinder's radius increases with a

gradual increase in k . It is clear from **Fig. 7.10** that, when $Pr (= 6.5)$ compared to $Pr (= 8.0)$, the penetration-depth of a curve $\theta(\eta)$ is significantly higher. Physically, the thermal diffusivity determines the Prandtl number, and the higher values of Pr result in weaker thermal diffusivity, which translates into a lower temperature field and thins the thermal layer. The unsteadiness parameter discussed in **Fig. 7.11** strengthened particles interactions, which indirectly improves the thermal conductivity. That is why thermal distribution rises for the increasing unsteadiness parameter.

The solutal distribution and associated thickness of the boundary layer are seen to decrease for K , as depicted in **Fig. 7.12**. Physically, reaction rates influence diffusion coefficients. Additionally, comparable outcomes for rising values of K_s are drawn in **Fig. 7.13** since the diffusion rate decreases as the reaction rate increases. The concentration distribution exhibits increasing behavior for the increasing values of the unsteadiness parameter S , as seen in **Fig. 7.14**. Since the particles interactions are enhanced by the unsteadiness parameter, the thermal conductivity is also indirectly enhanced, causing concentration fields to expand. **Fig. 7.15** portrays the curvature parameter outcome on the solutal distribution. According to these findings, it is observed that the concentration distribution decreases nearer the cylinder's surface while increases far away from the surface.

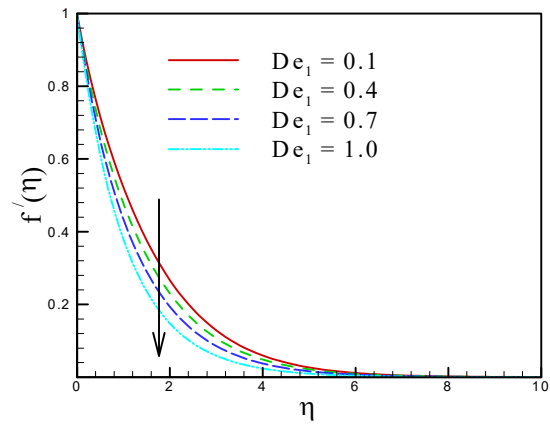


Fig. 7.2: Plot of $f'(\eta)$ for De_1 .

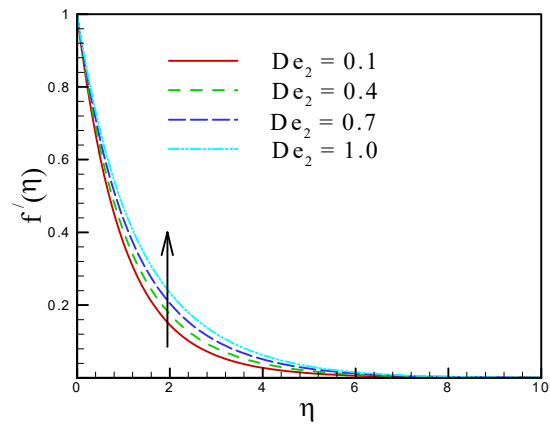


Fig. 7.3: Plot of $f'(\eta)$ for De_2 .

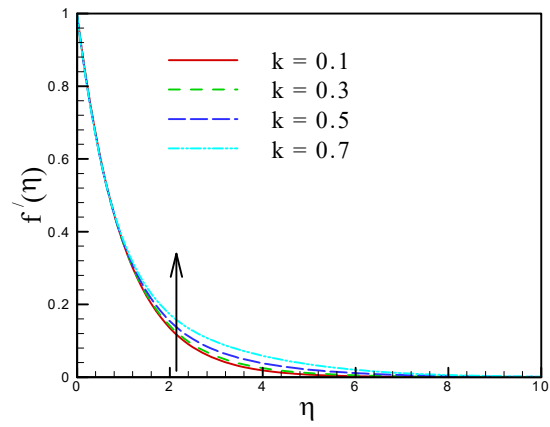


Fig. 7.4: Plot of $f'(\eta)$ for k .

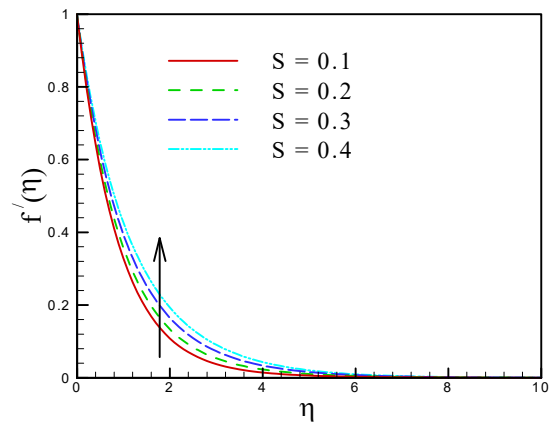


Fig. 7.5: Plot of $f'(\eta)$ for S .

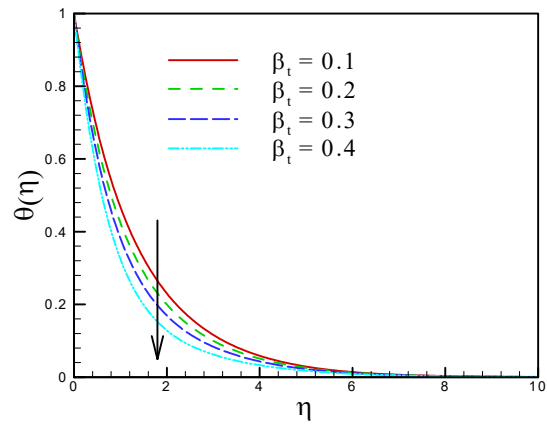


Fig. 7.6: Plot of $\theta(\eta)$ for β_t .

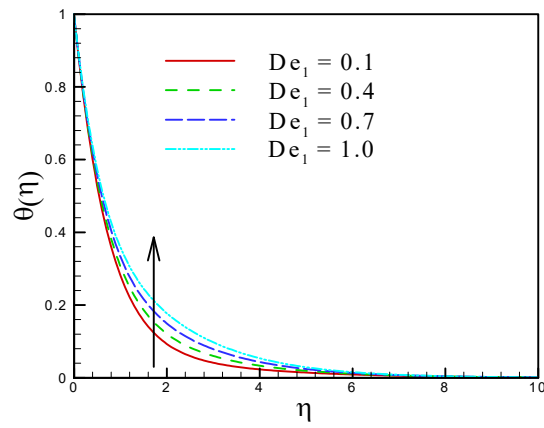


Fig. 7.7: Plot of $\theta(\eta)$ for De_1 .

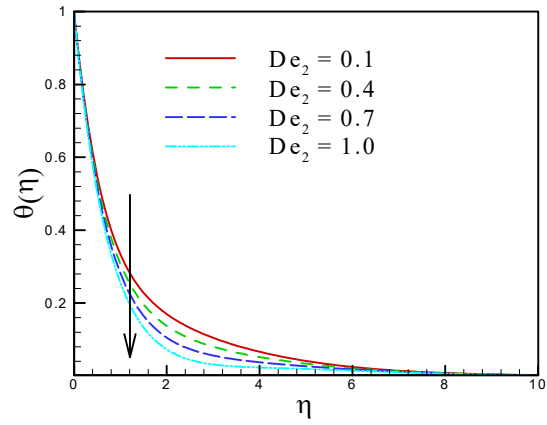


Fig. 7.8: Plot of $\theta(\eta)$ for De_2 .

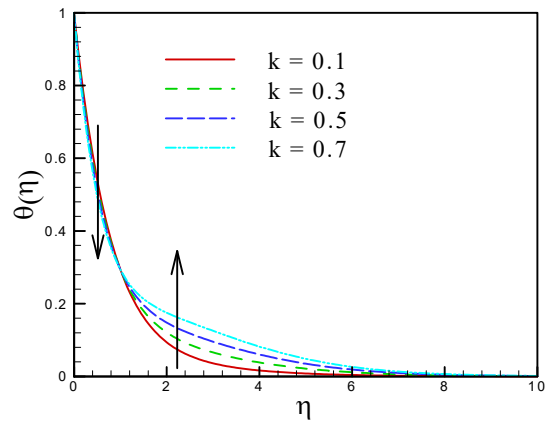


Fig. 7.9: Plot of $\theta(\eta)$ for k .

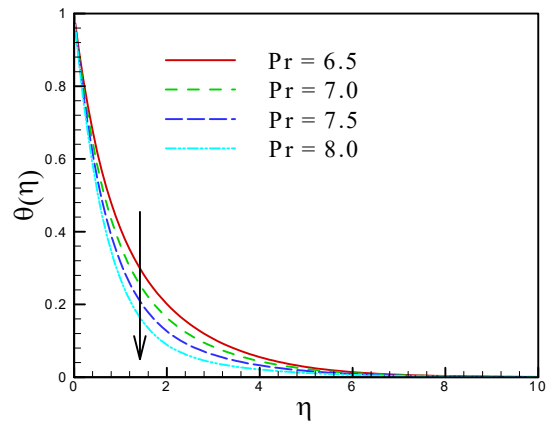


Fig. 7.10: Plot of $\theta(\eta)$ for Pr.

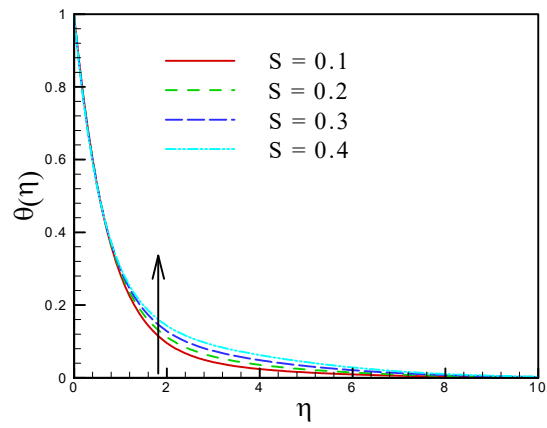


Fig. 7.11: Plot of $\theta(\eta)$ for S.

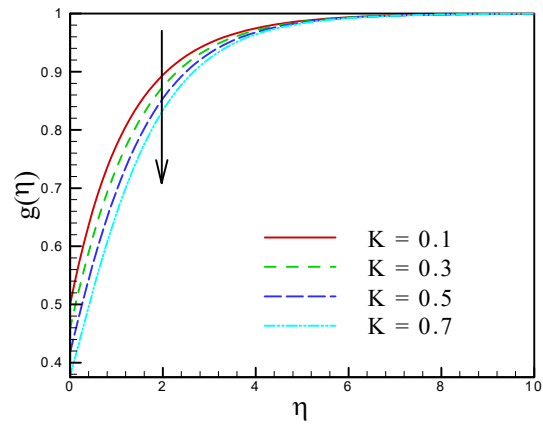


Fig. 7.12: Plot of $g(\eta)$ for K .

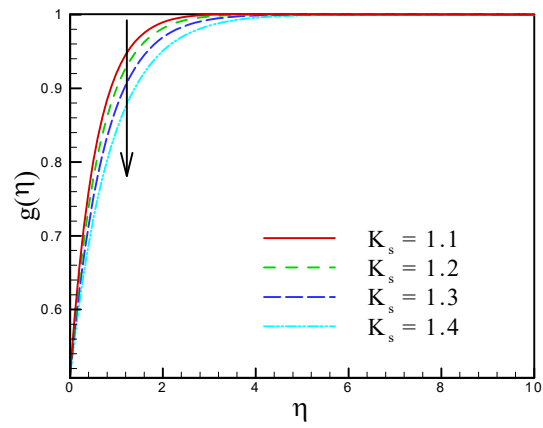


Fig. 7.13: Plot of $g(\eta)$ for K_s .

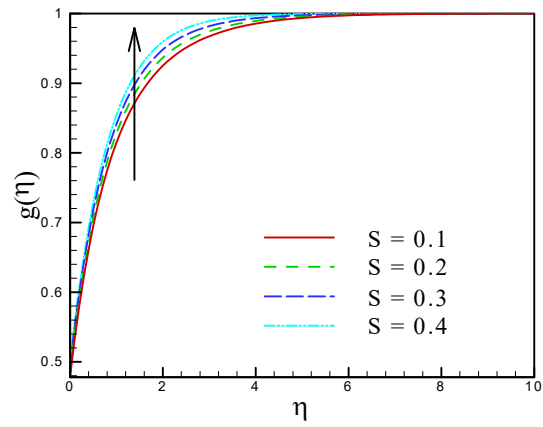


Fig. 7.14: Plot of $g(\eta)$ for S .

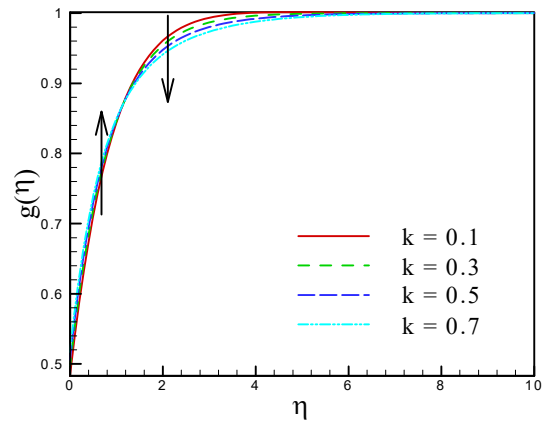


Fig. 7.15: Plot of $g(\eta)$ for k .

Table. 7.1: Comparison of $f''(0)$ for unsteadiness parameter when $k = De_1 = De_2 = 0$.

S	Sharidan <i>et al.</i> [86]	Chamkha <i>et al.</i> [87]	Present results
0.8	-1.261042	-1.261512	-1.261517
1.2	-1.377722	-1.378052	-1.377892
2.0	-1.587362	-	-1.587141

Chapter 8

Flow of Oldroyd-B Nanofluid in Non-Inertial Frame Inspired by Cattaneo-Christov Theory

In this chapter, the rotating flow of an Oldroyd-B nanofluid fluid bounded by a stretching surface is examined using the Cattaneo-Christov theory. A significant perspective of this endeavor is to include the consequences of Buongiorno's model of nanofluids because of their improved heat transport. The order analysis approach is adopted to present mathematical modeling of momentum and energy laws. Using flow similarities, the PDEs are transformed into ODEs. A well-known semi-analytical method called the homotopic technique is used to construct the series solution of produced ordinary differential equations. To explore how different physical flow factors, affects the fluid velocity, temperature, and concentration, the graphical results are sketched. Our findings show that thermal and solutal relaxation factors have a diminishing effect on the temperature and concentration distributions. Also, due to the incorporation

of elastic effects, we have discovered that the hydrodynamic boundary layer grows thinner. Further, the rotation parameter also reduces the thickness of the boundary layer.

8.1 Physical model and mathematical formulation

The motion of an incompressible three-dimensional Oldroyd-B nanofluid flow bounded by the stretching surface is considered in the current chapter. The surface associated in the xy -plane and fluid is assumed in the region $z > 0$. The surface stretching velocity is $u_w = ax$, which induces the flow in the surrounding layers of fluid. The fluid is rotated uniformly around the z -axis with a constant angular velocity Ω . The temperature and concentration conservation equations are modified to account for the thermal and solutal relaxation effects by using the Cattaneo-Christov theory with Brownian motion and thermophoresis phenomenon. The assumed surface is isothermal, that is, the constant temperature and concentration are denoted by T_w and C_w , while outside the thermal and solutal boundary layer are denoted by T_∞ and C_∞ .

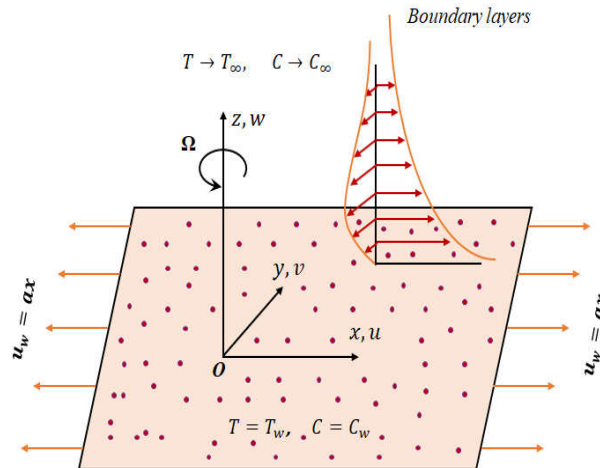


Fig. 8.1: The problem's geometry and coordinate system.

In the context of the overhead assumptions, the governing equations are [88]:

$$\frac{\partial u}{\partial x} + \frac{\partial v}{\partial y} + \frac{\partial w}{\partial z} = 0, \quad (8.1)$$

$$u \frac{\partial u}{\partial x} + v \frac{\partial u}{\partial y} + w \frac{\partial u}{\partial z} - 2\Omega v + \lambda_1 \left\{ \begin{array}{l} u^2 \frac{\partial^2 u}{\partial x^2} + v^2 \frac{\partial^2 u}{\partial y^2} + w^2 \frac{\partial^2 u}{\partial z^2} \\ 2uv \frac{\partial^2 u}{\partial x \partial y} + 2vw \frac{\partial^2 u}{\partial y \partial z} + 2uw \frac{\partial^2 u}{\partial x \partial z} \\ -2\Omega \left(u \frac{\partial v}{\partial x} + v \frac{\partial v}{\partial y} + w \frac{\partial v}{\partial z} \right) + 2\Omega \left(v \frac{\partial u}{\partial x} - u \frac{\partial u}{\partial y} \right) \end{array} \right\}, \quad (8.2)$$

$$= \nu \left\{ \frac{\partial^2 u}{\partial z^2} + \lambda_2 \left(u \frac{\partial^3 u}{\partial x \partial z^2} + v \frac{\partial^3 u}{\partial y \partial z^2} + w \frac{\partial^3 u}{\partial z^3} - \frac{\partial u}{\partial x} \frac{\partial^2 u}{\partial z^2} - \frac{\partial u}{\partial y} \frac{\partial^2 v}{\partial z^2} - \frac{\partial u}{\partial z} \frac{\partial^2 w}{\partial z^2} \right) \right\}$$

$$u \frac{\partial v}{\partial x} + v \frac{\partial v}{\partial y} + w \frac{\partial v}{\partial z} + 2\Omega u + \lambda_2 \left\{ \begin{array}{l} u^2 \frac{\partial^2 v}{\partial x^2} + v^2 \frac{\partial^2 v}{\partial y^2} + w^2 \frac{\partial^2 v}{\partial z^2} \\ 2uv \frac{\partial^2 v}{\partial x \partial y} + 2vw \frac{\partial^2 v}{\partial y \partial z} + 2uw \frac{\partial^2 v}{\partial x \partial z} \\ +2\Omega \left(u \frac{\partial u}{\partial x} + v \frac{\partial u}{\partial y} + w \frac{\partial u}{\partial z} \right) + 2\Omega \left(v \frac{\partial v}{\partial x} - u \frac{\partial v}{\partial y} \right) \end{array} \right\}, \quad (8.3)$$

$$= \nu \left\{ \frac{\partial^2 v}{\partial z^2} + \lambda_2 \left(u \frac{\partial^3 v}{\partial x \partial z^2} + w \frac{\partial^3 v}{\partial z^3} + v \frac{\partial^3 v}{\partial y \partial z^2} - \frac{\partial v}{\partial x} \frac{\partial^2 u}{\partial z^2} - \frac{\partial v}{\partial z} \frac{\partial^2 w}{\partial z^2} - \frac{\partial v}{\partial y} \frac{\partial^2 v}{\partial z^2} \right) \right\}$$

In addition, using Eqs. (1.10 to 1.13), the following PDEs are produced for the phenomena of thermal and solutal energy transport in an Oldroyd-B fluid (cf. Chapter 1)

$$u \frac{\partial T}{\partial x} + v \frac{\partial T}{\partial y} + w \frac{\partial T}{\partial z} - \tau \left\{ D_B \left(\frac{\partial C}{\partial z} \frac{\partial T}{\partial z} \right) + \frac{D_T}{T_\infty} \left(\frac{\partial T}{\partial z} \right)^2 \right\}$$

$$+ \lambda_t \left\{ \begin{array}{l} u^2 \frac{\partial^2 T}{\partial x^2} + v^2 \frac{\partial^2 T}{\partial y^2} + w^2 \frac{\partial^2 T}{\partial z^2} + 2uv \frac{\partial^2 T}{\partial x \partial y} + 2vw \frac{\partial^2 T}{\partial y \partial z} \\ +2uw \frac{\partial^2 T}{\partial x \partial z} + u \frac{\partial u}{\partial x} \frac{\partial T}{\partial x} + u \frac{\partial v}{\partial x} \frac{\partial T}{\partial y} + u \frac{\partial w}{\partial x} \frac{\partial T}{\partial z} + v \frac{\partial u}{\partial y} \frac{\partial T}{\partial x} \\ +v \frac{\partial v}{\partial y} \frac{\partial T}{\partial y} + u \frac{\partial w}{\partial x} \frac{\partial T}{\partial z} + w \frac{\partial u}{\partial z} \frac{\partial T}{\partial x} + w \frac{\partial v}{\partial z} \frac{\partial T}{\partial y} + w \frac{\partial w}{\partial z} \frac{\partial T}{\partial z} \end{array} \right\}, \quad (8.4)$$

$$- \lambda_t \tau D_B \left\{ u \frac{\partial^2 C}{\partial x \partial z} \frac{\partial T}{\partial z} + u \frac{\partial C}{\partial z} \frac{\partial^2 T}{\partial x \partial z} + v \frac{\partial^2 C}{\partial y \partial z} \frac{\partial T}{\partial z} + v \frac{\partial C}{\partial z} \frac{\partial^2 T}{\partial y \partial z} + w \frac{\partial^2 C}{\partial z^2} \frac{\partial T}{\partial z} + w \frac{\partial C}{\partial z} \frac{\partial^2 T}{\partial z^2} \right\}$$

$$- 2\lambda_t \tau \frac{D_T}{T_\infty} \left\{ u \frac{\partial T}{\partial z} \frac{\partial^2 T}{\partial x \partial z} + v \frac{\partial T}{\partial z} \frac{\partial^2 T}{\partial y \partial z} + w \frac{\partial T}{\partial z} \frac{\partial^2 T}{\partial z^2} \right\} = \alpha_1 \frac{\partial^2 T}{\partial z^2}$$

$$\left. \begin{aligned}
& u \frac{\partial C}{\partial x} + v \frac{\partial C}{\partial y} + w \frac{\partial C}{\partial z} - \lambda_c \frac{D_T}{T_\infty} \left\{ u \frac{\partial^3 T}{\partial x \partial z^2} + v \frac{\partial^3 T}{\partial y \partial z^2} + w \frac{\partial^3 T}{\partial z^3} \right\} \\
& + \lambda_c \left\{ \begin{aligned}
& u^2 \frac{\partial^2 C}{\partial x^2} + v^2 \frac{\partial^2 C}{\partial y^2} + w^2 \frac{\partial^2 C}{\partial z^2} + 2uv \frac{\partial^2 C}{\partial x \partial y} + 2vw \frac{\partial^2 C}{\partial y \partial z} \\
& + 2uw \frac{\partial^2 C}{\partial x \partial z} + u \frac{\partial u}{\partial x} \frac{\partial C}{\partial x} + u \frac{\partial v}{\partial x} \frac{\partial C}{\partial y} + u \frac{\partial w}{\partial x} \frac{\partial C}{\partial z} + v \frac{\partial u}{\partial y} \frac{\partial C}{\partial x} \\
& + v \frac{\partial v}{\partial y} \frac{\partial C}{\partial y} + v \frac{\partial w}{\partial y} \frac{\partial C}{\partial z} + w \frac{\partial u}{\partial z} \frac{\partial C}{\partial x} + w \frac{\partial v}{\partial z} \frac{\partial C}{\partial y} + w \frac{\partial w}{\partial z} \frac{\partial C}{\partial z}
\end{aligned} \right\} \\
& = D_B \frac{\partial^2 C}{\partial z^2} + \frac{D_T}{T_\infty} \left(\frac{\partial^2 T}{\partial z^2} \right)
\end{aligned} \right\}, \quad (8.5)$$

with corresponding BC's

$$\left. \begin{aligned}
& u = u_w, \quad v = 0, \quad w = 0, \quad T = T_w \text{ and } C = C_w \text{ at } z = 0 \\
& u \rightarrow 0, \quad v \rightarrow 0, \quad T \rightarrow T_\infty \text{ and } C \rightarrow C_\infty \text{ as } z \rightarrow \infty
\end{aligned} \right\}. \quad (8.6)$$

Letting the similarity transformations

$$\left. \begin{aligned}
& u = axf'(\eta), \quad v = axg(\eta), \quad w = -\sqrt{a\nu}f(\eta), \quad \eta = \sqrt{\frac{a}{\nu}}z, \\
& \theta = \frac{T-T_\infty}{T_w-T_\infty}, \quad \phi = \frac{C-C_\infty}{C_w-C_\infty}
\end{aligned} \right\}. \quad (8.7)$$

The overhead similarity transformations satisfy the continuity equation (8.1) and transform the above motion equations into ODEs as follows

$$f''' + ff'' - f'^2 + 2\lambda(g - De_1fg') + De_1(2ff'f'' - f^2f''') + De_2(f''^2 - ff^{iv}) = 0, \quad (8.8)$$

$$\left. \begin{aligned}
& g'' + fg' - f'g - 2\lambda\{f' + De_1(f'^2 - ff'' + g^2)\} + De_1(2ff'g' - f^2g'') \\
& + De_2(f'g'' - fg''' - gf''' + g'f'') = 0
\end{aligned} \right\}, \quad (8.9)$$

$$\left. \begin{aligned} & \theta'' + \text{Pr} (f + g) \theta' + \text{Pr} \{N_b \theta' \phi' + N_t \theta'^2\} \\ & - \text{Pr} \beta_t \left\{ (f + g) (f' + g') \theta' + (f + g)^2 \right\} \theta'' \\ & - \text{Pr} \beta_t N_b \left\{ (f + g) \theta'' \phi' + (f + g) \theta' \phi'' \right\} - 2 \text{Pr} \beta_t N_t (f + g) \theta' \theta'' = 0 \end{aligned} \right\}, \quad (8.10)$$

$$\left. \begin{aligned} & \phi'' + \text{Pr} Le (f + g) \phi' + \text{Pr} Le \frac{N_t}{N_b} \theta'' - \text{Pr} Le \beta_c \left\{ (f + g) (f' + g') \phi' + (f + g)^2 \phi'' \right\} \\ & - \text{Pr} Le \frac{N_t}{N_b} (f + g) \theta''' = 0 \end{aligned} \right\}. \quad (8.11)$$

with the corresponding BC's as

$$\left. \begin{aligned} & f(0) = 0, \quad g(0) = 0, \quad f'(0) = 1, \quad \theta(0) = 1, \quad \phi(0) = 1, \\ & f'(\infty) = 0, \quad g(\infty) = 0, \quad \theta(\infty) = 0, \quad \phi(\infty) = 0 \end{aligned} \right\}. \quad (8.12)$$

The physical parameters are expressed as: $De_1 (= \lambda_1 a)$ is the fluid relaxation time parameter, $De_2 (= \lambda_2 a)$ the fluid retardation time parameter, $\lambda (= \frac{\Omega}{a})$ the rotation parameter, $\beta_t (= \lambda_t a)$ the thermal relaxation time parameter, $\beta_c (= \lambda_c a)$ the solutal relaxation time parameter, $N_b (= \frac{\tau D_B (C_w - C_\infty)}{\nu})$ the Brownian diffusion coefficient, $N_t (= \frac{\tau D_T (T_w - T_\infty)}{\nu T_\infty})$ the thermophoresis parameter, $\text{Pr} (= \frac{\nu}{\alpha_1})$ the Prandtl number, and $Le (= \frac{\alpha_1}{D_B})$ the Lewis number.

8.2 Solution procedure

For the convergent series solution of ODEs, the homotopic method is employed. To accomplish this, one needed the proper linear operators and initial hypotheses as stated below:

$$f_o(\eta) = 1 - e^{-\eta}, \quad g_o(\eta) = 0, \quad \theta_o(\eta) = e^{-\eta} \quad \text{and} \quad \phi_o(\eta) = e^{-\eta}, \quad (8.13)$$

$$\mathcal{L}_f = \frac{\partial^3 f}{\partial \eta^3} - \frac{\partial f}{\partial \eta}, \quad \mathcal{L}_g = \frac{\partial^2 g}{\partial \eta^2} - g, \quad \mathcal{L}_\theta = \frac{\partial^2 \theta}{\partial \eta^2} - \theta \quad \text{and} \quad \mathcal{L}_\phi = \frac{\partial^2 \phi}{\partial \eta^2} - \phi, \quad (8.14)$$

satisfying

$$\left. \begin{aligned} \mathcal{L}_f &= [c_0 + c_1e^\eta + c_2e^{-\eta}], \mathcal{L}_g = [c_3e^\eta + c_4e^{-\eta}] \\ \mathcal{L}_\theta &= [c_5e^\eta + c_6e^{-\eta}], \mathcal{L}_\phi = [c_7e^\eta + c_8e^{-\eta}] \end{aligned} \right\}, \quad (8.15)$$

where c_i ($i = 0, 1, 2, \dots, 8$) are the constants.

The general solutions can be expressed as

$$\left. \begin{aligned} f_m(\eta) &= f_m^*(\eta) + c_0 + c_1e^\eta + c_2e^{-\eta} \\ g_m(\eta) &= g_m^*(\eta) + c_3e^\eta + c_4e^{-\eta} \\ \theta_m(\eta) &= \theta_m^*(\eta) + c_5e^\eta + c_6e^{-\eta} \\ \phi_m(\eta) &= \phi_m^*(\eta) + c_7e^\eta + c_8e^{-\eta} \end{aligned} \right\}, \quad (8.16)$$

where $f_m^*(\eta)$, $g_m^*(\eta)$, $\theta_m^*(\eta)$ and $\phi_m^*(\eta)$ indicate the special solutions.

8.3 Convergence analysis

The convergence control variables h_f , h_g , h_θ and h_ϕ are employed in the homotopy analysis approach to producing the series solution. The series solution convergence region can be adjusted and controlled by these convergence control variables. Therefore, **Fig. 8.2** portrays the h -curves. It can be seen that the satisfactory values of h_f , h_g , h_θ and h_ϕ are $-1.45 \leq h_f \leq -0.34$, $-1.13 \leq h_g \leq -0.34$, $-1.13 \leq h_\theta \leq -0.34$, $-1.13 \leq h_\phi \leq -0.33$.

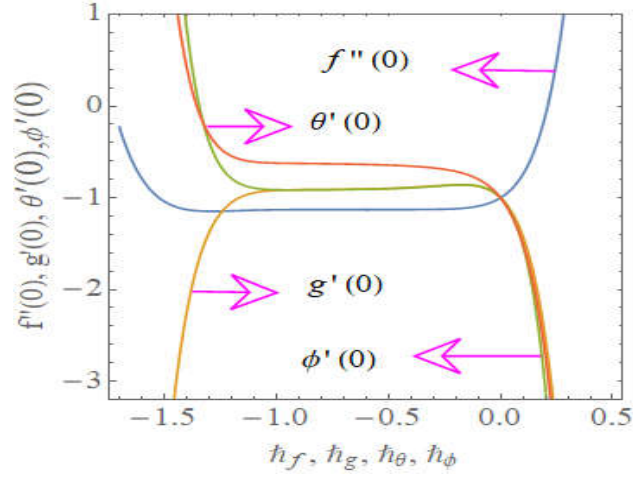


Fig. 8.2: The combined h -curves.

Further, in **Table 8.1**, the convergence of velocities, temperatures, and concentration is examined. The suggested values analyzed that the 16th order of approximations are adequate for $f''(0)$ and $g'(0)$ the 16th and 20th are satisfactory for $\theta'(0)$, and $\phi'(0)$.

Table. 8.1: The convergence analysis for $\lambda = 0.1$, $De_1 = De_2 = 0.2$, $N_t = N_b = 0.2$, $\beta_t = \beta_c = 0.1$, $Le = 2.0$, and $Pr = 6.2$.

Approximation order	$-f''(0)$	$-g'(0)$	$-\theta'(0)$	$-\phi'(0)$
1	1.16446	0.29512	0.64611	0.93613
5	1.22545	0.26895	0.53596	0.93341
8	1.23179	0.26364	0.53484	0.91738
12	1.23214	0.26299	0.53423	0.88818
16	1.23217	0.26293	0.53419	0.89586
20	1.23217	0.26293	0.53419	0.89447
25	1.23217	0.26193	0.53419	0.89447
30	1.23217	0.26193	0.53419	0.89447
35	1.23217	0.26193	0.53419	0.89447

8.4 Interpretation of graphical results

The thermal and solutal transport phenomena are investigated using the Cattaneo-Christov theory. The primary goal of this section is to present and explore the consequences of physical parameters on solutions. With the help of following numerical values, $0.0 \leq \lambda \leq 0.6$, $0.2 \leq De_1 \leq 1.8$, $0.2 \leq De_2 \leq 1.1$, $0.2 \leq N_t \leq 1.4$, $0.2 \leq N_b \leq 1.4$, $0.1 \leq \beta_t \leq 1.1$, $0.1 \leq \beta_c \leq 1.1$ and $6.2 \leq Pr \leq 7.3$, the graphical analysis of non-dimensional parameters are sketched.

Fig. 8.3(a) and **(b)** characterize the influence of rotation parameter λ on the velocities in the x and y -directions. The velocity around the z -axis seems to decrease as the velocity

in the x and y -directions increases. Further, a thinner boundary layer is seen as λ increases, since the rotation rate to stretching rate ratio improves. Physically, the larger rotational effects provide resistance to fluid motion in the x -direction, causing the boundary layer to thin.

The thermal and solutal fields are plotted in **Fig. 8.4(a)** and **(b)** for diverse values of rotation parameter λ . In **Fig. 8.4(a)** as the λ increases, the temperature rises, and the thermal boundary layer thickens. Physically, this is due to the fact that a larger rotation parameter gives the fluid more kinetic energy, which raises its temperature. And when the angular velocity is increased, the thickness of the concentration boundary layer grows as seen in **Fig. 8.4(b)**.

In **Fig. 8.5(a)** and **(b)** the thermal and solutal curves exhibit an increasing trend as the values of local Deborah number De_1 increase, while in **Fig. 8.6(a)** and **(b)** these curves shows the opposite behavior for the increasing values of De_2 . When these two figures are compared, it is evident that De_1 , and De_2 have completely different effects on the fluid temperature and concentration. Since De_1 is associated with relaxation time, while De_2 is affected by the retardation time. A higher relaxation time causes to rise the thermal and solutal transport rate, while higher retardation time causes heat and mass transport to fall.

The variations of the thermophoresis parameter N_t on temperature and concentration profiles are depicted through **Fig. 8.7(a)** and **(b)**, respectively. When we increase the thermophoresis parameter, we see that the fluid temperature and concentration and associated thermal and solutal boundary layer thickness are increased. In fact, the presence of nanoparticles increases the fluid's thermal conductivity. Stronger thermal conductivity can be seen as the thermophoresis parameter rises. The temperature and concentration and thickness of the thermal and solutal boundary layer are increased as a result of the increased thermal conductivity. This increased thermal conductivity raises the temperature and concentration and increases the

thickness of the boundary layers.

Fig. 8.8(a) and **(b)** depict the behavior of N_b as a function of thermal and solutal field. Increasing the values of N_b resulting in an increase in the temperature profile. Physically as the values of N_b are maximized, the random movement of fluid particles is also increased, resulting in the generation of heat, which raises the temperature of nanoparticles. But the Brownian motion parameter exhibits the opposite behavior.

Fig. 8.9(a) depicts the decreasing behavior of thermal relaxation time β_t as a function of temperature distribution. It is obvious that the temperature profile $\theta(\eta)$ is inversely proportional to thermal relaxation time. It means that the inclusion of thermal relaxation time reduces the temperature penetration depth. The effect of β_c on solutal distribution is revealed in **Fig. 8.9(b)**. The solutal distribution and the thickness of the boundary layer decrease as β_c increases. When we increase β_c , molecules require more time to transfer mass particles to neighboring particles, resulting in a weaker nanoparticle volume fraction.

Fig. 8.10 depicts the result of Pr on the thermal transport of an Oldroyd-B nanofluid. When the values of Pr are enhanced, the heat transportation rate slow down. Physically, increasing the Pr reduces the thermal conductivity of the liquid, which reduces conduction. This reduces the thickness of the thermal layer as well as the fluid temperature.

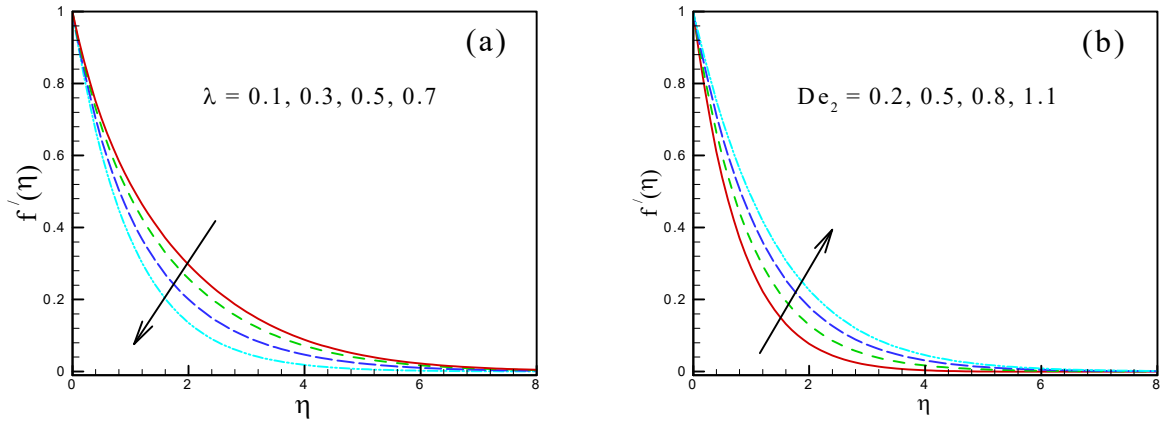


Fig. 8.3: Bearing of λ on $f'(\eta)$ and $g(\eta)$.

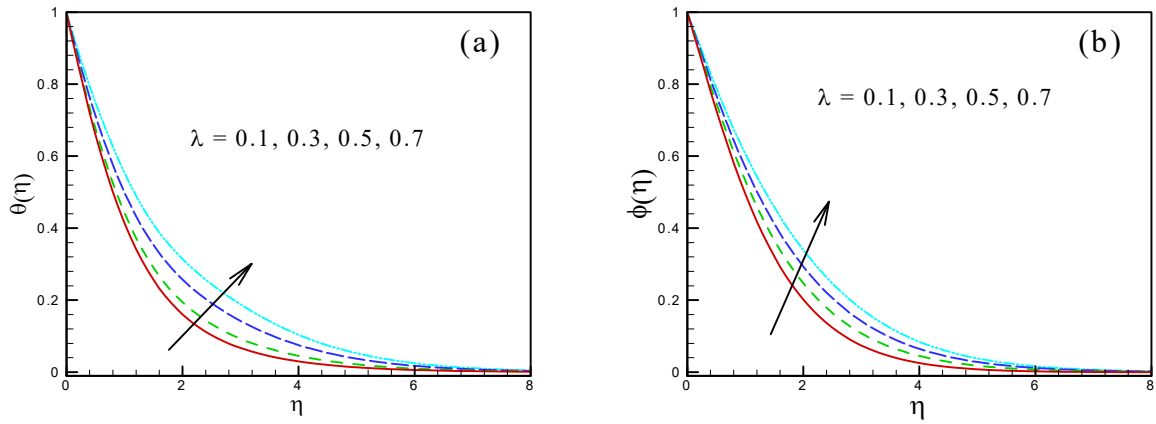


Fig. 8.4: Bearing of λ on $\theta(\eta)$ and $\phi(\eta)$.

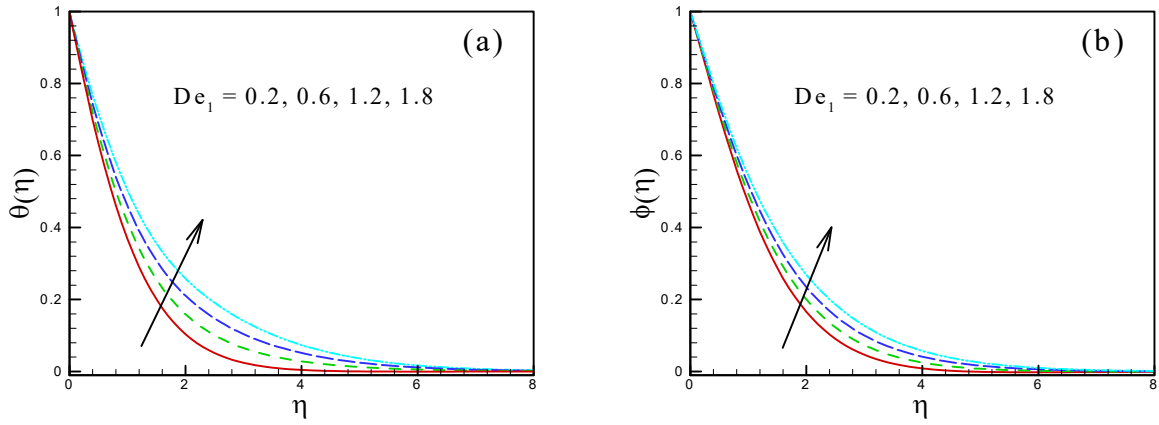


Fig. 8.5: Bearing of De_1 on $\theta(\eta)$ and $\phi(\eta)$.

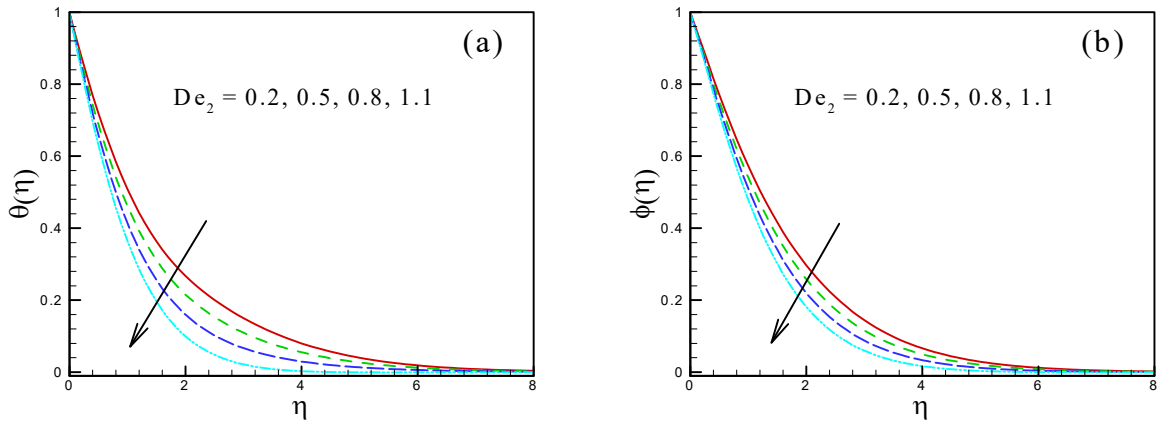


Fig. 8.6: Bearing of De_2 on $\theta(\eta)$ and $\phi(\eta)$.

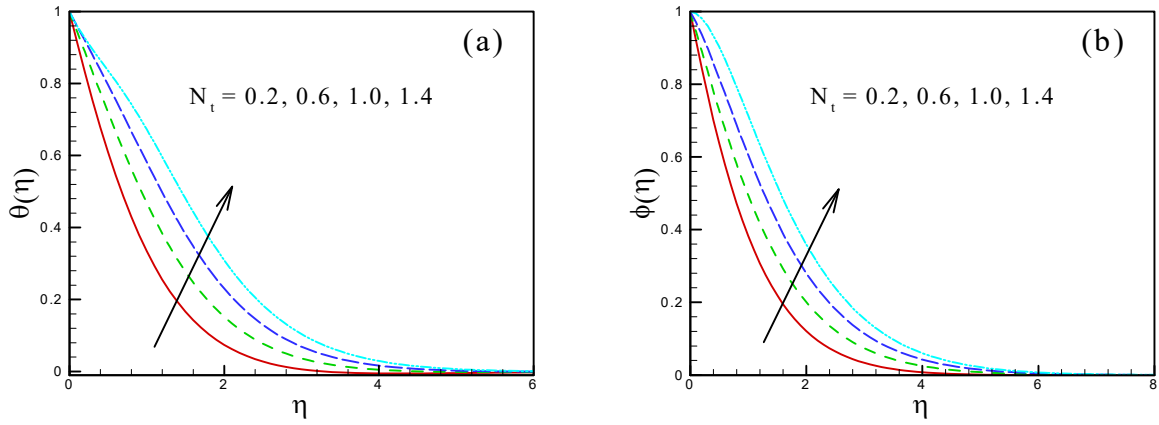


Fig. 8.7: Bearing of N_t on $\theta(\eta)$ and $\phi(\eta)$.

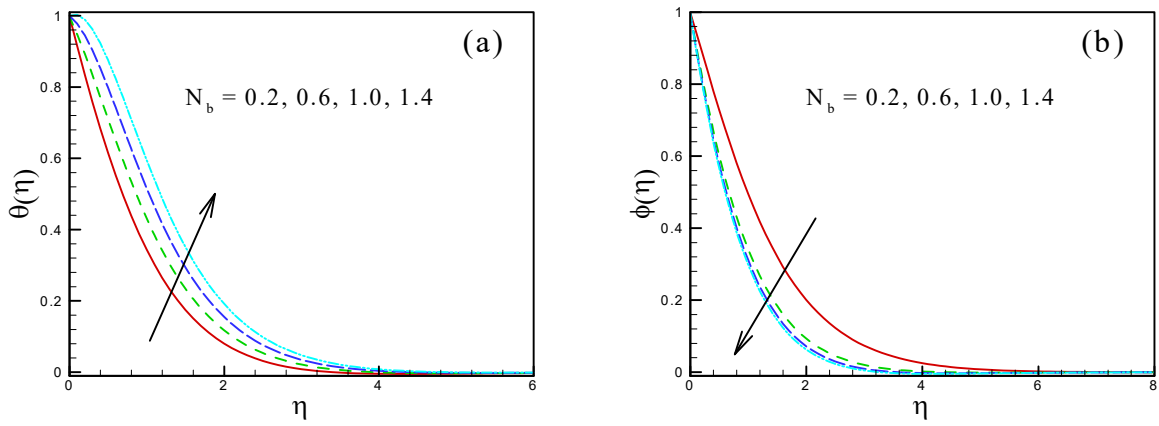


Fig. 8.8: Bearing of N_b on $\theta(\eta)$ and $\phi(\eta)$.

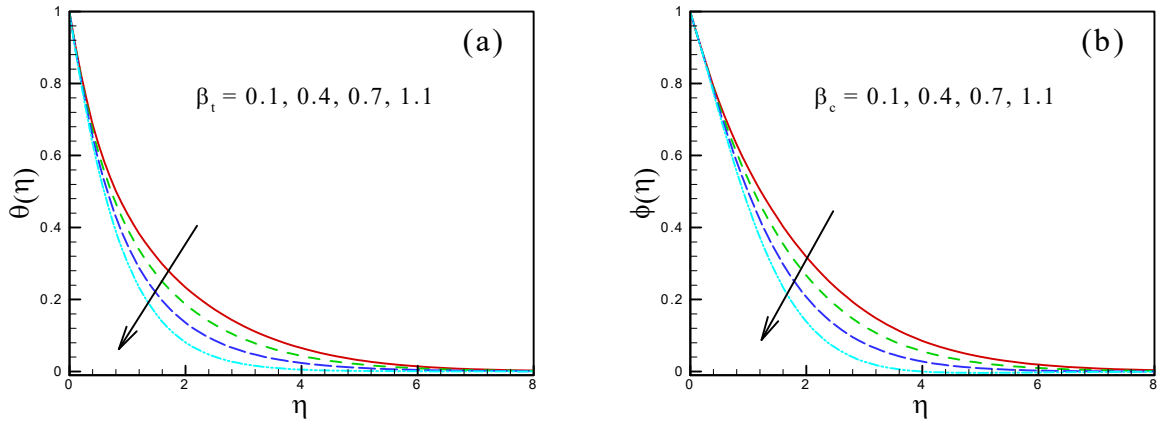


Fig. 8.9: Bearing of β_t and β_c on $\theta(\eta)$ and $\phi(\eta)$, respectively.

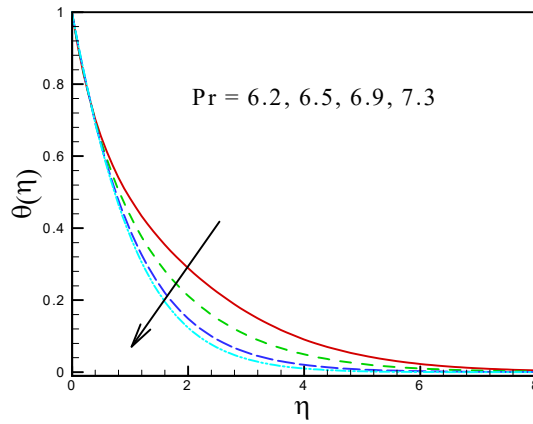


Fig. 8.10: Bearing of Pr on $\theta(\eta)$.

8.5 Results Authentication

A comparison with previously published results is suggested Abbasi *et al.* [84], which are presented in **Table 8.2**, is done to ensure the accuracy of the current numerical results. This table shows a valid relationship between existing findings and previous outcomes. This guarantees the accuracy of our study.

Table. 8.2: Comparison of $f''(0)$ for De_2 when $De_1 = 0.4$ and $\lambda = 0$.

De_2	Abbasi <i>et al.</i> [84]	Present results
0.0	1.101900	1.101651
0.2	1.004980	1.002254
0.4	0.929860	0.929245
0.6	0.869420	0.865375
0.8	0.819430	0.818217
1.0	0.777180	0.779144

Chapter 9

Concluding Remarks and Future

Directions

Analysis of the rheological characteristics of a viscoelastic Oldroyd-B fluid flow caused by stretching surface was the primary objective of the current theoretical work. Further, this investigation also included the general prediction of the thermal and solutal energy transport mechanisms in such flows. For this purpose, the flow phenomenon in the form of the partial differential equations is developed, and then these PDEs were converted into highly nonlinear ordinary differential equations using appropriate similarity transformations. To analyze the flow and energy transport features of an Oldroyd-B material, the solution of governing equations was computed by employing both the analytical and numerical methods. When examining this phenomena, the numerous physical impacts were taken into consideration. This conclusive chapter outlines the important findings of this thesis and suggests recommendations for further research.

9.1 Summary of results

The key outcomes of this research work are precised as follows:

- The increasing values of the relaxation time parameter increase the stress relaxation phenomenon which resulted in a reduction in the flow characteristics of the nanofluid, while retardation time parameter showed opposite behavior.
- The unsteadiness parameter tends to enhanced the velocity, temperature and concentration profiles.
- The velocity, temperature, and concentration distributions at the surface of the cylinder improved as the curvature parameter was increased.
- An increase in Brownian motion of nanoparticles converts kinetic energy to heat energy, which raised the temperature.
- An increase in the thermophoresis parameter resulted in a rise in the temperature gradient, which leded to an increase in the temperature of the nanoparticles.
- When the thermophoresis parameter was increased, the temperature difference between the wall and the free surface increases as well, and resulted in an increase in nanofluid concentration.
- The increase in Prandtl and Lewis numbers, respectively, decreased the temperature and concentration distributions.
- The magnetic field parameter increased the fluid velocity while it decreased the temperature field.

- Larger values of thermal and solutal Biot numbers enhanced the temperature and concentration distributions.
- Heat generation/absorption, Eckert number and solar radiation significantly boosted up the temperature field.
- It was noted that the temperature ratio parameter improved the heat transport rate.
- The increasing the activation energy parameter values expanded the nanoparticles concentration field.
- The addition of thermophoretic particles to the liquid stream reduced mass transfer. Additionally, as the value of N_t^* increases, mass transfer was decreased.
- The temperature and concentration fields were declined by the thermal and solutal relaxation parameters, β_t and β_c , respectively.
- The effect of the rotation parameter reduced the velocity field, whereas increasing the rotation parameter revealed an increase in the fluid temperature and concentration distributions.

9.2 Future recommendations

In this thesis, an investigation of the rheological characteristics of the Oldroyd-B fluid flow induced by stretching surface with thermal and solutal energy transport has received more focus. However, the outcomes of our both the numerical and analytical computations still leave space for additional developments and extensions in this work. So, there are a few recommendations that can be looked at in the upcoming research, and they are as follows:

- The mathematical modeling for unsteady Oldroyd-B fluid flow due to stretchable cylindrical stretching surface was presented in this work. However, it could be attractive to produce mathematical modeling for a rotating spherical surface.
- The energy transport phenomenon for an Oldroyd-B material generated by a rotating cone has not been studied yet. Therefore, thorough theoretical investigations can fill this gap.
- Future research may focus on the time-dependent three-dimensional flow of an Oldroyd-B fluid induced by a stretchable rotating cylinder under diverse physical effects.
- For the computation of these types of highly non-linear flow phenomena, innovative numerical techniques such as the finite volume approach and finite element method can be used to tackle the problems of diverse physical geometries.

Bibliography

- [1] J.G. Oldroyd, On the formulation of rheological equations of state, Proc. Royal Soc. Lond. Ser. A Math. Phys. Sci., 200 (1063) (1950) 523-541.
- [2] R.K. Bhatnagar, G. Gupta and K.R. Rajagopal, Flow of an Oldroyd-B fluid due to a stretching sheet in the presence of a free stream velocity, Int. J. Non-Linear Mech., 30 (1995) 391-405.
- [3] C. Fetecau and C. Fetecau, Decay of a potential vortex in an Oldroyd-B fluid, Int. J. Eng. Sci., 43 (2005) 340-351.
- [4] T. Hayat, Z. Hussain, M. Farooq, A. Alsaedi and M. Obaid, Thermally stratified stagnation point flow of an Oldroyd-B fluid, Int. J. Nonlinear Sci. Numer. Simul., 15 (1) (2014) 77-86.
- [5] F.G. Awad, S.M. Ahamed, P. Sibanda and M. Khumalo, The effect of thermophoresis on unsteady Oldroyd-B nanofluid flow over stretching surface, PLoS One, 10 (8) (2015) 0135914.
- [6] A. Hafeez, M. Khan and J. Ahmed, Flow of magnetized Oldroyd-B nanofluid over a rotating disk, Appl. Nanosci., 10 (2020) 5135-5147.

- [7] M. Khan, A. Hafeez and J. Ahmed, Impacts of non-linear radiation and activation energy on the axisymmetric rotating flow of Oldroyd-B fluid, *Physica A: Stat. Mech. Appl.*, 580 (2021) 124085.
- [8] F.K. Moore, Unsteady laminar boundary-layer flow, National Aeronautics and Space Administration, Washington DC, (1951).
- [9] B.T. Chao and D.R. Jeng, Unsteady stagnation point heat transfer, *J. Heat Transf.*, 87 (2) (1965) 221-230.
- [10] K.T. Yang, Unsteady laminar boundary layers in an incompressible stagnation flow, *J. Appl. Mech.*, 25 (4) (1958) 421-427.
- [11] C.Y. Wang, Liquid film on an unsteady stretching surface, *Q. Appl. Math.*, 48 (4) (1990) 601-610.
- [12] S. Khalili, H. Tamim, A. Khalili and M.M. Rashidi, Unsteady convective heat and mass transfer in pseudoplastic nanofluid over a stretching wall, *Adv. Powder Technol.*, 26 (5) (2015) 1319-1326.
- [13] C.S.K. Raju and N. Sandeep, Unsteady three-dimensional flow of Casson–Carreau fluids past a stretching surface, *Alex. Eng. J.*, **55 (2)** (2016) 1115-1126.
- [14] M. Khan and M. Azam, Unsteady heat and mass transfer mechanisms in MHD Carreau nanofluid flow, *J. Mol. Liq.*, 225 (2017) 554-562.
- [15] Y.X. Li, H. Waqas, K. Al-Khaled, S.A. Khan, M.I. Khan, S.U. Khan, R. Naseem and Y.M. Chu, Simultaneous features of Wu’s slip, nonlinear thermal radiation and activation energy

in unsteady bio-convective flow of Maxwell nanofluid configured by a stretching cylinder, *Chin. J. Phys.*, 73 (2021) 462-478.

- [16] E.R. El-Zahar, A.E.N. Mahdy, A.M. Rashad, W. Saad and L.F. Seddek, Unsteady MHD mixed convection flow of Non-Newtonian Casson hybrid nanofluid in the stagnation zone of sphere spinning impulsively, *Fluids*, 6 (6) (2021) 197.
- [17] S. Sindhu and B.J. Gireesha, Scrutinization of unsteady non-Newtonian fluid flow considering buoyancy effect and thermal radiation: Tangent hyperbolic model, *Int. Commun. Heat Mass Transf.*, 135 (2022) 106062.
- [18] E. Alali and A.M. Megahed, MHD dissipative Casson nanofluid liquid film flow due to an unsteady stretching sheet with radiation influence and slip velocity phenomenon, *Nanotechnol. Rev.*, 11 (1) (2022) 463-472.
- [19] B.C. Sakiadis, Boundary-layer behavior on continuous solid surfaces: I. Boundary-layer equations for two-dimensional and axisymmetric flow, *AIChE J.*, 7 (1) (1961) 26-28.
- [20] L.J. Crane, Flow past a stretching plate, *J. Appl. Math. Phys., ZAMP*, 21 (4) (1970) 645-647.
- [21] P.M. Patil, S. Roy and I. Pop, Chemical reaction effects on unsteady mixed convection boundary layer flow past a permeable slender vertical cylinder due to a nonlinearly stretching velocity, *Chem. Eng. Commun.*, 200 (3) (2013) 398-417.
- [22] A.S. Butt, A. Ali and A. Mehmood, Numerical investigation of magnetic field effects on entropy generation in viscous flow over a stretching cylinder embedded in a porous medium, *Energy*, 99 (2016) 237-249.

- [23] V. Rajesh, O.A. Beg and C. Sridevi, Finite difference analysis of unsteady MHD free convective flow over moving semi-infinite vertical cylinder with chemical reaction and temperature oscillation effects, *J. Appl. Fluid Mech.*, 9 (1) (2016) 157-167.
- [24] T. Hayat, S. Qayyum, M. Farooq, A. Alsaedi and M. Ayub, Mixed convection flow of Jeffrey fluid along an inclined stretching cylinder with double stratification effect, *Therm. Sci.*, 21(2) (2017) 849-862.
- [25] M. Azam, T. Xu and M. Khan, Numerical simulation for variable thermal properties and heat source/sink in flow of Cross nanofluid over a moving cylinder, *Int. Commun. Heat Mass Transf.*, 118 (2020) 104832.
- [26] S.U.S. Choi, Enhancing thermal conductivity of fluids with nanoparticles, *ASME Publications-Fed*, 231 (1995) 99-106.
- [27] J. Buongiorno, Convective transport in nanofluids, *J. Heat Transf.*, 128 (3) (2006) 240-250.
- [28] A.I. Alsabery, M.A. Ismael, A.J. Chamkha and I. Hashim, Effect of nonhomogeneous nanofluid model on transient natural convection in a non-Darcy porous cavity containing an inner solid body, *Int. Commun. Heat Mass Transf.*, 110 (2020) 104442.
- [29] Y.B. Kho, A. Hussanan, M.K.A. Mohamed and M.Z. Salleh, Heat and mass transfer analysis on flow of Williamson nanofluid with thermal and velocity slips: Buongiorno model, *Propuls. Power Res.*, 8(3) (2019) 243-252.
- [30] F. Alzahrani and M.I. Khan, Applications of Darcy-Forchheimer 3D reactive rotating flow of rate type nanoparticles with non-uniform heat source and sink and activation energy, *Chem. Phys. Lett.*, 783 (16) (2021) 139054.

- [31] Y.M. Chu, M. Ramzan, N. Shaheen, J.D. Chung, S. Kadry, F. Howari, M.Y. Malik and H.A.S. Ghazwani, Analysis of Newtonian heating and higher-order chemical reaction on a Maxwell nanofluid in a rotating frame with gyrotactic microorganisms and variable heat source/sink, *J. King Saud Univ. Sci.*, **33** (8) (2021) 101645.
- [32] G. Rasool and A. Wakif, Numerical spectral examination of EMHD mixed convective flow of second-grade nanofluid towards a vertical Riga plate using an advanced version of the revised Buongiorno's nanofluid model, *J. Therm. Anal. Calorim.*, **143** (3) (2021) 2379-2393.
- [33] B. Bakthavatchalam, K. Habib, R. Saidur, B.B. Saha and K. Irshad, Comprehensive study on nanofluid and ionanofluid for heat transfer enhancement: A review on current and future perspective, *J. Mol. Liq.*, **305** (2020) 112787.
- [34] T. Ma, Z. Guo, M. Lin and Q. Wang, Recent trends on nanofluid heat transfer machine learning research applied to renewable energy, *Renew. Sust. Energ. Rev.*, **138** (2021) 110494.
- [35] E.C. Okonkwo, I. Wole-Osho, I.W. Almanassra, Y.M. Abdullatif and T. Al-Ansari, An updated review of nanofluids in various heat transfer devices, *J. Therm. Anal. Calorim.*, **145** (6) (2021) 2817-2872.
- [36] D.C. Llorens, P. Vicente and A. Viedma, Experimental study of heat transfer to non-Newtonian fluids inside a scraped surface heat exchanger using a generalization method, *Int. J. Heat Mass Transf.*, **118** (2018) 75-87.
- [37] U.S. Mahabaleshwar, K.R. Nagaraju, P.V. Kumar, M.N. Nadagouda, R. Bennacer and M.A. Sheremet, Effects of Dufour and Soret mechanisms on MHD mixed convective-

radiative non-Newtonian liquid flow and heat transfer over a porous sheet, *Therm. Sci. Eng. Prog.*, 16 (2020) 100459.

- [38] K.U. Rehman, W. Shatanawi and M.Y. Malik, Heat transfer and double sampling of stratification phenomena in non-Newtonian liquid suspension: A comparative thermal analysis, *Case Stud. Therm. Eng.*, 33 (2022) 101934.
- [39] S. Akhtar, S. Almutairi and S. Nadeem, Impact of heat and mass transfer on the Peristaltic flow of non-Newtonian Casson fluid inside an elliptic conduit: Exact solutions through novel technique, *Chin. J. Phys.*, 78 (2022) 194-206.
- [40] D. Banerjee, S. Pati and P. Biswas, Analysis of electroviscous effect and heat transfer for flow of non-Newtonian fluids in a microchannel with surface charge-dependent slip at high zeta potentials, *Phys. Fluids*, 34 (11) (2022) 112016.
- [41] P. Jalili, A.A. Azar, B. Jalili and D.D. Ganji, Study of nonlinear radiative heat transfer with magnetic field for non-Newtonian Casson fluid flow in a porous medium, *Results Phys.*, 48 (2023) 106371.
- [42] X. Wang, Y. Qiao, H. Qi and H. Xu, Numerical study of pulsatile non-Newtonian blood flow and heat transfer in small vessels under a magnetic field, *Int. Commun. Heat Mass Transf.*, 133 (2022) 105930.
- [43] N.S. Khashi'ie, I. Waini, A.R.M. Kasim, N.A. Zainal, A. Ishak and I. Pop, Magnetohydrodynamic and viscous dissipation effects on radiative heat transfer of non-Newtonian fluid flow past a nonlinearly shrinking sheet: Reiner–Philippoff model, *Alex. Eng. J.*, 61 (10) (2022) 7605-7617.

- [44] J. Wang, G. Tan, J. Wang and L.F. Feng, Numerical study on flow, heat transfer and mixing of highly viscous non-newtonian fluid in Sulzer mixer reactor, *Int. J. Heat Mass Transf.*, 183 (2022) 122203.
- [45] A.R. Bestman, Natural convection boundary layer with suction and mass transfer in a porous medium, *Int. J. Energy Res.*, 14 (4) (1990) 389-396.
- [46] A.R. Bestman, Radiative heat transfer to flow of a combustible mixture in a vertical pipe, *Int. J. Energy Res.*, 15 (3) (1991) 179-184.
- [47] M.I. Khan, T. Nasir, T. Hayat, N.B. Khan and A. Alsaedi, Binary chemical reaction with activation energy in rotating flow subject to nonlinear heat flux and heat source/sink, *J. Comput. Des. Eng.*, 7 (3) (2020) 279-286.
- [48] R. Kumar, A. Bhattacharyya, G.S. Seth and A.J. Chamkha, Transportation of magnetite nanofluid flow and heat transfer over a rotating porous disk with Arrhenius activation energy: Fourth order Noumerov's method, *Chin. J. Phys.*, 69 (2021) 172-185.
- [49] B. Mahanthesh, K. Thriveni, P. Rana and T. Muhammad, Radiative heat transfer of nanomaterial on a convectively heated circular tube with activation energy and nanoparticle aggregation kinematic effects, *Int. Commun. Heat Mass Transf.*, 127 (2021) 105568.
- [50] G. Revathi, V.S. Sajja, C.S.K. Raju and M.J. Babu, Numerical simulation for Arrhenius activation energy on the nanofluid dissipative flow by a curved stretching sheet, *Eur. Phys. J.: Spec. Top.*, 230 (5) (2021) 1283-1292.

- [51] M.B. Rekha, I.E. Sarris, J.K. Madhukesh, K.R. Raghunatha and B.C. Prasannakumara, Activation energy impact on flow of AA7072-AA7075/Water-Based hybrid nanofluid through a cone, wedge and plate, *Micromachines*, 13 (2) (2022) 302.
- [52] F. Alzahrani and M.I. Khan, Significance of induced magnetic force bio-convective flow of radiative Maxwell nanofluid with activation energy, *Case Stud. Therm. Eng.*, 27 (2021) 101282.
- [53] A. Shahid, M.M. Bhatti, R. Ellahi and K.S. Mekheimer, Numerical experiment to examine activation energy and bi-convection Carreau nanofluid flow on an upper paraboloid porous surface: Application in solar energy, *Sustain. Energy Technol. Assess.*, 52 (2022) 102029.
- [54] M.A. Chaudhary and J.H. Merkin, A simple isothermal model for homogeneous-heterogeneous reactions in boundary-layer flow. I Equal diffusivities, *Fluid Dyn. Res.*, 16 (6) (1995) 311.
- [55] J.H. Merkin, A model for isothermal homogeneous-heterogeneous reactions in boundary-layer flow, *Math. Comput. Model. Dyn. Syst.*, 24 (8) (1996) 125-136.
- [56] I.L. Animasaun, C.S.K. Raju and N. Sandeep, Unequal diffusivities case of homogeneous-heterogeneous reactions within viscoelastic fluid flow in the presence of induced magnetic-field and nonlinear thermal radiation, *Alex. Eng. J.*, 55 (2) (2016) 1595-1606.
- [57] O.K. Koriko, I.L. Animasaun, M.G. Reddy and N. Sandeep, Scrutinization of thermal stratification, nonlinear thermal radiation and quartic autocatalytic chemical reaction effects on the flow of three-dimensional Eyring-Powell alumina-water nanofluid, *Multidiscip. Model. Mater. Struct.*, 14 (2) (2018) 261-283.

- [58] R. Kumar, R. Kumar, R. Koundal, S.A. Shehzad and M. Sheikholeslami, Cubic autocatalysis reactions in three-dimensional nanofluid flow considering viscous and Joule dissipations under thermal jump, *Commun. Theor. Phys.*, 71 (7) (2019) 779.
- [59] F.E. Alsaadi, T. Hayat, S.A. Khan, F.E. Alsaadi and M.I. Khan, Investigation of physical aspects of cubic autocatalytic chemically reactive flow of second grade nanomaterial with entropy optimization, *Comput. Methods Programs Biomed.*, 183 (2020) 105061.
- [60] G. Sarojamma, R.V. Lakshmi, P.V.S. Narayana and I.L. Animasaun, Exploration of the significance of autocatalytic chemical reaction and Cattaneo-Christov heat flux on the dynamics of a micropolar fluid, *J. Appl. Comput.*, 6 (1) (2020) 77-89.
- [61] R. Meenakumari, P. Lakshminarayana and K. Vajravelu, Influence of induced magnetic field and slip conditions on convective Prandtl fluid flow over a stretching surface with homogeneous and heterogeneous reactions, *Multidiscip. Model. Mater. Struct.*, 17 (1) (2020) 127-147.
- [62] J.B.J. Fourier, *Theorie analytique de la chaleur*, Didot, Paris, (1822) 499-508.
- [63] C. Cattaneo, Sulla conduzione del calore. *Atti Sem. Mat. Fis. Univ. Modena*, 3 (1948) 83-101.
- [64] C.I. Christov, On frame indifferent formulation of the Maxwell–Cattaneo model of finite-speed heat conduction, *Mech.*, 36 (4) (2009) 481-486.
- [65] S.Z. Alamri, A.A. Khan, M. Azeez and R. Ellahi, Effects of mass transfer on MHD second grade fluid towards stretching cylinder: a novel perspective of Cattaneo–Christov heat flux model, *Phys. Lett., A*, 383 (2-3) (2019) 276-281.

- [66] G. Rasool and T. Zhang, Darcy-Forchheimer nanofluidic flow manifested with Cattaneo-Christov theory of heat and mass flux over non-linearly stretching surface, PLoS One, 14 (8) (2019) e0221302.
- [67] M. Turkyilmazoglu, Heat transfer enhancement feature of the non-Fourier Cattaneo-Christov heat flux model, J. Heat Transf., 143 (9) (2021) 094501.
- [68] B. Ali, P.K. Pattnaik, R.A. Naqvi, H. Waqas and S. Hussain, Brownian motion and thermophoresis effects on bioconvection of rotating Maxwell nanofluid over a Riga plate with Arrhenius activation energy and Cattaneo-Christov heat flux theory, Therm. Sci. Eng. Prog., 23 (2021) 100863.
- [69] M.V. Reddy and P. Lakshminarayana, MHD radiative flow of Williamson nanofluid with Cattaneo-Christov model over a stretching sheet through a porous medium in the presence of chemical reaction and suction/injection, J. Porous Media, 25 (12) (2022) 1-15.
- [70] S.J. Liao, The proposed homotopy analysis technique for the solution of nonlinear problems, Ph.D. Thesis, Shanghai Jiao Tong University, 1992.
- [71] M. Khan, A. Ahmed, M. Irfan and J. Ahmed, Analysis of Cattaneo-Christov theory for unsteady flow of Maxwell fluid over stretching cylinder, J. Therm. Anal. Calorim., 144 (2021) 145-154.
- [72] M.S. Abel, J.V. Tawade and M.M. Nandeppanavar, MHD flow and heat transfer for the upper-convected Maxwell fluid over a stretching sheet, Meccanica, 47 (2) (2012) 385-393.

- [73] A.M. Megahed, Variable fluid properties and variable heat flux effects on the flow and heat transfer in a non-Newtonian Maxwell fluid over an unsteady stretching sheet with slip velocity, *Chin. Phys. B*, 22 (9) (2013) 094701.
- [74] A.K. Pandey and M. Kumar, Natural convection and thermal radiation influence on nanofluid flow over a stretching cylinder in a porous medium with viscous dissipation, *Alex. Eng. J.*, 56 (1) (2017) 55-62.
- [75] K.R. Rajagopal and R.K. Bhatnagar, Exact solutions for some simple flows of an Oldroyd-B fluid, *Acta Mech.*, 113 (1) (1995) 233-239.
- [76] M. Jamil, C. Fetecau and M. Imran, Unsteady helical flows of Oldroyd-B fluids, *Commun. Nonlinear Sci.*, 16 (3) 9 (2011) 1378-1386.
- [77] W.A. Khan and I. Pop, Boundary-layer flow of a nanofluid past a stretching sheet, *Int. J. Heat Mass Transf.*, 53 (11-12) (2010) 2477-2483.
- [78] A. Ahmed, M. Khan, A. Hafeez and J. Ahmed, Thermal analysis in unsteady radiative Maxwell nanofluid flow subject to heat source/sink, *App. Nanosci.*, 10 (2020) 1-9.
- [79] M.R. Shirkhani, H.A. Hoshyar, I. Rahimipetroudi, H. Akhavan and D.D. Ganji, Unsteady time-dependent incompressible Newtonian fluid flow between two parallel plates by homotopy analysis method (HAM), homotopy perturbation method (HPM) and collocation method (CM), *Propuls. Power Res.*, 7 (3) (2018) 247-256.
- [80] L.R.K.R.W.D.R. Talbot, R.K. Cheng, R.W. Schefer and D.R. Willis, Thermophoresis of particles in a heated boundary layer, *J. Fluid Mech.*, 101 (4) (1980) 737-758.

- [81] G.K. Batchelor and C. Shen, Thermophoretic deposition of particles in gas flowing over cold surfaces, *J. Colloid Interface Sci.*, 107 (1) (1985) 21-37.
- [82] R.N. Kumar, R.J. Punith Gowda, G.D. Prasanna, B.C. Prasannakumara, K.S. Nisar and W. Jamshed, Comprehensive study of thermophoretic diffusion deposition velocity effect on heat and mass transfer of ferromagnetic fluid flow along a stretching cylinder, *Proc. Inst. Mech. Eng. E: J. Process Mech. Eng.*, 235 (5) (2021) 1479-1489.
- [83] A. Ahmed, M. Khan, J. Ahmed and S. Nadeem, Mixed convection in unsteady stagnation point flow of Maxwell fluid subject to modified Fourier's law, *Arab. J. Sci. Eng.*, 45 (11) (2020) 9439-9447.
- [84] F.M. Abbasi, M. Mustafa, S.A. Shehzad, M.S. Alhuthali and T. Hayat, Analytical study of Cattaneo–Christov heat flux model for a boundary layer flow of Oldroyd-B fluid, *Chin. Phys. B*, 25 (1) (2015) 014701.
- [85] T. Hayat, Z. Hussain, A. Alsaedi and M. Farooq, Magnetohydrodynamic flow by a stretching cylinder with Newtonian heating and homogeneous-heterogeneous reactions, *PLoS One*, 11 (6) (2016) e0156955.
- [86] S. Sharidan, M. Mahmood and I. Pop, Similarity solutions for the unsteady boundary layer flow and heat transfer due to a stretching sheet, *App. Mecm. Eng.*, 11 (3) (2006) 647-654.
- [87] A.J. Chamkha, A.M. Aly and M.A. Mansour, Similarity solution for unsteady heat and mass transfer from a stretching surface embedded in a porous medium with suction/injection and chemical reaction effects, *Chem. Eng. Commun.*, 197 (6) (2010) 846-858.

- [88] W.A. Khan, M. Irfan and M. Khan, An improved heat conduction and mass diffusion models for rotating flow of an Oldroyd-B fluid, *Results Phys.*, 7 (2017) 3583-3589.

Turnitin Originality Report

Flow and Thermal Analysis of Oldroyd-B Fluid due to Stretching Surfaces
Muhammad Yasir .

by



From PhD (PhD DRSML)

- Processed on 23-Feb-2024 15:23 PKT
- ID: 2302356646
- Word Count: 23128

Similarity Index
16%

Similarity by Source

Internet Sources:

11%

Publications:

10%

Student Papers:

2%

Masoodulhaq
Professor
Department of Mathematics
Quaid-i-Azam University

M. Yasir
Focal Person (Turnitin)
Quaid-i-Azam University
Islamabad

sources:

1

1% match (Internet from 04-Feb-2023)

https://www.researchgate.net/publication/328547548_Effects_of_mass_transfer_on_MHD_second_grade_fluid_towards_stretching_cylinder_A_novel_perspective_of_Cattaneo-Christov_heat_flux_model

2

1% match (Internet from 07-Feb-2023)

https://www.researchgate.net/publication/245095123_Thermal_convection_with_the_Cattaneo-Christov_model

3

1% match (Internet from 07-Feb-2023)

https://www.researchgate.net/publication/324949615_Investigation_on_ethylene_glycol_Nano_fluid_flow_over_a_vertical_permeable_circular_cylinder_under_effect_of_magnetic_field

4

1% match (Internet from 19-Mar-2023)

https://www.researchgate.net/publication/331928668_Natural_Convection_Effects_on_Heat_and_Mass_Transfer_of_Slip_Flow_of_time-dependent_Prandtl_Fluid

5

1% match (Internet from 31-Oct-2022)

<http://pr.hec.gov.pk/jspui/bitstream/123456789/20440/1/Abdul%20hafeez%20mathematics%202022%20qau%20isb.pdf%2027.5.22.pdf>

6

1% match (Internet from 19-Mar-2023)

<https://www.scribd.com/document/631587497/Mathematical-modelling-of-unsteady-Oldroyd-B-fluid-flow-d-2023-Ain-Shams-Eng>

7

1% match (Internet from 10-Dec-2022)

<https://www.scilit.net/journal/818698>

8

< 1% match (Internet from 17-Feb-2023)